NATIONAL TECHNICAL UNIVERSITY OF ATHENS
SCHOOL OF RURAL & SURVEYING ENGINEERING
DEPARTMENT OF TOPOGRAPHY
LABORATORY OF GENERAL GEODESY

CONSEIL EUROPÉEN POUR LA RECHERCHE NUCLÉAIRE
EUROPEAN COUNCIL FOR NUCLEAR RESEARCH

DEVELOPMENT OF AN ALGORITHM FOR THE POSITION DETERMINATION OF ENCODED AND UNCODED TARGETS

Application on the fiducials position and their offset distance determination with respect to a stretched wire on the cryogenic magnets of the LHC at CERN

Servet Lapardhaja

Diploma Thesis

Supervisor:
Evangelia Lambrou
Professor NTUA

Athens June 2019

This work is devoted to my family and my professors,
who encouraged me to go to CERN in order to elaborate my thesis.

ACKNOWLEDGEMENTS

Servet Lapardhaja

FOREWORD

My six months partnership with the European Organization for Nuclear Research as a Trainee, allowed me to discover the exceptional work environment and research community of CERN. People from various countries with different professions and disciplines cooperate in order to complete and achieve specific tasks and goals.

The Surveying team at CERN uses techniques from various fields such as geodesy and photogrammetry, in order to achieve high quality results in several tasks. The precision and the reliability are two of the main objectives of surveyors and are the key elements for a high quality work.

A short term internship of six months, may not be a sufficient amount of time in order to comprehend fully the whole term projects that are taking place in the facilities of CERN, however it offers a unique experience to collaborate with experienced researchers.

Finally, I would like to mention that this diploma thesis is based on a specific task that took place at CERN, is a sequel of previous projects and thesis from other students that had also the opportunity as me to work at the CERN facilities. The objective of all the information that is gathered and presented is to be used in the future as tools for various CERN applications.

CONTENTS

FIGURES

x

PHOTOS

TABLES

ABSTRACT

The objective of this thesis is the development of an algorithm for the automatic detection and position determination of encoded and uncoded targets. The developed algorithm includes several parts which are:

- the automatic detection of all the targets
- their precise 2D image coordinates determination
- the decoding of the encoded targets and the detection of the corresponding uncoded targets

An application of the algorithm has been done on the cryomagnets of the LHC at CERN. The aim of the application was the position determination of the fiducials on which uncoded targets are mounted and the calculation of their offset distance with respect to an installed stretched wire.

Fiducials are fixed points which are used as reference marks and their position is linked with the inner geometry of the magnet.

This thesis is summarized on the following chapters:

- **The first chapter** is an introduction about CERN and provides the reader with the basic information for the organization, the Large Hadron Accelerator and the objectives of this work.

  In particular, reference is made to the establishment of the organization, and of which member states it is composed, including Greece, which is a founding member.

  Then there is a presentation about the EN-SMM-ESA section and its functions, the LHC accelerator and the alignment tasks.

  At the end of the chapter a brief reference is made to the process of automatic target detection, measurement and decoding.

- **The second chapter** presents the application of close range photogrammetry, the equipment and the targets that were used in the accelerators and the process of distortion correction.

  Furthermore, the principle of offset measurement with respect to a stretched wire is referenced and the usefulness of this method at the CERN's accelerators is mentioned and the high precision to the level of few micrometers that it provides.

At the end of the chapter, the advantages of the usage of photogrammetry for the measurement and determination of wires are highlighted.

- **The third chapter** describes the development of the algorithm for the automatic detection of targets, what this algorithm includes and what are the conditions in order to achieve the detection.

  Initially, the types of targets that are commonly used are presented which are distinguished to the ones that are encoded and uncoded.

  Afterwards, there is a brief description of the MATLAB software, which was chosen for the development of the algorithm. The basic parameters, are introduced and the different kind of preprocessing procedures that are implemented, are presented.

  For the detection of the targets, reference is made to three algorithms, concluding that the most reliable is the one based on the *regionprops* function.

  At the end of the chapter, there is a comparison of the results that are produced by using the detection algorithm and the AICON software. The number of detected targets by the developed algorithm but also by the AICON software are at the same level and almost equal.

- **The fourth chapter** presents various algorithms that were tested for the target position determination, their advantages and disadvantages and the precision that has been achieved.

  At first, implementing an algorithm in order to position the targets, the image should be cropped into multiple pieces, where each piece contains one target individually. Then the target position determination algorithms can be executed.

  Among the algorithms that are being presented in this chapter the most reliable is the one that makes the ellipse adjustment because it is able to provide the standard deviations for the image coordinates. Thus, it is feasible to evaluate the quality of the position determination. The results of this algorithm will be used as observations for the bundle adjustment.

  At the end of this chapter, various analyses are presented concerning:

  - the precision of the determination of each target

- the residuals after the bundle adjustment
- the RMS on X, Y and Z resulting from the various algorithms
- the residuals that come out after the transformation of the targets' coordinates when the three-dimensional coordinates that are used as reference points are provided via AICON

After all the analyses, the most reliable results arise, if the image coordinates which were calculated by the ellipse fitting are used as observations.

- **The fifth chapter** describes how the decoding algorithm works for encoded targets that have a particular pattern and the problems that occurred during the decoding process. These targets have a circular black or white body at their center which is surrounded by circular code segments of specific patterns.

  Thanks to the pattern, a binary number sequence can be created which represents the color changes from black to white and the inverse, on the code segments. Each sequence corresponds to a number when the binary number is converted to an integer in the decimal system.

  Every target, depending on the number of bits available, can produce an equal number of binary sequences. For instance, a 14-bit target can create 14 different binary sequences by simply moving the first digit of the binary number at the end and thus 14 different codes are created.

  From all the code numbers, the smallest one is selected and then a search for correspondence on a lookup table is executed to find the match of the number found, with the code that AICON provides.

  However, there are some issues which may make the decoding nearly impossible, such as:

  - the very small size of targets
  - the lightning conditions
  - the quality of the targets

  At the end of this chapter, how to find the correspondence on each image among uncoded targets is analyzed. This can be achieved by using the collinearity equations combined with least squares.

- **The sixth chapter** presents the basic functionalities of the LGC2 adjustment software that is developed at CERN and the basic types

of observations that are used such as UVD, UVEC, ANGL and ZEND.

Afterwards, it is described how the data that concern the targets and the wire are handled, depending on the observation type that has been selected to be used.

Also, it is mentioned that the extraction of the approximate coordinates of the targets is carried out by using the bundle adjustment report of AICON.

However, the approximate coordinates for the wire can be obtained by the intersection of 2 planes which contain the wire. These planes will produce a line which represents the wire. Then the intersection of this line with the rays from the projection center that head to the wire provide the approximate spatial coordinates of the points on the wire.

When all the available data are gathered and transformed to the format that LGC2 requires then the adjustment can be executed.

- **The seventh chapter** is concerned with the calculation of the 3D, radial and vertical, offset of the fiducials with respect to the stretched wire.

  For the calculation of these distances, 10 photogrammetric projects were carried out at a section of the LHC where the targets and the stretched wire were installed.

  After the determination of the 3D coordinates of the fiducials and the determination of the wire, these targets should be projected on the wire. Once this is completed, the projected points should be inserted into the LGC2, so that the final adjustment can be carried out and the final coordinates of the projections and the fiducials can be calculated. Thus, the offsets can be calculated.

  The offset calculations have been initially carried out by using all the photos of each project and later by using 3, 4, 5 and 6 photos-cameras on specific positions, having the idea of the creation of a frame in the future that will have a specific number of cameras installed on it.

  From the analysis of the results, as it has been expected, the highest precision was achieved when all the 30-35 photos per project were used. This is not feasible to be implemented on a frame, because such a big number of cameras cannot be installed on it. The

number of cameras which is able to provide satisfactory results, is equal to 4. By using 4 cameras the precision of the 3D distance offset for the fiducials is about ± 15 μm to ± 20 μm.

- **The eighth chapter** presents the conclusions of the work and proposals for its detailed implementation.

  The detection algorithm has the ability to detect nearly all the targets whose diameter is greater than 4-5 pixels. For targets with a diameter of more than 4-5 pixels, satisfied precision and reliability of the algorithm is achieved. The comparisons for the number of targets identified by the AICON algorithm and the developed algorithm show that the results were equivalent.

  Among the algorithms of the target position determination, the most precise and reliable one is the one that uses the ellipse adjustment of measured edge points with least squares.

  The precision of both the image coordinates in the image space and the 3D coordinates in the object space is almost the same to AICON. Specifically, the precision of the position determination on the image is in the range of ± 0.03 pixel to ± 0.05 pixel, while in the three dimensional space is from ± 3 μm to ± 8 μm for a distance of approximately 1.0 m from the object. These values demonstrate the high precision of the position determination of the targets.

  In addition, the decoding of the targets, as well as finding the homologous points using the collinearity equations by least squares provide adequate precision to the correlations of the targets among multiple images. In series of experiments with up to 16000 encoded targets, over 98% of them detected by AICON, receive the same code by the developed algorithm. That indicates the high reliability of the decoding algorithm.

  Finally, the calculation of the offset distances of the fiducials with respect to the stretched wire was made with a precision of ± 15 μm to ± 20 μm. This precision is equivalent to the achieved by the manual ecartometry method which is developed at CERN to measure radial offset distances from the fiducials to the stretched wire.

  Due to the lack of suitable equipment and conditions during the experiments, the connection to gravity with adequate precision was not possible. Thus, it is difficult to determine the distance

components (radial and vertical). In order to achieve this, two high precision bi-directional inclinometers should be installed.

By the procedures explained in this work and the developed algorithms, the position determination of targets as well as the measurements of the offset distances can be achieved precisely.

Thus, in addition to the satisfactory precision, measurement automation is achieved, eliminating the errors due to the human factor.

Finally, for the precise measurement of the radial and vertical offsets of the fiducials to the stretched wire, two high precision bi-directional inclinometers should be installed in the frame where the cameras will be mounted in order to achieve the connection to the gravity.

The number of cameras proposed to be installed on the frame is four. With this number of cameras, the required precision and reliability for the targets and wire determination and the measurement of the offset distance is attained.

EXTENDED ABSTRACT IN GREEK

ΑΝΑΠΤΥΞΗ ΑΛΓΟΡΙΘΜΟΥ
ΓΙΑ ΤΟΝ ΠΡΟΣΔΙΟΡΙΣΜΟ ΤΗΣ ΘΕΣΗΣ
ΚΩΔΙΚΟΠΟΙΗΜΕΝΩΝ ΚΑΙ
ΜΗ ΚΩΔΙΚΟΠΟΙΗΜΕΝΩΝ ΣΤΟΧΩΝ

Εφαρμογή για τον προσδιορισμό της θέσης και της απόστασης των fiducials από το τεντωμένο σύρμα στους κρυομαγνήτες του μεγάλου επιταχυντή Αδρονίων στο CERN

Αντικείμενο αυτής της διπλωματικής εργασίας είναι η ανάπτυξη ενός αλγορίθμου για τον αυτόματο εντοπισμό και προσδιορισμό της θέσης κωδικοποιημένων και μη στόχων. Ο αναπτυσσόμενος αλγόριθμος αποτελείται από επιμέρους τμήματα τα οποία περιλαμβάνουν:

- τον αυτόματο εντοπισμό όλων των στόχων
- τον ακριβή προσδιορισμό των εικονοσυντεταγμένων των κέντρων τους
- την αποκωδικοποίηση των κωδικοποιημένων στόχων και εύρεση των ομόλογων μη κωδικοποιημένων στόχων

Εφαρμογή του αλγορίθμου πραγματοποιήθηκε στους κρυομαγνήτες του Μεγάλου Επιταχυντή Αδρονίων στο CERN.

Ο στόχος της εφαρμογής ήταν ο προσδιορισμός της θέσης των fiducials τα οποία είναι μη κωδικοποιημένοι σταθεροί στόχοι και ο υπολογισμός της απόστασής τους από ένα τεντωμένο σύρμα που έχει εγκατασταθεί πάνω στον κρυομαγνήτη.

Τα fiducials αποτελούν τα εξωτερικά ορατά σημεία που η αλληλουχία τους αντιστοιχεί στον άξονα του επιταχυντή και με βάση τη θέση τους πραγματοποιείται η ευθυγράμμιση των τμημάτων του επιταχυντή.

Η διπλωματική εργασία αποτελείται από τα παρακάτω κεφάλαια :

- **Το πρώτο κεφάλαιο** αποτελεί μια αναφορά στο CERN και μας εφοδιάζει με τις βασικές πληροφορίες σχετικά με τον οργανισμό, τον Μεγάλο Επιταχυντή Αδρονίων και τους στόχους της εργασίας.

  Συγκεκριμένα γίνεται αναφορά στην ίδρυση του οργανισμού και στα κράτη μέλη από τα οποία αποτελείται, στα οποία συμπεριλαμβάνεται ως ιδρυτικό μέλος η Ελλάδα.

Επίσης γίνεται αναφορά στον τομέα EN-SMM-ESA και τις λειτουργίες του και επισημαίνονται κάποια βασικά στοιχεία που αφορούν τον επιταχυντή LHC και τις εργασίες ευθυγράμμισης.

Στο τέλος του κεφαλαίου πραγματοποιείται μια αναλυτική καταγραφή του αντικείμενου και των στόχων της διπλωματικής εργασίας.

- **Το δεύτερο κεφάλαιο** παρουσιάζει τον εξοπλισμό και τους στόχους που χρησιμοποιήθηκαν κατά την διεξαγωγή των πειραμάτων καθώς και τη διαδικασία διόρθωσης της διαστροφής στις εικόνες.

  Επιπλέον, επεξηγείται η αρχή της μέτρησης μέσω του τεντωμένου καλωδίου, αναφέρεται η χρησιμότητα της μεθόδου στα πειράματα στο CERN και η υψηλή ακρίβεια της τάξης των λίγων μικρομέτρων που παρέχει καθώς και τα διάφορα προβλήματα που παρουσιάζονται.

  Στο τέλος του κεφαλαίου επισημαίνονται τα πλεονεκτήματα της χρήσης φωτογραμμετρικών μεθόδων για τη μέτρηση της απόστασης των fiducials από το τεντωμένο σύρμα.

- **Το τρίτο κεφάλαιο** περιγράφει την ανάπτυξη του αλγορίθμου για τον αυτόματο εντοπισμό των στόχων, τις βασικές αρχές και τις συνθήκες που απαιτούνται για να πραγματοποιηθεί ο εντοπισμός.

  Αρχικά παρουσιάζονται οι τύποι των στόχων που χρησιμοποιούνται οι οποίοι διακρίνονται σε αυτούς που διαθέτουν κωδικοποίηση (Encoded target) και σε αυτούς που δεν έχουν κάποιο κωδικό (Uncoded targets).

  Παρέχονται συνοπτικά κάποια στοιχεία για το πρόγραμμα MATLAB το οποίο επιλέχθηκε για την ανάπτυξη του αλγορίθμου. Αναφέρονται οι βασικές παράμετροι που θα πρέπει να εισαχθούν από τον χρήστη για την έναρξη της λειτουργίας του αλγορίθμου. Αυτές οι παράμετροι είναι:

  - ο αριθμός των bit των στόχων
  - το χρώμα των στόχων
  - εάν είναι ανακλαστικοί ή όχι
  - η ελάχιστη και μέγιστη διάμετρός τους σε pixel
  - ο μέγιστος λόγος του μεγάλου προς τον μικρό ημιάξονα της έλλειψης
  - ο τρόπος επεξεργασίας της εικόνας

Έπειτα γίνεται αναφορά στα βήματα που ακολουθήθηκαν για την επεξεργασία των εικόνων που είναι απαραίτητη πριν την εφαρμογή του αλγορίθμου για τον εντοπισμό των στόχων.

Για την ανίχνευση των στόχων γίνεται αναφορά σε τρεις αλγορίθμους, καταλήγοντας πως ο πιο αξιόπιστος είναι αυτός που βασίζεται τη χρήση της εντολής *regionprops*.

Στο τέλος του κεφαλαίου γίνεται η σύγκριση των αποτελεσμάτων που προέκυψαν από τον αναπτυχθέντα αλγόριθμο εντοπισμού των στόχων με τα αντίστοιχα αποτελέσματα από τον εμπορικό αλγόριθμο AICON που διαθέτει το CERN σήμερα για την εκτέλεση της διαδικασίας ανίχνευσης και υπολογισμού των συντεταγμένων των στόχων.

Ο αριθμός των στόχων που ανιχνεύονται από τον ανεπτυγμένο αλγόριθμο και από τον αλγόριθμο AICON είναι σχεδόν ίδιος και μάλιστα σε ορισμένα πειράματα είναι και μεγαλύτερος.

- **Το τέταρτο κεφάλαιο** παρουσιάζει διάφορους αλγόριθμους που χρησιμοποιήθηκαν ώστε να γίνει ο προσδιορισμός των συντεταγμένων των στόχων, τα πλεονεκτήματα και τα μειονεκτήματα του καθενός και την ακρίβεια που έχει επιτευχθεί.

  Απαραίτητη πριν γίνει η εφαρμογή ενός αλγορίθμου είναι η περικοπή της εικόνας σε πολλά τμήματα, όπου το κάθε τμήμα θα απεικονίζει τον κάθε στόχο ξεχωριστά.

  Από τους αλγόριθμους που παρουσιάζονται ο πιο αξιόπιστος είναι αυτός της προσαρμογής έλλειψης καθώς παρέχει την τυπική απόκλιση των συντεταγμένων του κάθε στόχου και άρα την ποιότητα προσδιορισμού τους. Έτσι είναι γνωστή η ποιότητα των παρατηρήσεων που θα εισαχθούν έπειτα για να πραγματοποιηθεί η συνόρθωση.

  Μετά τη συνόρθωση με τη μέθοδο των ελαχίστων τετραγώνων είναι γνωστή η ακρίβεια των εικονοσυντεταγμένων του κέντρου του στόχου, ώστε να μπορεί να γίνει αξιολόγησή τους .

  Στο τέλος του κεφαλαίου αυτού παρουσιάζονται διάφορες αναλύσεις που αφορούν:

  - στην ακρίβεια προσδιορισμού των εικονοσυντεταγμένων από κάθε αλγόριθμο
  - στα υπόλοιπα που προκύπτουν μετά την συνόρθωση

- στην ακρίβεια του προσδιορισμού των X, Y, Z που προκύπτουν, εάν ως παρατηρήσεις χρησιμοποιηθούν οι εικονοσυντεταγμένες που προέκυψαν από τους διάφορους αλγορίθμους
- στα υπόλοιπα που παρουσιάζονται μετά τον μετασχηματισμό των συντεταγμένων των στόχων εάν χρησιμοποιηθούν ως σημεία αναφοράς οι τρισδιάστατες συντεταγμένες των στόχων που προέκυψαν από τις μετρήσεις μέσω του AICON

Σε όλες τις αναλύσεις, τα πιο αξιόπιστα αποτελέσματα προκύπτουν εάν ως παρατηρήσεις χρησιμοποιηθούν οι εικονοσυντεταγμένες που υπολογίστηκαν από την προσαρμογή της έλλειψης.

- **Στο πέμπτο κεφάλαιο** αναλύεται η λειτουργία του αλγορίθμου αποκωδικοποίησης για τους κωδικοποιημένους στόχους που έχουν ένα συγκεκριμένο πρότυπο. Το κυκλικό πρότυπο που διαθέτουν οι στόχοι είναι μια αλληλουχία δυαδικών αριθμών που δημιουργείται καταγράφοντας τις μεταβολές του λευκού με το μαύρο. Η κάθε αλληλουχία αντιστοιχεί σε έναν αριθμό εφόσον γίνει η μετατροπή του δυαδικού αριθμού σε ακέραιο αριθμό στο δεκαδικό σύστημα.

Κάθε στόχος ανάλογα με τον αριθμό των bit που διαθέτει μπορεί να παράγει ισάριθμο αριθμό αλληλουχιών δυαδικών αριθμών. Για παράδειγμα ένας 14bit στόχος μπορεί να δημιουργήσει 14 διαφορετικές αλληλουχίες δυαδικών αριθμών μεταθέτοντας απλώς κάθε φορά το πρώτο ψηφίο του δυαδικού αριθμού προς το τέλος και έτσι δημιουργούνται 14 διαφορετικοί κωδικοί.

Από όλους τους αριθμούς επιλέγεται ο μικρότερος και κατόπιν γίνεται μια αναζήτηση στον αντίστοιχο look up table για να βρεθεί η αντιστοιχία του αριθμού που επιλέχθηκε με τον κωδικό που παρέχεται από τον αλγόριθμο του AICON.

Διάφορες οι αιτίες μπορούν να κάνουν δύσκολη είτε ακόμη και να καταστήσουν την αποκωδικοποίηση μη εφικτή, τέτοιες για παράδειγμα είναι:

- το μέγεθος των στόχων
- ο φωτισμός
- η ποιότητα κατασκευής τους

Στο τέλος αυτού του κεφαλαίου γίνεται επίσης αναφορά και στον τρόπο αναγνώρισης των στόχων που είναι μη κωδικοποιημένοι και εύρεσης ομόλογων σημείων. Βασική συνθήκη για να επιτευχθεί η

αναγνώριση είναι η εφαρμογή της εμπροσθοτομίας χρησιμοποιώντας τη συνθήκη συγγραμμικότητας με τη μέθοδο ελαχίστων τετραγώνων.

- **Το έκτο κεφάλαιο** παρουσιάζει τις βασικές λειτουργίες του προγράμματος συνόρθωσης LGC2 που έχει αναπτυχθεί στο CERN και το οποίο θα χρησιμοποιηθεί για τον υπολογισμό των τελικών συντεταγμένων των fiducials και των προβολών τους πάνω στο σύρμα.

  Γίνεται αναφορά στα βασικά είδη των παρατηρήσεων που χρησιμοποιούνται όπως το UVD που χρησιμοποιεί μοναδιαία διανύσματα και αποστάσεις, το UVEC που αποτελεί απλοποίηση του UVD αφού κάνει χρήση μόνο του μοναδιαίου διανύσματος και των παρατηρήσεων οριζόντιων και κατακόρυφων γωνιών οι οποίες είναι διαθέσιμες μόνο στην έκδοση του LGC2.

  Έπειτα γίνεται διάκριση στον τρόπο χειρισμού και επεξεργασίας των δεδομένων ανάλογα αν το αντικείμενο μελέτης είναι ένας στόχος ή ένα τεντωμένο σύρμα.

  Επίσης αναφέρεται πως οι προσωρινές συντεταγμένες στο χώρο για τους στόχους εξάγονται από το bundle adjustment report. Όσον αφορά το εγκατεστημένο σύρμα ο υπολογισμός των προσωρινών συντεταγμένων των σημείων του πραγματοποιείται με την τομή επιπέδων που ορίζονται από το κέντρο προβολής της φωτογραφίας και δυο σημείων του σύρματος. Αυτή η τομή ορίζει μια ευθεία που αναπαριστά το σύρμα.

  Έπειτα ορίζεται τομή των ακτίνων από το κέντρο προβολής προς το σύρμα ώστε να προσδιοριστούν οι προσωρινές συντεταγμένες στο χώρο των σημείων που είναι προς αναζήτηση.

- **Το έβδομο κεφάλαιο** ασχολείται με τον υπολογισμό της απόστασης στο χώρο, αλλά και των συνιστωσών της ακτινικής και κατακόρυφης απόστασης των σταθερών στόχων από το τεντωμένο σύρμα.

  Για τον προσδιορισμό των αποστάσεων αυτών πραγματοποιήθηκαν 10 πειράματα - εφαρμογές σε ένα τμήμα του κρυομαγνήτη στον LHC όπου έγινε εγκατάσταση των στόχων και του τεντωμένου σύρματος. Σε κάθε πείραμα πραγματοποιήθηκαν 30 με 35 λήψεις φωτογραφιών από διαφορετικές θέσεις με διαφορετικές στροφές στην κάμερα με σκοπό την βέλτιστη κάλυψη και κατανομή των φωτογραφιών στην περιοχή.

Μετά τον προσδιορισμό των τριδιάστατων συντεταγμένων των σταθερών στόχων και του σύρματος, γίνεται η προβολή αυτών των στόχων στο σύρμα. Τα σημεία προβολής εισάγονται στο πρόγραμμα LGC2 για να γίνει η τελική συνόρθωση και να υπολογιστούν οι τελικές συντεταγμένες των σταθερών στόχων και των προβολών τους στο σύρμα ώστε να υπολογιστούν οι αποστάσεις.

Ο υπολογισμός των αποστάσεων και η εκτίμηση των ακριβειών τους γίνεται χρησιμοποιώντας αρχικά όλες τις φωτογραφίες από κάθε πείραμα (30-35) και έπειτα χρησιμοποιώντας 3, 4, 5 και 6 κάμερες-φωτογραφίες σε συγκεκριμένες θέσεις. Η παραπάνω διερεύνηση έγινε προκειμένου να προκύψει ο ελάχιστος αριθμός καμερών που ικανοποιείται την επιθυμητή ακρίβεια.

Από την ανάλυση των αποτελεσμάτων προκύπτει ότι η καλύτερη ακρίβεια επιτυγχάνεται χρησιμοποιώντας όλες τις φωτογραφίες που ελήφθησαν από κάθε μια κάμερα.

Το ελάχιστο πλήθος των καμερών που κρίνεται ότι αποδίδει ικανοποιητικά αποτελέσματα είναι 4 κάμερες όπου οι ακρίβεια προσδιορισμού της απόστασης των σταθερών στόχων είναι της τάξης των ±15 μm έως ±20 μm.

- **Το όγδοο κεφάλαιο** παρουσιάζει τα συμπεράσματα της εργασίας και προτάσεις για την καλύτερη εφαρμογή της.

Ο αλγόριθμος εντοπισμού των στόχων έχει τη δυνατότητα ανίχνευσης και εντοπισμού σχεδόν όλων των στόχων των οποίων η διάμετρος είναι μεγαλύτερη από 4-5 pixel. Για μεγέθη στόχων με διάμετρο άνω των 4-5 pixel η ακρίβεια και η αξιοπιστία του αλγορίθμου είναι ιδιαίτερα ικανοποιητική. Από τις συγκρίσεις που πραγματοποιήθηκαν μεταξύ του αριθμού των στόχων που εντοπίστηκαν από τον αλγόριθμο του AICON και τον αναπτυχθέντα αλγόριθμο τα αποτελέσματα ήταν ταυτόσημα.

Από τους αλγορίθμους προσδιορισμού των εικονοσυντεταγμένων των στόχων, ο πιο ακριβής και αξιόπιστος είναι αυτός που κάνει τη χρήση της προσαρμογής της έλλειψης, με συνόρθωση ελαχίστων τετραγώνων.

Η ακρίβεια τόσο των εικονοσυντεταγμένων όσο και των συντεταγμένων στο χώρο των στόχων είναι σχεδόν ταυτόσημη με αυτή που επιτυγχάνεται με το AICON. Συγκεκριμένα η ακρίβεια προσδιορισμού των εικονοσυντεταγμένων είναι της τάξης $\pm$ 0.03

pixel έως ± 0.05 pixel, ενώ στον τρισδιάστατο χώρο από ± 3 μm έως ± 8 μm για αποστάσεις που κυμαίνονται στο 1.0 m . Η τάξη μεγέθους αυτών των τιμών αποδεικνύει την ικανοποιητική ακρίβεια προσδιορισμού των θέσεων των στόχων.

Επιπλέον η αποκωδικοποίηση των στόχων, καθώς και η εύρεση ομόλογων σημείων χρησιμοποιώντας τις εξισώσεις συγγραμμικότητας με συνόρθωση ελαχίστων τετραγώνων προσδίδουν ικανοποιητική ακρίβεια στη συσχέτιση των στόχων στις φωτογραφίες.

Σε σειρά πειραμάτων με συνολικό αριθμό 16000 κωδικοποιημένων στόχων, πάνω από το 98% των κωδικοποιημένων στόχων που ανιχνεύτηκαν από το AICON έλαβαν τον ίδιο κωδικό και από τον αναπτυχθέντα αλγόριθμο. Το γεγονός αυτό δηλώνει την μεγάλη αξιοπιστία του αλγορίθμου αποκωδικοποίησης των κωδικοποιημένων στόχων.

Τέλος όσον αφορά στον προσδιορισμό των αποστάσεων των fiducials από το τεντωμένο σύρμα, έγινε με ακρίβεια της τάξης των ±15 μm έως ±20μm.

Αυτή η ακρίβεια είναι αντίστοιχη με αυτή που επιτυγχάνεται μέσω της μεθόδου ecartometry που έχει αναπτυχθεί στο CERN για την μέτρηση κάθετων αποστάσεων από τα fiducials προς το τεντωμένο σύρμα.

Λόγω της έλλειψης κατάλληλου εξοπλισμού αλλά και των συνθηκών κατά τη διάρκεια των πειραμάτων, δεν ήταν δυνατός ο ακριβής ορισμός του συστήματος αναφοράς, γεγονός που καθιστά δύσκολο τον προσδιορισμό των συνιστωσών της απόστασης (ακτινικής και κατακόρυφης). Προκειμένου να επιτευχθεί αυτό θα πρέπει να εγκατασταθούν δυο υψηλής ακρίβειας κλισίμετρα ώστε να γίνει ο ακριβής ορισμός της κατακορύφου.

Η διαδικασία που αναπτύχτηκε στην εργασία αυτή με τη λήψη φωτογραφιών και τη χρήση των αλγορίθμων που αναπτύχθηκαν μπορούν να κάνουν προσδιορισμό θέσεων των στόχων με ακρίβεια ±7 μm όσο και των αποστάσεων των fiducials από το τεντωμένο σύρμα με ακρίβεια ±15 μm έως ±20 μm. Ο προσδιορισμός των αποστάσεων επιτυγχάνεται με ακρίβεια αντίστοιχη της προηγούμενης διαδικασίας που εφαρμόζονταν στο CERN για το σκοπό αυτό.

Έτσι εκτός από την επιθυμητή ακρίβεια, επιτυγχάνεται και η αυτοματοποίηση των μετρήσεων, ώστε να εξαλείφεται η

πιθανότητα παρουσίας χονδροειδών σφαλμάτων λόγω του ανθρώπινου παράγοντα.

Τέλος για την ακριβή μέτρηση των ακτινικών και κατακόρυφων αποστάσεων των σταθερών στόχων (fiducials) από το τεντωμένο σύρμα προτείνεται να εγκατασταθούν δυο ειδικά κλισίμετρα υψηλής ακρίβειας να εγκατασταθούν στο πεδίο όπου θα είναι εγκατεστημένες οι κάμερες, έτσι ώστε να πραγματοποιείται με ακρίβεια ο ορισμός της κατακορύφου του συστήματος αναφοράς και έτσι ο μετασχηματισμός θα είναι περισσότερο ακριβής.

Στην περίπτωση αυτή δεν θα υπάρχει επιρροή του μετασχηματισμού στην ακρίβεια των ακτινικών και κατακόρυφων αποστάσεων και θα εξαρτώνται κυρίως από την ακρίβεια προσδιορισμού των σημείων και του σύρματος.

Σήμερα λόγω του υπάρχοντος εξοπλισμού και συνθηκών αυτό δεν είναι εφικτό.

Για αυτό γίνεται ιδιαίτερη αναφορά στην απόσταση στο χώρο η οποία είναι ανεξάρτητη από τα συστήματα αναφοράς.

Τέλος, ο ελάχιστος αριθμός καμερών που προτείνεται να εγκατασταθούν στο πεδίο για την αυτόματη λήψη φωτογραφιών χωρίς ανθρώπινη παρέμβαση είναι τέσσερις, όπου εξασφαλίζουν την επιθυμητή ακρίβεια προσδιορισμού των συντεταγμένων και των αποστάσεων.

INTRODUCTION

The elaboration of this thesis took place at CERN, and specifically at the EN-SMM-ESA group, which is affiliated with the surveying works at the organization.

The aim of this work is to develop a photogrammetric method in order to measure offset distances from fiducials with respect to a stretched wire.

In order to accomplish this task, several steps were required to be implemented.

First of all, an algorithm, which will be able to realize the automatic detection of the photogrammetric targets, which are either encoded or uncoded ought to be created. The part of the algorithm that concerns the detection of targets, was established around the *regionprops* function of the MATLAB, which is the software that was used to create the code.

By introducing several presuppositions, the detection of the targets can be enhanced and be more efficient, in terms of excluding objects that are not real targets.

The second step was to determine the 2D position of the center of each target precisely. This procedure required special care, in order to find the most suitable, reliable and precise method to determine the position. Methods as the calculation of the centroid, the weighted centroid and the determination of the center of the best-fitting ellipse were used. The method that predominated was the ellipse fitting by using the least squares adjustment. In this way, the best ellipse is adjusted on the edge points that are detected on a target from the subpixel edge detector. The fact that, the least squares are used in order to define the best ellipse, is advantageous, because an estimation of the quality and precision is provided through the standard deviations of the image coordinates of the center of the adjusted ellipse.

Since, the detection and the position determination for each target is completed on every single image, the homologous points should be referred to each other. The correspondence among the encoded targets can be achieved by the decoding of their code segments. For the uncoded targets, intersections should be applied by using the collinearity equations with the least squares, where estimations for the precision of the intersections can be provided and can be interpreted. When the precision of an intersection is below a defined threshold (typically ±50 μm) then, the two-targeted points are homologous.

After all the implementation of all the procedures concerning the targets, the wire needs also to be defined. This is carried out by using an algorithm for wire measurement already developed at CERN. This wire measurement algorithm provides on each image the 2D coordinates of two points that the wire passes through. These two points are on the edges of each image.

After the gathering of data for the wires and the targets, they need to be integrated together under the platform of the LGC2 where an adjustment is applied in order to determine them in the 3D space. In order to be able to execute LGC2, the data needs to be converted to the required LGC2 format.

Afterwards, the fiducials which are used for the offset measurements, need to be projected on the stretched wire. Their projection generates the projected points which are the ones that are used for the offset measurements. The second and last adjustment is later executed which provides the final 3D coordinates for both the fiducials and the projected points. Thus, the offset distances are calculated after the orientation of the coordinate system with one of each axis vertical.

Chapter 1

ABOUT CERN

1.1. General information about CERN

On this section, general information about CERN is being presented, focusing on when the institution was established and which countries are at this moment its member states. Afterwards, a more in-depth report is presented about the functionalities of EN-SMM-ESA section, where this study has been elaborated.

After the end of World War II, a group of visionary European scientists imagined the creation of a European atomic physics laboratory which would not only unite the scientists from different nationalities but allow them to share the knowledge among them. Louis de Broglie, who was a French scientist, gave the first official proposal for the creation of such a laboratory. Several conferences and meetings followed until the final formation of CERN on 29 September 1954 by the 12 founding member states which were Belgium, Denmark, France, the Federal Republic of Germany, Greece, Italy, the Netherlands, Norway, Sweden, Switzerland, the United Kingdom and Yugoslavia. Since then a couple of countries have joined the organization. The total number of member states until now is 22 (Fig. 1.1), with several other states having the status of associate member states (CERN History 2018).

At the European Organization for Nuclear Research, a large group of scientists, engineers and not only, collaborate together in order to investigate the structure of universe, by using complex instruments and machines to study the fundamental particles. Particles are accelerated to reach a speed close the speed of light and then to collide. This process finally, provides to the scientists clues and information about the interaction of the particles and nature. The most frequently used equipment that are used for particle physics at CERN are the accelerators and detectors. Accelerators are responsible for boosting of beams to high energies in order to collide with each other or with targets, while detectors are used to record these collisions.
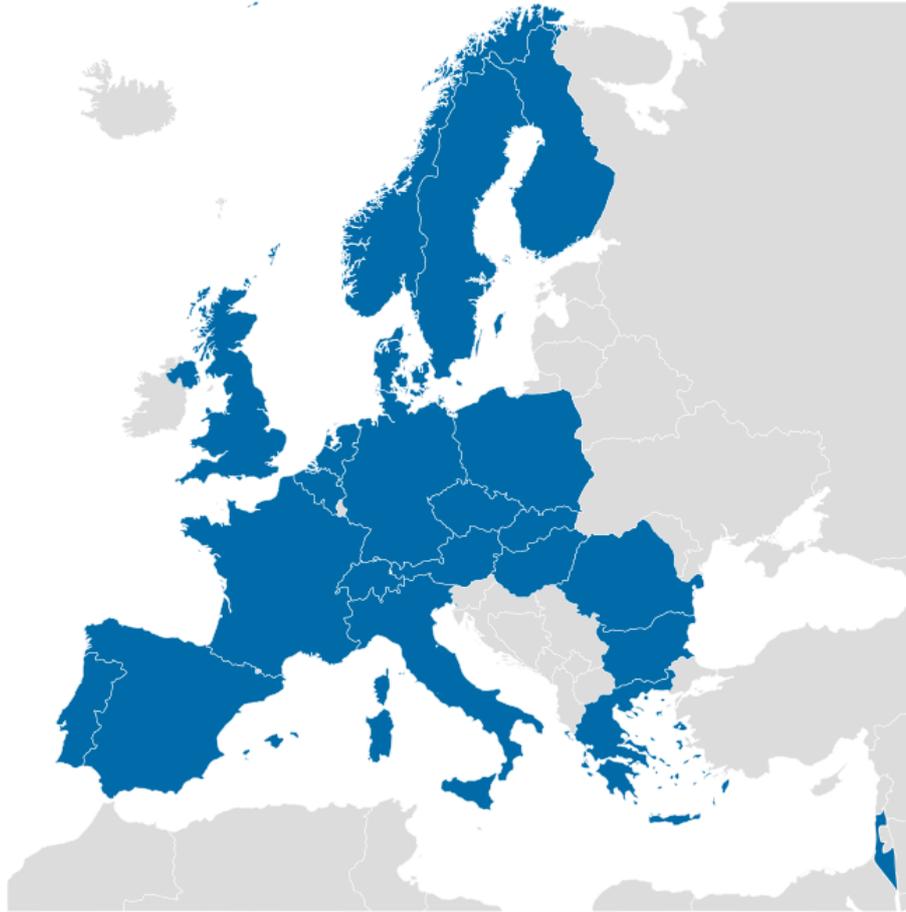
Figure 1.1 Member states of the CERN (wikipedia.org/wiki/CERN)

1.1.1. EN-SMM-ESA section

The present study has been elaborated at the EN-SMM-ESA section at CERN. These acronyms have the following meanings:

EN: Engineering

SMM: Survey, Mechatronics and Measurements

ESA: Experiments, Survey and Alignment

The SMM group is responsible and maintains centralized competence in Survey, Mechatronics systems, tests and Measurement. The Survey group is responsible for the geodetic metrology of the accelerators, the beam transfer and detectors for the whole CERN site. This includes the alignment of sections of accelerators, the metrology of detectors for assembly and positioning on the beam lines (CERN EN-SMM Group 2018).

The ESA section of the SMM group is in charge of the detector large scale metrology and alignment for CERN physics experiments. In general, some of the works of which the section is responsible are the installation, measurement and maintenance of geodetic infrastructure at the experiments, the metrology of detector prototypes and components, the geometrical measurements for the alignment of Physics detectors with respect to the corresponding accelerator and beam geometries and the mathematical respectively statistical processing and analysis of related survey data in order to supply the precise spatial position and orientation of the detectors.

1.1.2. CERN accelerators

Accelerators are used to speed up and increase the energy of a beam of particles by creating electromagnetic fields which accelerate them, steer and focus them. Accelerators might have two forms. The first one is to have a form of a ring where particles travel in a round loop and the second one is to have a linear accelerator (CERN Accelerators 2018).

The main components of an accelerator are:

- Radiofrequency cavities, which are metallic chambers that allow radio waves to interact with passing particle. Each time a beam passes the electric field in a radiofrequency cavity, an amount of energy from the waves is transferred to the particles, pushing them forwards.
- Vacuum systems, which are needed for the pipes in which particle beams travel.
- Various types of magnet, which serve different functions around a circular accelerator. In general, the more energy a particle has, the greater the magnetic field needed to bend its path.

The accelerator complex at CERN is a succession of machines that accelerate particles to increasingly higher energies. Each machine boosts the energy of a beam of particles, before injecting the beam into the next machine in the sequence (CERN Accelerators 2018). One of the most well-known accelerators is the LHC, whose main LHC experiments are ATLAS, ALICE, CMS and LHCb.

In figure 1.2 the CERN accelerator complex is presented with the ongoing experiments and the LHC which is the dark blue line.
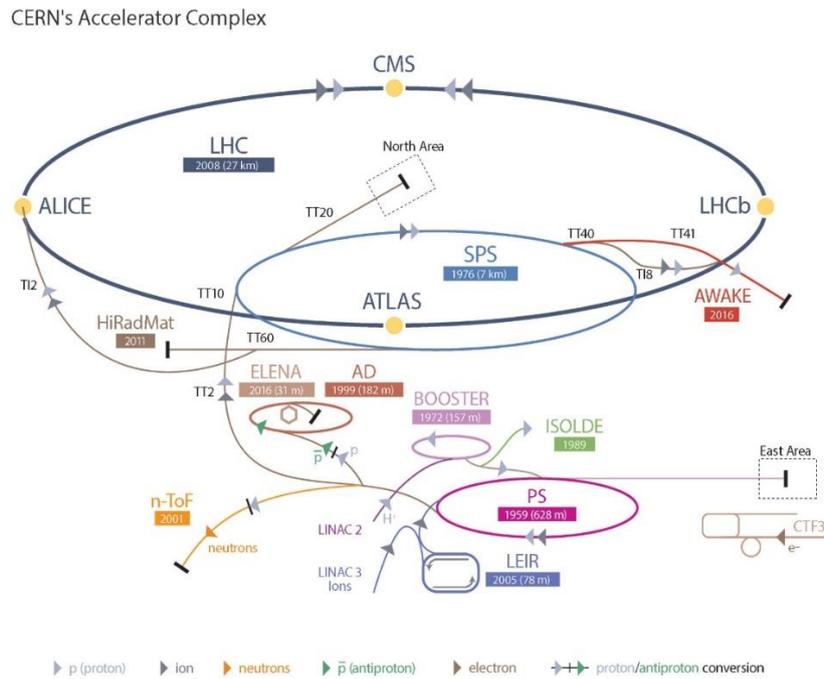
Figure 1.2 CERN accelerator complex (cds.cern.ch/record/2197559)

1.2. The Large Hardon Collider (LHC) accelerator

One of the biggest and most important works at CERN is the development of the Large Hardon Collider accelerator. The LHC is a 27 kilometers ring which has the ability to accelerate and boost the energy of particles along the way. A brief presentation about the LHC and its components is presented in this section. Subsequently in this section, the importance of alignment is highlighted and the various methods that have been used and can be used in the future in order to achieve high precisions are mentioned.

The Large Hadron Collider – LHC is the largest particle accelerator in the world at this moment with a circumference of 27 kilometers (Photo 1.1). Its operation began on 10th September 2008 and since then it is able to boost with high energy the particles along its way (CERN Large Hadron Collider 2018).

The accelerator is able to hold two high energy particle beams which travel in opposite directions, at a speed close to the speed of light, before they collide. A large number of magnets which are from different varieties and sizes are used to direct the beams at the accelerator. The majority of the magnets are dipole and quadrupole magnets. There are 1232 dipole magnets which are used to bend the beams and 382 quadrupole magnets which are used to focus the beams. Finally, after the

6

beams are accelerated, they collide at four points of the ring, where the four detectors which are ALICE, ATLAS, CMS and LHCb are located.
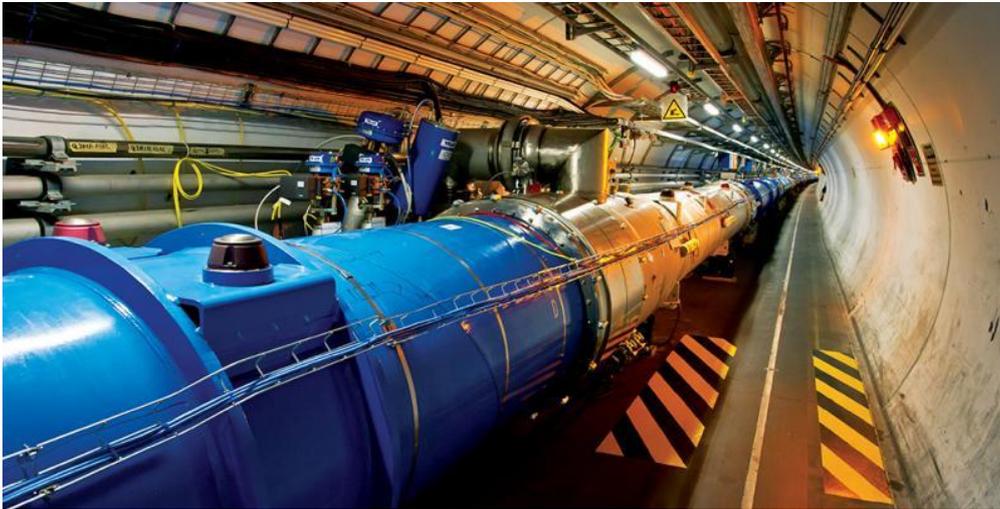
Photo 1.1 The LHC accelerator (home.cern/topics/large-hadron-collider)

The main components of the LHC accelerator are (LHC Machine Outreach Components 2018):
- Power converters which convert A.C. to the D.C. required by the magnets
- Beam dumps
- Magnets
- Cryogenics which use superfluid helium, which has unusually efficient heat transfer properties, allowing kilowatts of refrigeration to be transported over more than a kilometer with a temperature drop of less than 0.1 K.
- Vacuums and specifically LHC has three vacuum systems, insulation vacuum for cryomagnets, insulation vacuum for helium distribution line and beam vacuum.
- Collimator systems, which will protect the accelerator against unavoidable regular and irregular beam loss.
- Current leads transfer the current from warm into the cold mass of the magnets.

1.3. Survey and alignment activities

The alignment for the LHC magnets is essential for the stability of beams on their orbits. Until now, the radial alignment has been achieved thanks to ecartometry, a method that has been developed at CERN and for the vertical alignment, optical and digital levels are used. However, these

methods are manual and time consuming. Moreover, the human presence in the tunnel will gradually be limited because of the increased radioactivity of components exposed to the beam. This is why the Survey team is looking for more automatic ways in order to do the measurements.

Since the construction of the first accelerator which accelerated protons, the Proton Synchrotron in 1959, the Survey team had started to develop and to use tools for the alignment of various elements of machines. One of the most common tools and techniques used for the alignment is the usage of the stretched wires.

The principle of the measurements using stretched wires incorporate the measuring the shortest distance of a point B to a straight-line AC. Usually, such a simple geometry as it is previewed on figure 1.3 can be done just by measuring the angle ABC and the distances AB and BC. The line AC could be materialized with a laser beam (Quesnel J. 2008).
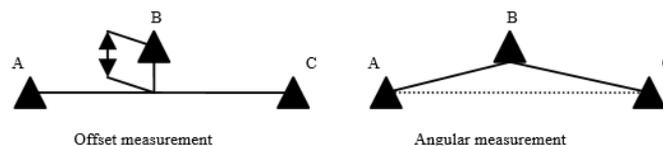
Figure 1.3 Principle of the offset measurement (Behrens A. 2016)

At CERN's accelerators, offset measurements are the main method for the radial alignment of components. In order to carry out these measurements ecartometry is implemented. For these measurements, ecartometers are installed on a fiducial which is on the magnet and then the perpendicular distance to a stretched wire is measured (Fig. 1.4).
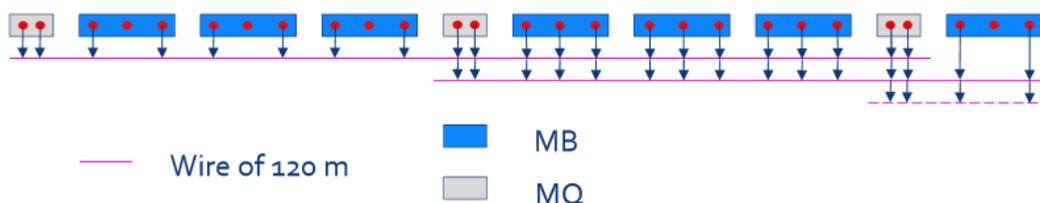
Figure 1.4 Scheme for ecartometry in LHC (Behrens A. 2016)

This method provides favorable precisions compared to other methods. For instance, at the LHC, the alignment precisions of 0.05mm or 50 µm have been achieved on a distance of 150m the along accelerator. This

precision is much better than any other that can be achieved with common instrumentation (Behrens A. 2016).

However, there is the disadvantage that the process is time consuming hence, not very efficient. Usually with the traditional equipment, a group of two persons can measure and cover around 500 meters of accelerator each day. This fact leads to the research to automate the procedure in order to avoid delays on the measurement itself but also save time and gain manpower.

Photogrammetric procedures are able to provide more automatic solutions and can be used as possible tools for ecartometry since in laboratory conditions a precision of less than ±10 μm for the wire measurement can be reached (Behrens A. 2016).

1.4. Objective of the thesis

The objective of this thesis is the development of an algorithm for the automatic detection and position determination of encoded and uncoded targets.

The developed algorithm includes several parts which (i) are the automatic detection of all the targets, (ii) their precise 2D image coordinates determination and (iii) the decoding of the encoded targets. An application of the algorithm was carried out on the cryomagnets of the LHC at CERN.

The aim of the application was the position determination of the fiducials which are uncoded targets and the calculation of their offset distance with respect to an installed stretched wire.

The idea of the development of such an algorithm started when tests revealed that photogrammetric process is able to provide wire measurement precisions of less than ±10 μm (Behrens A. 2016). When the first results indicated that wire measurements can be carried out precisely, there was the need to develop an algorithm for the 2D determination of the wire on several images. With this algorithm it is possible to extract the image coordinates of two points through which the wire passes. Since this information became available, the next step was to develop an algorithm for the position determination of the fiducials. From that position offset distance with respect to the stretched wire is going to be measured.

In general, the fiducials are fixed points which are used as reference marks and their position (Photo 1.2), which is linked with the inner geometry of the cryogenic magnet, was determined by a procedure called fiducialisation. Due to the fact that the inner part of the magnets is inaccessible, the role of the fiducials is very important for the surveying works, especially for the task of the accelerator alignment.

Cryogenic magnets (Fig.1.5) are the parts which constitute the LHC. Cryogenic magnets, use cryogenic techniques in order to cool the superconducting magnets. It would have been unable to operate the magnets without the use of cryogenic systems, a fact that reveals the importance of the usage of such techniques.

The superconducting magnets at the LHC are able to maintain temperatures about -271.3°C which enable the niobium-titanium wires to reach a superconducting rate. On the top of these magnets, the fiducials are installed which are essential for the accelerator alignment (Rossi L. 2003).

In the future, in order to automate the measurement procedure and to avoid the exposure to high radiation levels, a structure which will be able to execute the measurements should be constructed and used. A machine that is able to carry out such tasks is the survey collimator train. At this moment, the train is developed in order to make remote controlled visual inspections and radiation surveys in the LHC (Behrens A. 2010). The main parts of the train as they are presented in the photo 1.3 are the traction unit, sensor unit, control unit and battery unit.

The idea is to install on the survey collimator train a specifically defined frame which will carry some cameras, which are going to be installed on specific positions. In this way, a pre-calibration of the cameras for the determination of the interior orientation should be done. Also the parameters of the interior orientation can be computed, the relative position of the cameras can be easily determined and the exterior orientation of the cameras, which includes their rotations, can be specified.

Since all this information is available, the wire measurement and the target positioning of the fiducials can be carried out automatically without the presence of a human. The calculation of the offset distance can be finally accomplished automatically since the 3D position of the fiducials and the wire have been specified. The train makes the offset measurements along the whole track of the LHC feasible, because it can be performed automatically, without the presence of any personnel and it

is not so vulnerable to radiation which is a prohibitive factor for the humans.
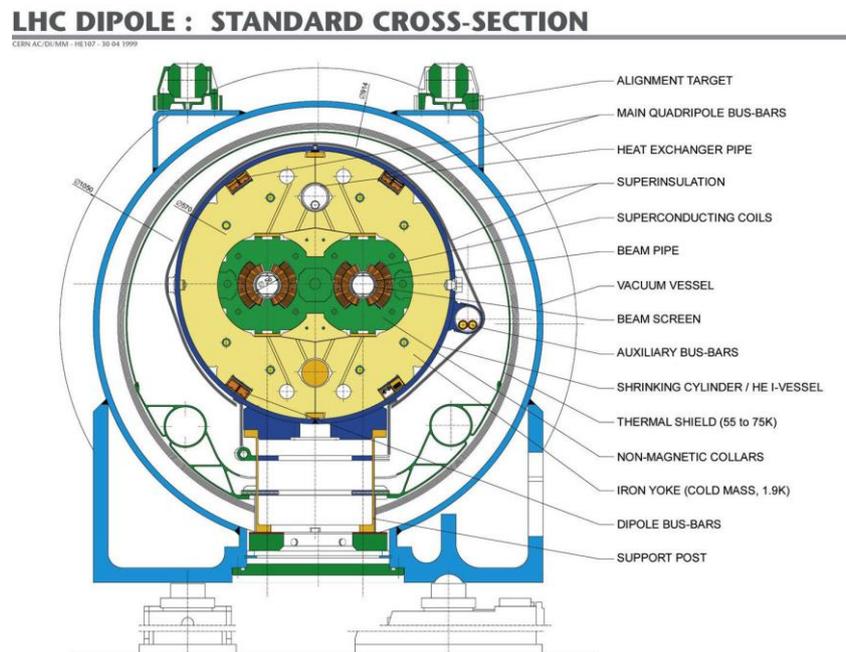
Figure 1.5 Cross section of the LHC Main Dipole in its cryostat
(Rossi L. 2003)

Photo 1.2 Fiducials on a LHC dipole magnet
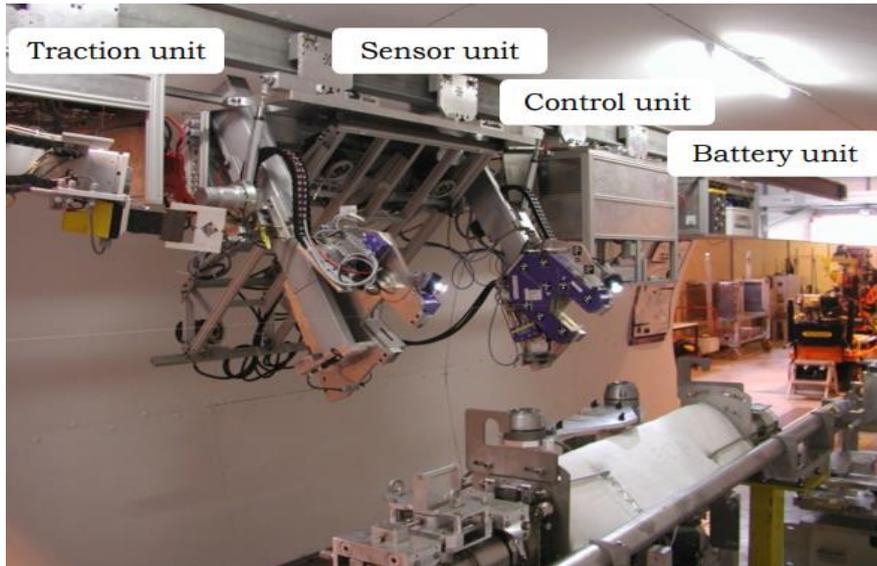
Photo 1.3 Parts of survey collimator train

1.4.1. Target detection

The first step in order to determine the position of the targets, is to detect them. The detection of the targets is a key procedure because it provides the total number of the targets found and also the approximate coordinates of these targets in the local coordinate system of the image. The targets usually used, have a round shape with specific code segments around their circle. Due to their geometry and features, various algorithms have been tested on MATLAB interface, like the detection of specific features on images, circular Hough transformation and analysis of connected objects on a binary image using *regionprops* function. The most reliable results (presented in chapter 3) have been achieved by using the *regionprops* function, on which the proposed algorithm has been based.

Photo 1.4 shows that with the *regionprops* all the targets on the wooden board have been detected. This example proves the high reliability of this method. In the next chapters, the conditions used in order to achieve the detection will be discussed.

Photo 1.5 represents the outcome of the circular Hough transformation (CHT) for this specific example. The results of the usage of this algorithm on this image reveals that with this method, most of the targets can be detected. However, with this algorithm each image needs special treatment, depending on the illumination and the angle that the picture

has been captured, which influence the circular shape of the targets. Due to the fact that they get elliptical shapes in the perspective view, the conditions are different and the sensitivity of the algorithm has to be changed, thus it is not possible to automatize the detection of targets using this algorithm.

The same algorithm has been run with photo 1.6, but in this case the sensitivity is changed to 0.8. At this point, the targets identified are much fewer than previously where the sensitivity is defined to 0.9.
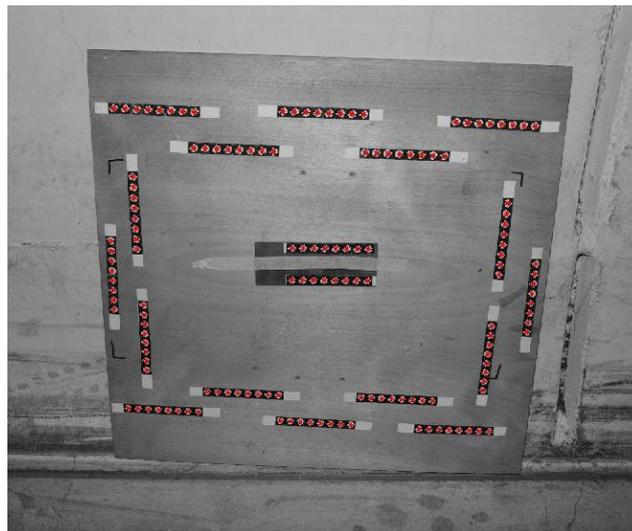
Photo 1.4 Detection of targets using regionprops
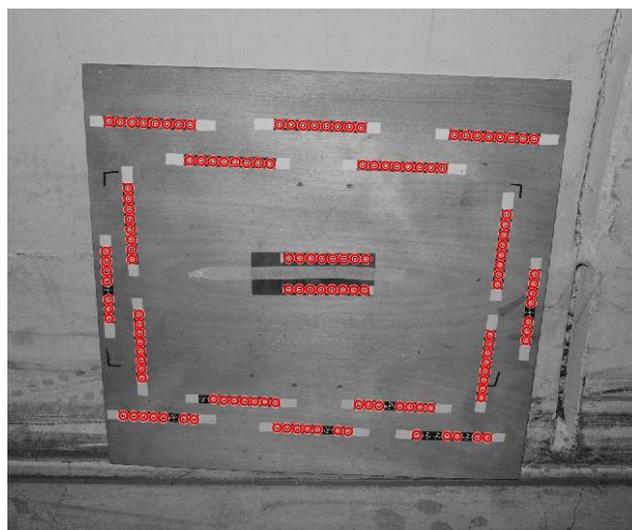
Photo 1.5 Detection of targets using CHT with sensitivity 0.9
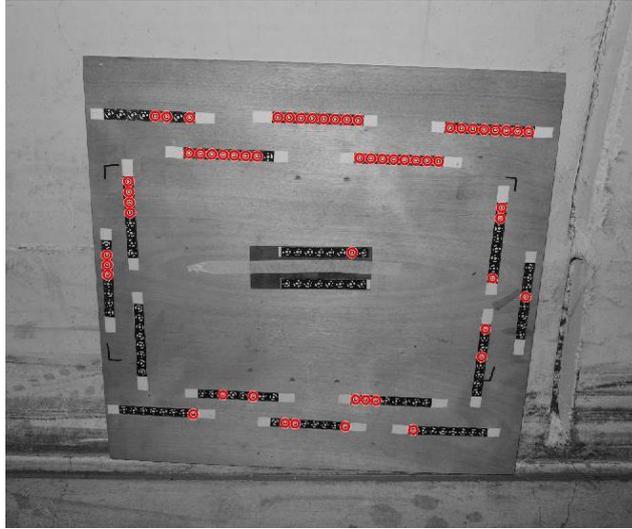
Photo 1.6 Detection of targets using CHT with sensitivity 0.8

1.4.2. Target position determination

Target position determination is one of the most essential parts of this thesis. Various ways and algorithms have been tested in order to achieve the highest possible precision and reliability. In the chapter where the target position determination is going to be analyzed in detail, emphasis is given to the ellipse fitting method, because of its high reliability on the measurement and the precision that this method provides. Several other methods have been tested such as cropping and resizing the cropped image by a factor in order to increase precision of the regionprops. Each method has its advantages and disadvantages which have to be taken into consideration in order to conclude to the most suitable method to achieve high precision target position determination. In photo 1.7, the centers of the ellipses determined from ellipse fitting are plotted on the targets.
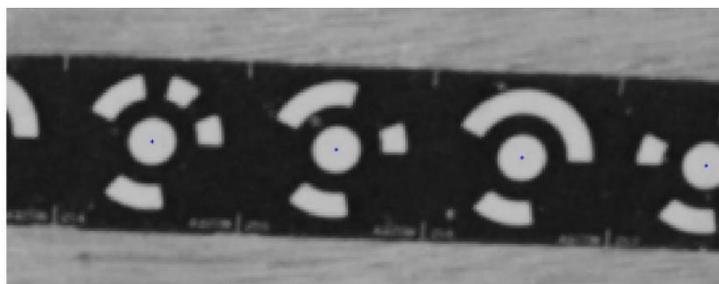
Photo 1.7 Centers of the targets determined by ellipse fitting

1.4.3. Target decoding

As it is clear from the previous figures, most of the targets used during the internship, have been coded targets. The AICON software is able to generate coded targets of 12, 14 and 20 bits. Each of these targets has a unique code, which represents their ID (Photo 1.8). This ID is helpful to recognize and correlate the targets that have been captured with a camera in a great number of images. An example a successful decoding is represented at the photo 1.9.
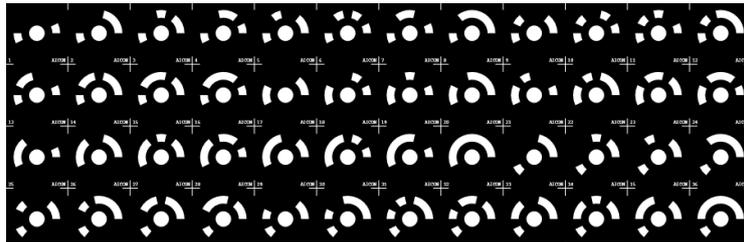
Photo 1.8 14bit coded targets generated by AICON

The decoding method developed and used in this thesis is based on the minimization of the binary number created from the code segments. In particular, from 14bit coded target, a sequence of 14 numbers that are 0 or 1 will be created by it and 14 different sequences can be generated. Each sequence represents a specific number, from which the smallest number should be chosen. Then the number that is found will correspond to a specific code that the AICON software provides.

In chapter 5, an analysis in detail is going to be focused, concentrating on the algorithm that has been developed for the target decoding.
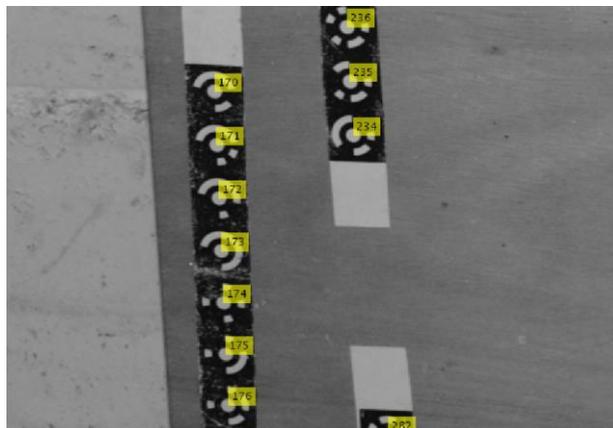
Photo 1.9 Target decoding

Chapter 2

CAMERA GEOMETRY AND STRETCHED WIRE OFFSET MEASUREMENT

2.1. Close range photogrammetry at CERN

Photogrammetry includes techniques of image measurement, which provide the ability to obtain the shape and the position of an object by using one or more photos.

The aim of photogrammetric measurement is the 3D representation of an object (Luhmann T. 2006). In general, there are several types of photogrammetry, among them photogrammetry and close-range photogrammetry.

By definition, close-range photogrammetry is simply photogrammetric data collection and processing. Collection methods can be both ground or aerial based, and the final output can be rendered either two or three dimensionally (Salmon J. 2018).

Due to the wide variety of applications, close range photogrammetry, can be characterized as interdisciplinary.

In this diploma thesis, close range photogrammetry will be used for surveying works. The images used were captured in such a way that the distances between the camera and the objects to be analyzed were limited to 1-2 m (Photo 2.1).

On the following subchapters, more in-depth information is going to be provided concerning the equipment and in general the photogrammetric procedures.

As it has been mentioned previously, on the accelerators at CERN, offset measurements are carried out by ecartometry which is the main method for the radial alignment of the components. This method is manual and time consuming.

At CERN digital photogrammetry has been used for nearly 20 years and has proven its efficiency during the construction of the LHC experiments with high precision and flexibility.
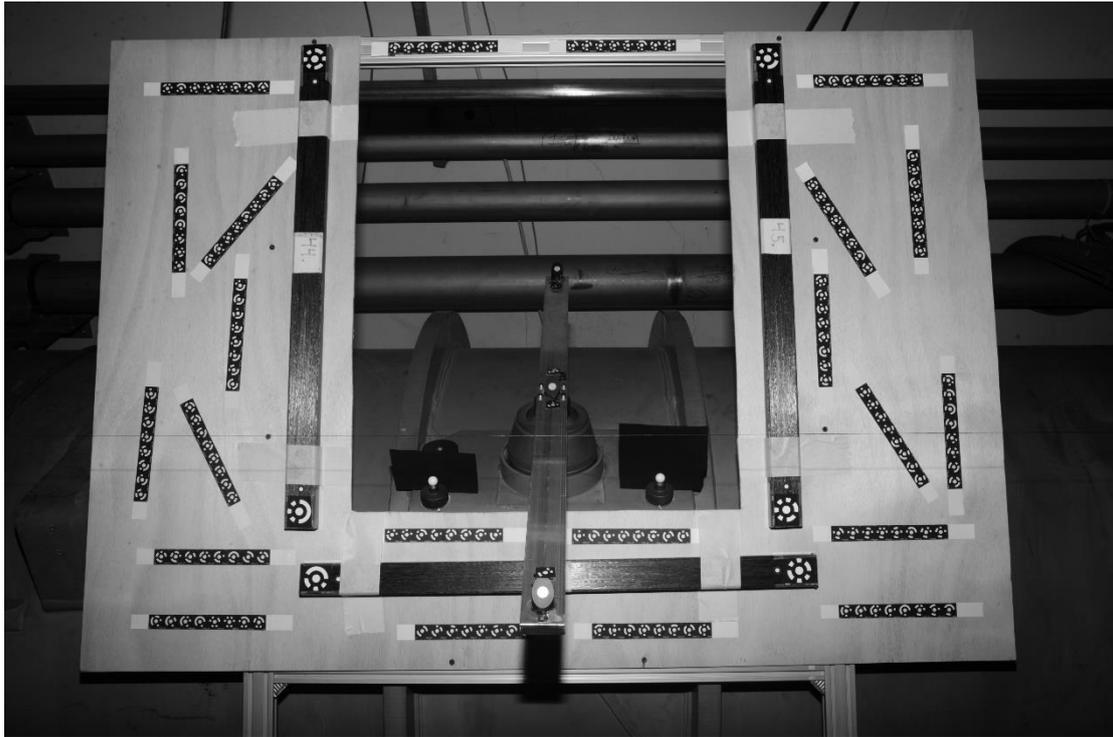
Photo 2.1 Close range photogrammetry at the LHC

CERN uses the AICON photogrammetric software since 1997 (Photo 2.2) but in recent years the integrated feature measurement attracted interest. Through this software, it is possible to measure curved lines in different images (Behrens A. 2016).

One of the greatest advantages of photogrammetry is that it offers the ability to measure simultaneously wires and targets. In this way the wire and fiducials can be determined simultaneously. Nowadays, camera resolution is high enough to distinguish and recognize the wire and the targets at short distances, thus the measurements can be carried out automatically or semi automatically (Mergelkuhl D. 2015).

2.2. Instrumentation

The EN-SMM-ESA section has the complete equipment of digital photogrammetry with digital cameras, several lenses, flashes, tripods, scale bars and different types of targets. The last acquired camera is the Nikon D3X camera (Photo 2.3). It is provided with a CMOS sensor of 35.9 mm x 24.0 mm with a resolution of 24.5 MP. The camera specifications are presented in the table 2.1.

A remote flash Nikon Speedlight SB-700 is mounted on the camera while taking pictures. The section has all sorts of targets that can be recognized by the AICON software. The targets can be encoded targets or simple circular targets without code (uncoded). Also, some targets might be reflective or not depending on the purpose of their use. Metal targets (Photo 2.4) might also be used on the fiducials (Scandella L. 2017).

The photo 2.5 presents a fully photogrammetric equipment by AICON.

Photo 2.2 Detection, measurement and target decoding by AICON

Type	Nikon D3X
Resolution	6048 x 4032 pixels
Pixel size	5.9 μm

Table 2.1 Specifications of the camera

Photo 2.3 Nikon D3X camera
(fotointern.ch/archiv/2008/12/01/nikon-d3x-jetzt-mit-vollformat/)
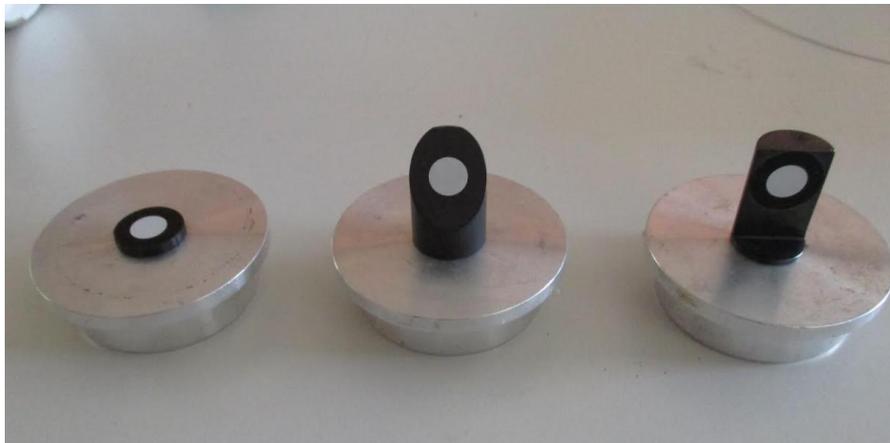
Photo 2.4 Uncoded metal targets usually used on the fiducials

Photo 2.5 Photogrammetric equipment by AICON
(accurexmeasure.com/dpa-inspect.htm)

2.3. Camera calibration

The calibration of a camera is performed in order to determine its interior geometrical parameters. During the process of camera calibration, the interior orientation of the camera is determined. The interior orientation parameters describe the inner geometry and characteristics of a camera (Schenk T. 2005).

There are several processes to calibrate a camera. One is to perform a calibration under laboratory conditions, and another is the auto calibration, where the parameters of the interior orientation are calculated during the bundle adjustment. Cameras should be calibrated periodically because exterior factors such as stress, temperature change and pressure differences may change some of the interior orientation parameters, but also when parameters as focal length aperture and others are changed by the user. All these change the interior geometry in a camera and a calibration is required.

2.3.1. Interior orientation

The interior orientation defines, among other parameters, the position of the perspective center and the radial distortion curve. A camera with known interior orientation is equivalent to a "metric camera" if the orientation elements are stable. An amateur camera, for example, is non-metric because the interior orientation changes e.g. every time the camera is focused.

A camera can be modelled as a spatial system which consists of a planar imaging area and the lens with its perspective center. The parameters of interior orientation of a camera define the spatial position of the perspective center, the principal distance and the location of the principal point. They also encompass deviations from the principle of central perspective to include radial and tangential distortion and often image affinity and orthogonality (Luhmann T. 2006).

The parameters of interior orientation are :

- Principal point H′:
    The projection of the perspective center on the image plane with image coordinates (x'_0, y'_0), for standard cameras approximately equal to the center of the image: $H' \simeq M'$

- Principal distance c:

   Normal distance to the perspective center from the image plane in the negative z′ direction; approximately equal to the focal length of the lens when focused at infinity: c≃f

- Parameters of functions describing imaging errors:

   Functions or parameters that describe deviations from the central perspectrive model are dominated by the effect of radial-symmetric distortion Δr′

The figure 2.1 represents visually the aforementioned parameters.
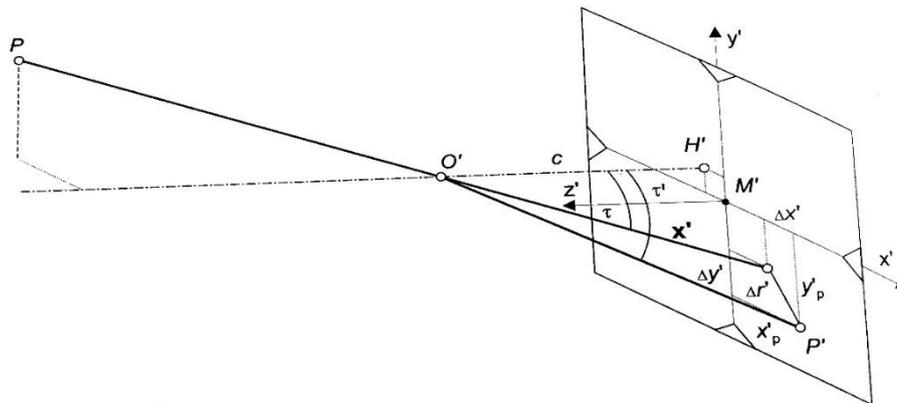
Figure 2.1 Interior orientation (Luhmann T. 2006)

It is important to mention that for digital cameras fiducial marks to define the coordinate system are not required. The image coordinate system of digital cameras usually has as origin of the system the upper left corner pixel center, creating a left handed coordinate system, which is linked with the chip of the sensor.

If these parameters of interior orientation are known, coordinates of a point on an error free image can be defined as below:

$$X' = \begin{bmatrix} x' \\ y' \\ z' \end{bmatrix} = \begin{bmatrix} x'_p - x'_0 - \Delta x' \\ y'_p - y'_0 - \Delta y' \\ -c \end{bmatrix} \tag{2.1}$$

Where

$x'_p,\ y'_p$:   measured coordinates of point P′ on the image

$x'_0,\ y'_0$:   coordinates of the principal point H′

$\Delta x',\ \Delta y'$:   axis-related correction values for imaging errors

The measured image coordinates x'_p, y'_p are corrected by a shift of the principal point x'_0, y'_0, thus this results to image coordinates related to the principal point :

$$x^o = x'_p - x'_o \tag{2.2}$$

$$y^o = y'_p - y'_o \tag{2.3}$$

Where image radius distance from the principal point is:

$$r' = \sqrt{x^{o2} + y^{o2}} \tag{2.4}$$

Thus, the image coordinates x^o, y^o are corrected by:

$$x' = x^o - \Delta x' \tag{2.5}$$

$$y' = y^o - \Delta y' \tag{2.6}$$

This results to the corrected image coordinates x', y'.

2.3.2. Radial distortion

Radial distortion constitutes the major imaging error for most camera systems. The distortion curve can be expressed by a polynomial with parameters K_1 to K_n:

$$\Delta r'_{rad} = K_1 r'^3 + K_2 r'^5 + K_3 r'^7 + \cdots \tag{2.7}$$

In most cases the coefficients can be reduced to the second or third term without any significant loss of accuracy. The image coordinates are corrected proportionally:

$$\Delta x'_{rad} = x' \frac{\Delta r'_{rad}}{r'} \tag{2.8}$$

$$\Delta y'_{rad} = y' \frac{\Delta r'_{rad}}{r'} \tag{2.9}$$

The distortion parameters defined in equation (2.7) are numerically correlated with image scale or principal distance. In equation (2.7) a linear part of the distortion function is added which leads to the rotation of the distortion curve forcing it to pass for second time from the 0 at the r´ axis (Fig. 2.2). Then formula 2.7 can be expressed as (2.10)

$$\Delta r'_{rad} = K_0 r' + K_1 r'^3 + K_2 r'^5 + K_3 r'^7 \qquad (2.10)$$
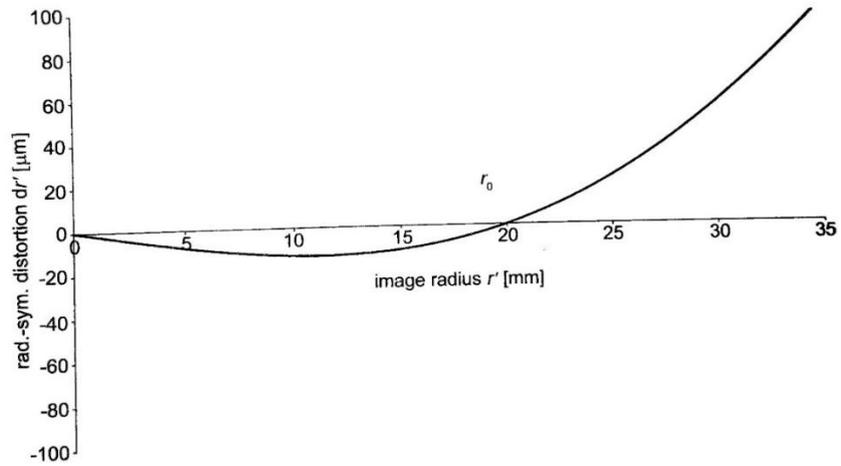
Figure 2.2 Distortion curve passing two times from dr'=0μm
(Luhmann T. 2006)

Alternatively, there is the following polynomial expression:

$$\Delta r'_{rad} = A_1 r' \left(r'^2 - r_0^2 \right) + A_2 r' \left(r'^4 - r_0^4 \right) + A_3 r' \left(r'^6 - r_0^6 \right) \quad (2.11)$$

The rearrangement of equation (2.11) to equation (2.12) leads to the same result as equation (2.10) (Luhmann T. 2006) :

$$\Delta r'_{rad} = A_1 r'^3 + A_2 r'^5 + A_3 r'^7 - r'(A_1 r_0^2 + A_2 r_0^4 + A_3 r_0^6) \quad (2.12)$$

A typical effect of radial distortion is presented at the figure 2.3.
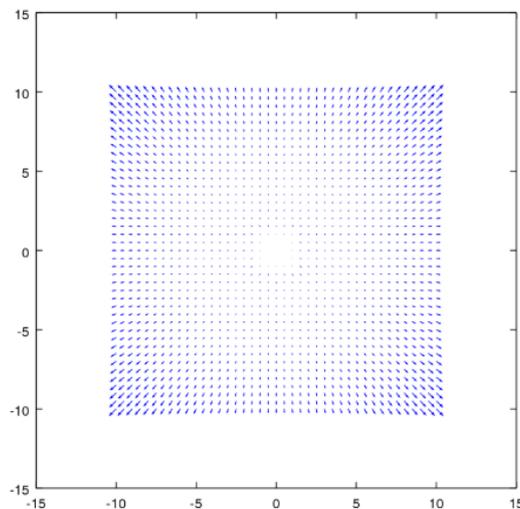
Figure 2.3 Effect of radial distortion (stackexchange.com)

2.3.3. Tangential distortion

Tangential distortion or radial asymmetric distortion is mainly caused by decentering and misalignment of individual lens elements within the objective (Luhmann T. 2006). It can be expressed by the formulas (2.13) and (2.14):

$$\Delta x'_{tan} = B_1\left(r'^2 + 2x'^2\right) + 2B_2 x'y' \qquad (2.13)$$

$$\Delta y'_{tan} = B_2\left(r'^2 + 2y'^2\right) + 2B_1 x'y' \qquad (2.14)$$

Compared to the radial distortion, the tangential distortion shows much smaller quantities for most quality lenses.

A typical effect of radial distortion is presented at the figure 2.4.
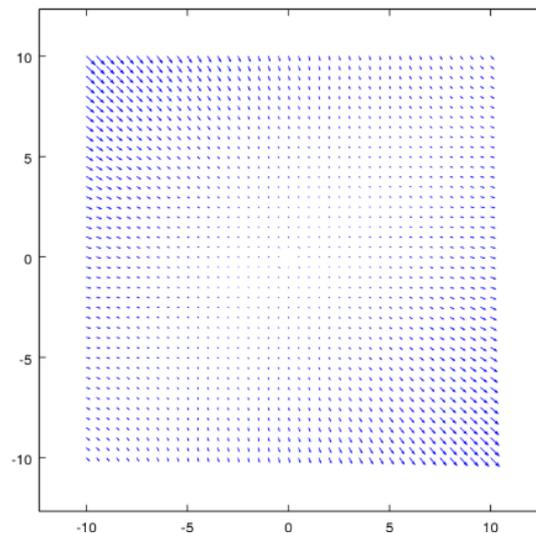
Figure 2.4 Effect of tangential distortion (stackexchange.com)

2.3.4. Affinity and shear

Affinity and shear are used to describe deviations of the image coordinate system with respect to orthogonality and uniform of the coordinate axes. On digital cameras these effects can be produced if the sensor has its light sensitive elements with rectangular or even parallelogram shapes rather than square. The formulas (2.15) and (2.16) provide the corrections for these phenomena.

$$\Delta x'_{aff} = C_1 x' + C_2 y' \tag{2.15}$$

$$\Delta y'_{aff} = 0 \tag{2.16}$$

2.3.5. Total correction

All the individual correction terms that have been mentioned until now can be used to correct the most typical photogrammetric error sources and they can be summarized at the following equations (Luhmann T. 2006):

$$\Delta x' = \Delta x'_{rad} + \Delta x'_{tan} + \Delta x'_{aff} \tag{2.17}$$

$$\Delta y' = \Delta y'_{rad} + \Delta y'_{tan} + \Delta y'_{aff} \tag{2.18}$$

In order to correct the measured image coordinates completely from the distortion, the correction should be applied iteratively. That means that once the image coordinates of a point are corrected one time for the distortion, then these corrected coordinates should be used again at the procedure of distortion correction, until the $\Delta x'$ and $\Delta y'$ of two consequetive iterations provide the almost same value. Then the final image coordinates are entirely free of distortion.

2.4. Evaluation of stretched wire measurements

The usage of the stretched wire is a technique which has been mainly developed at CERN and it is traditionally used for the alignment of the accelerators. The method has been proven to be precise and accurate enough for the works that are required. Until recently, the treatments and measurements on the wire have been done manually, however studies have shown that photogrammetry is able to provide adequate accurate results also efficiently with a lot of advantages (Vendeuvre C. 2016).

The principle of the measurements can be summarized as the shortest distance of a point to a straight line. Figure 1.3 presents the principle (Quesnel J. 2008).

In addition to the standard photogrammetric projects with signalized target measurement, orientation and calibration up to the calculation of 3D coordinates, photogrammetry gives the possibility to measure curved lines if they are visible in different images. In the recent years due to the increased camera resolution it is possible to measure stretched wires of 0.3 mm diameter at limited distances of 1-2 m (Behrens A. 2016).

Photogrammetry has also several advantages in this case because it is a non-contact measurement technique, which is advantageous for automation. Collimator train already uses photogrammetry for measurement of collimator fiducials and both targets and wires can be measured simultaneously.

Due to the usage of photogrammetry and the appropriate treatments, the identification, measurement and the calculation of the coordinates on the stretched wires can be carried out with a typical precision of ±6.5 μm /m.

Photo 2.6 Detected wire

Photo 2.6 is an image captured at LHC where the stretched wire is visible and detected. For the stretched wire identified, the image coordinates at the edges of the image are calculated.

The development for the detection and measurement of the stretched wire has been elaborated by Lucie Scandella who was also a Trainee at CERN (Scandella L. 2017).

Photo 2.7 At work in the LHC

Photo 2.7 presents a photogrammetric work in the LHC during the shutdown in July 2018, where a stretched wire, encoded and uncoded targets were mounted on the accelerator for the offset distance calculation.

Chapter 3

DEVELOPMENT OF AN ALGORITHM
FOR THE TARGET DETECTION

3.1.   Photogrammetric targets

A photogrammetric target is an artificial object of known geometry, which is placed on the field when taking pictures. Usually the targets should be clearly distinguishable in the images and present an undisputable central point. The targets may be uncoded or encoded (Photo 3.1).

The usage of first ones is limited to the identification and measurement, while the latter can also be decoded thanks to their code segments.

The encoded targets usually include a small circle which will be used for the measurement in order to find the center and segments that are around the circle, whose main purpose is to provide a specific code to each target (Manolopoulos K. 2017).
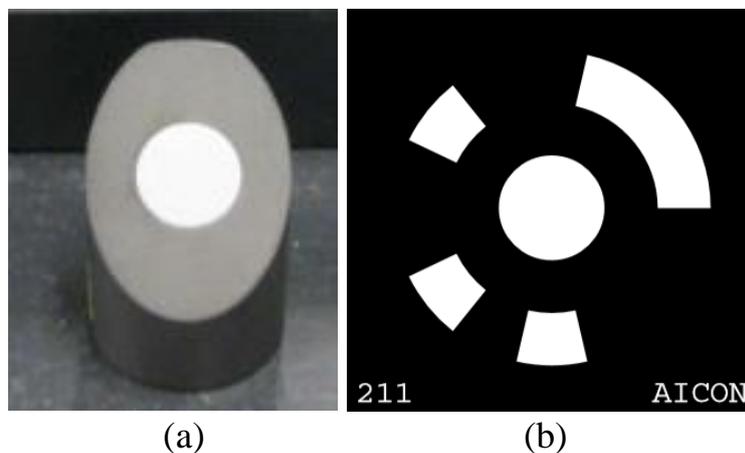
(a)   (b)
Photo 3.1 Uncoded (a) and encoded (b) targets

In close range photogrammetry, targets are very essential features which are used for various photogrammetric tasks. However, without the ability of automatic detection of the targets, the effectiveness of metrology systems abates, and the time required for various tasks increases due to the need for manual or semi-automatic measurement of targets on the images. The need for faster and more objective detection of targets in a

project which may include many images leads to the research for a more automatic way for recognition and pointing of the photogrammetric targets.

The most common targets that are used by CERN EN-SMM-ESA section are the targets represented by figures 3.1 and 3.2. The first target is an anodized aluminum target and the second is a conventional white target. Targets such as the figure 3.2 can be produced as retro reflective also.

Generally, retro reflectors, reflect light very efficiently back to the light source. For example, they are typically 100 to 1000 times more efficient in returning light than a conventional white target. A low power flash mounted on the camera is used to illuminate the targets. Hence, the targets can be detected easily. In addition, as the targets are illuminated completely by the flash, the target exposure is independent of the ambient illumination. Pictures can be taken in bright light or total darkness and the target exposure will be the same. The fact that the environment does not affect the outcome of the image when retro reflective targets are used, makes the whole process very convenient.

Although retro reflective targets have several advantages over conventional targets, they tend to lose their special reflective properties when viewed at steep angles, becoming dim and unmeasurable. For best results, the targets should not be viewed more than 60° to 65° off-axis (Geodetic Systems 2018). In addition, some other factors, which may make both retro reflective and conventional targets unmeasurable, are the dust and dirt, which may be on the targets and prohibit their detection.

3.2. MATLAB as development environment

The development environment is very crucial for the entire development of the algorithm, since the libraries that are available on each environment should be used in their own specific way and also the syntax and the rules should be obeyed. Furthermore, the coordinate system of the development environment should be determined in order to be able to do transformations between various coordinate systems.

The interface within which the algorithm has been developed is MATLAB (Fig. 3.1). MATLAB is a high-performance language for technical computing and it integrates computation, visualization and programming environment. MATLAB provides an interactive environment and the basic data element that it uses is the array (Houcque D. 2005).

The version of MATLAB that the algorithm has been developed in is MATLAB R2016b. The interface of MATLAB is very convenient for programming because it includes many libraries with functions that are ready to use.
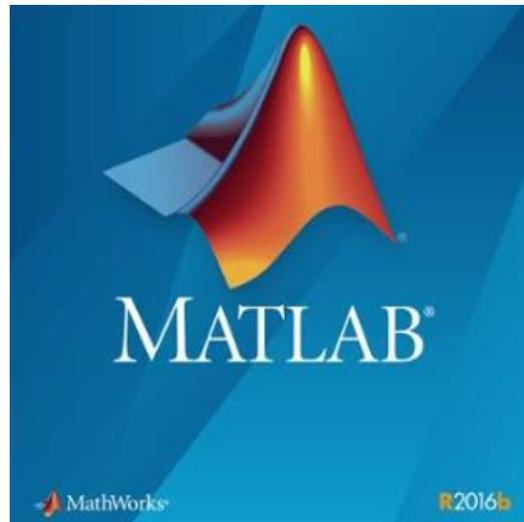
Figure 3.1 MATLAB R2016b logo

3.3.   Image elaboration parameters

3.3.1. Coordinate system

Every image in MATLAB has its own coordinate system. The user can specify locations in images using various coordinate systems. Coordinate systems are used to place elements in relation to each other. Coordinates in pixel and spatial coordinate systems relate to locations in an image.

Pixel coordinates enable the user to specify locations in images. In the pixel coordinate system, the image is treated as a grid of discrete elements, ordered from top to bottom and left to right (Fig. 3.2).
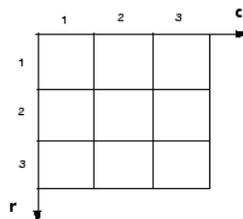
Figure 3.2 Pixel indices (Mathworks Coordinate Systems 2018)

31

For pixel coordinates, the number of rows, (r), downward, while the number of columns, (c), increase to the right as it is shown on figure 3.2. Pixel coordinates are integer values and range from 1 to the length of the row or column.

Spatial coordinates enable to specify a location in an image with greater detail than pixel coordinates (Fig. 3.3). In the spatial coordinate system, positions in an image are represented in terms of fractions of (Mathworks Coordinate Systems 2018).
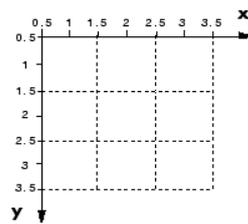
Figure 3.3 Spatial coordinate system
(Mathworks Coordinate Systems 2018)

Because each image has its own coordinate system, calculations and transformations from the coordinate system of an image to another coordinate system must be carried really carefully.

3.3.2. Input parameters

One of the first steps of the algorithm is to input some parameters. The parameters that are requested to be input are:

- The bit value of targets (12, 14 or 20)
- The type of targets, if they are retro reflective or conventional
- The color of the targets (White or Black)
- The minimum diameter of the targets in pixel
- The maximum diameter of the targets in pixel
- The maximum value for $\frac{a}{b} = \frac{semi\ major\ axis\ of\ an\ ellipse}{semi\ minor\ axis\ of\ an\ ellipse}$, for which the value 3 is recommended
- The preprocessing method for the grayscale image

3.3.3. Image preprocessing

Before, the automatic target detection, several image preprocessing are required in order to enhance the reliability of the algorithm.

The user must different kind of preprocessing depending on the project. There are three different ways of image preprocessing which are proposed. The first one includes an edge preserving smoothing filter called guided filter, while the second includes a Gaussian filter which is a smoothing filter which is typically used to reduce the noise. However, for both preprocessing procedures an adaptive histogram equalization will be implemented. The third one which is recommended for the most cases, uses image sharpening in order to enhance the edges and the contrast of each target which is helpful later for the binarization of the image.

It should be mentioned that depending on the environment, the adaptive histogram equalization might not be enough in order to provide the optimum results. Under some circumstances, the outcome might be even worse than the original image.

3.3.3.1. Adaptive histogram equalization

The histogram equalization algorithm has been a conventional image enhancement algorithm known for its simplicity and efficiency. It adjusts the gray level of an image according to the probability distribution function of the image and enlarges the dynamic range of the gray distribution to improve visual effects of the image. The histogram equalization algorithm may be divided into two types: local histogram equalization and global histogram equalization (Zhu Y. 2012).

Adaptive histogram equalization is an image processing technique that is used to enhance the contrast on an image. It differs from simple histogram equalization, in that the adaptive method computes several histograms, each corresponding to a distinct section of the image, and uses them to redistribute the illumination values of the image. It is therefore suitable for improving the local contrast and enhancing the definitions of edges in each region of an image (Komal Vij 2011).

Ordinary-global histogram equalization uses the same transformation that comes from the image histogram to transform all the pixels. This works well when the distribution of pixel values is similar throughout the image. However, when the image contains regions that are significantly lighter

or darker than most of the image like in our case where the targets might be black or white, the contrast in those regions will not be sufficiently enhanced.

Adaptive histogram equalization improves on this by transforming each pixel with a transformation function derived from a neighborhood region. In its simplest form, each pixel is transformed based on the histogram of a square surrounding the pixel.
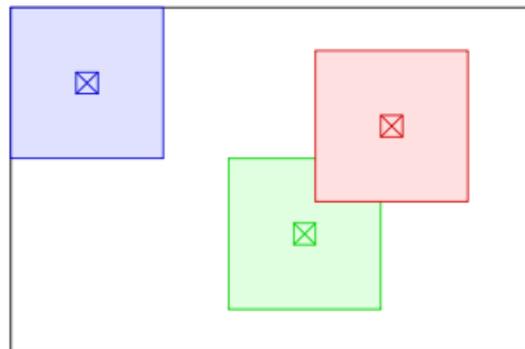
Figure 3.4 Pixel neighborhoods for adaptive histogram equalization
(wikipedia.org/wiki/Adaptive_histogram_equalization)

Photo 3.3 presents that the targets after the adaptive histogram equalization have an increased contrast. However, many texture and minute elements have also been illuminated due to the increase of the contrast, for which there is no interest and they may even increase the processing time at the next phases.

The implementation of the global histogram equalization does not provide as satisfying results as the adaptive histogram equalization. For instance, the lower left corner of photo 3.2 is not so well illuminated and the intensity values there are lower compared to the whole image, thus some issues might be faced with the automatic detection there. In these cases, the global histogram equalization might provide poor results on some specific targets. Hence, on the processed images after the implementation of histogram equalization the targets that might be on the dark regions, might have after the processing dark tones and might not be distinguished easily from their background. An example of the poor results of the global histogram equalization is illustrated in photo 3.4.
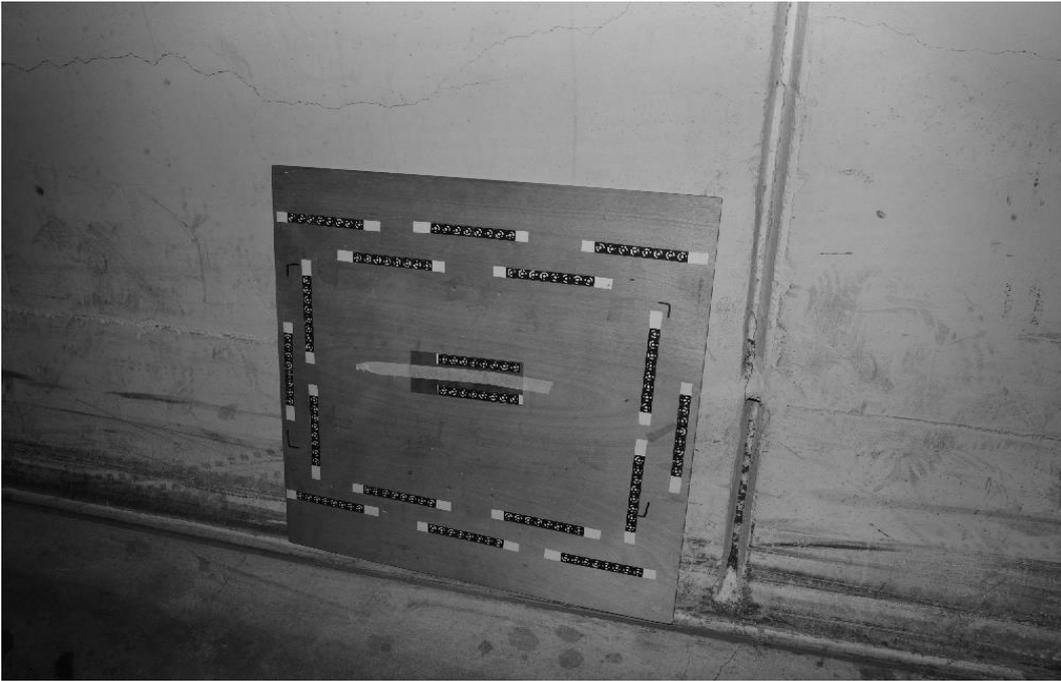
Photo 3.2 Original grayscale image
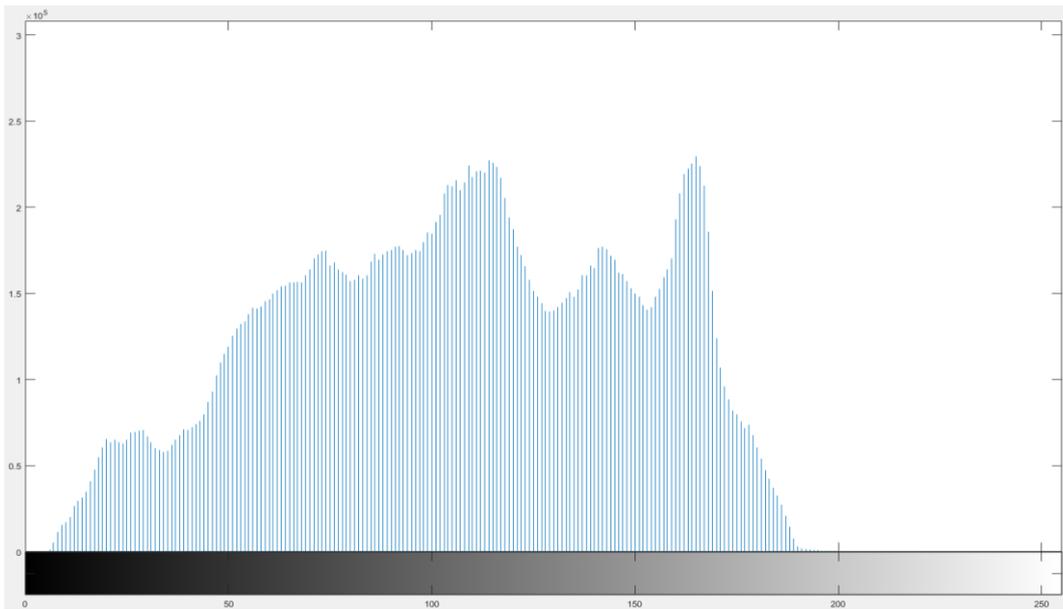
Figure 3.5 Histogram of the photo 3.2
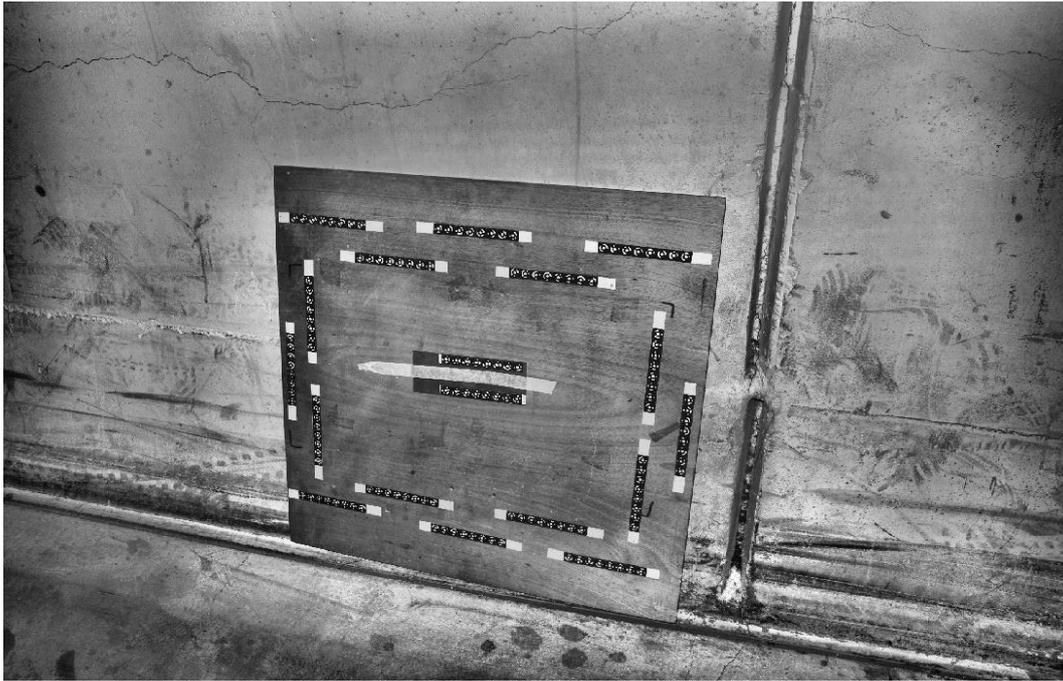
Photo 3.3 Implementation of adaptive histogram equalization
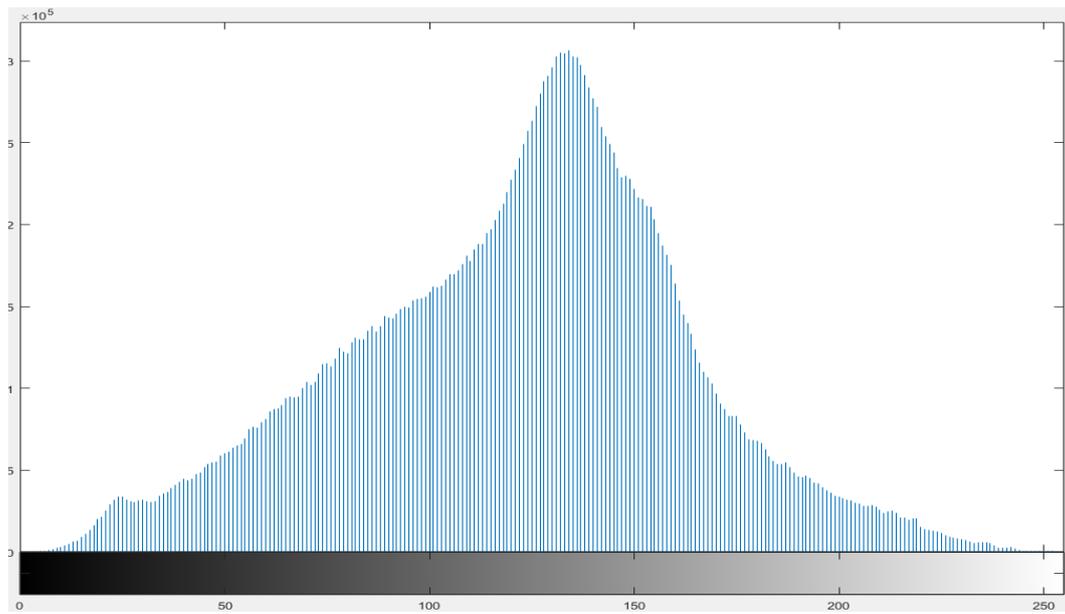
Figure 3.6 Histogram of the photo 3.3
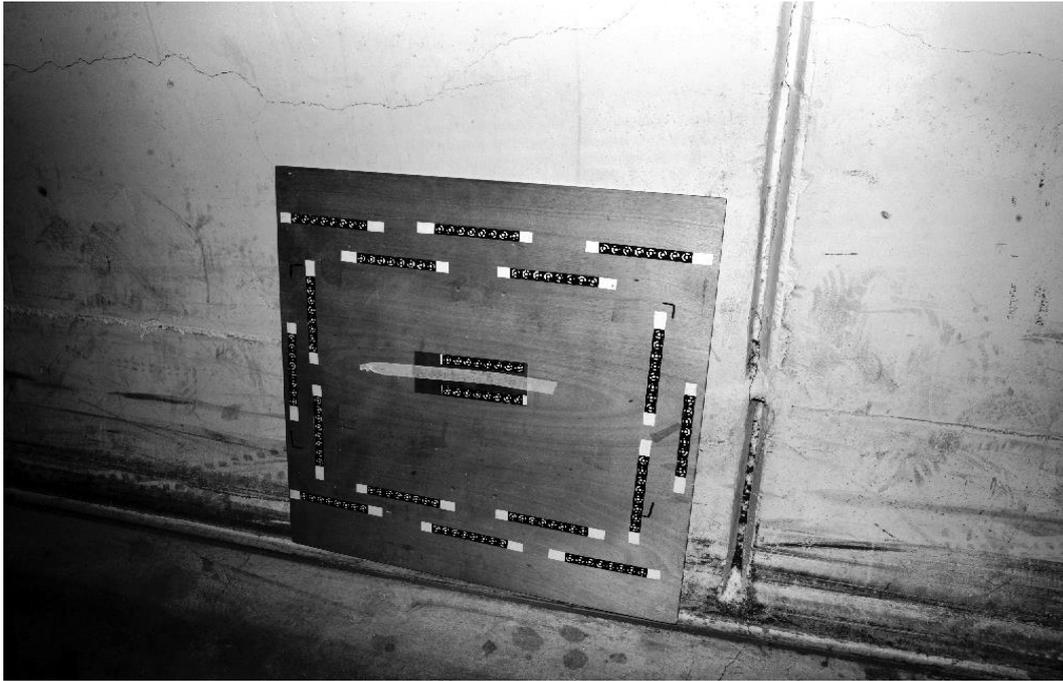
Photo 3.4 Implementation of global histogram equalization
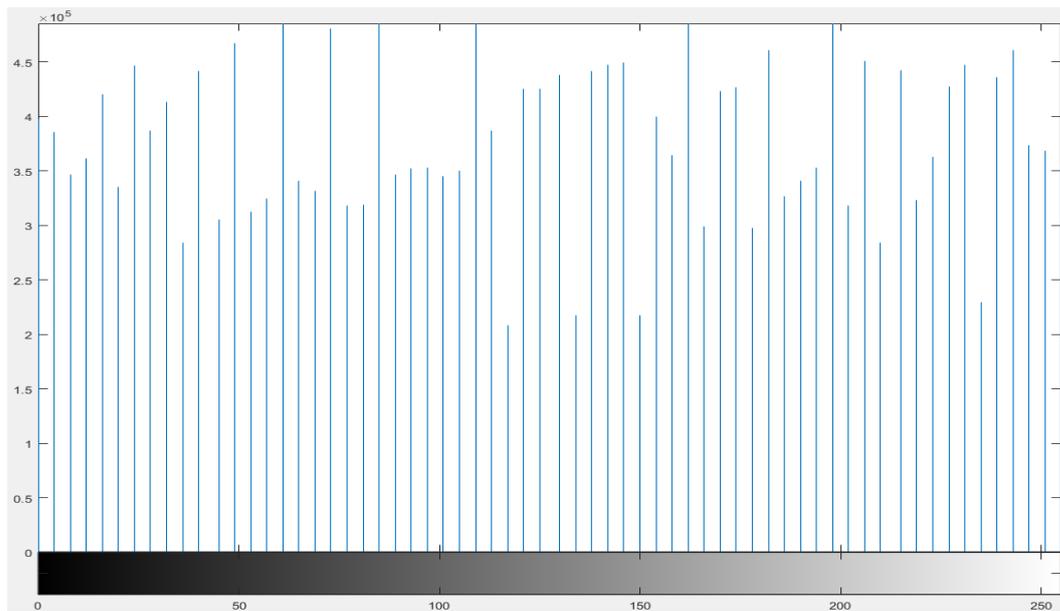
Figure 3.7 Histogram of the photo 3.4

3.3.3.2. Guided filter

After the implementation of the adaptive histogram equalization on an image, a lot of texture appears that previously was not visible. This texture in some cases might work as a noise, which may delay the

processing time of the algorithm. Considering that, a filter which is able to smooth the image should be applied.

An important advantage of the guided filter is that it is an edge preserving filter also, thus the geometry of the targets after the usage of the filter will not change.

The guided image filtering performs smoothing of an image using the contents of another image picture called "guide". This image guide may be the image itself, a different version of the image or an entirely different image.

The preservation of edges is based on the variance value of the image that is used as a guide. The parameter ε (regularization) is given which is going to be used to as a criterion to consider whether a variance is high or low. Regions that have a variance (σ^2) greater than ε are retained, while areas that have a variance lower than ε are smoothed (Scandella L. 2017).

An example of image filtering with the guided filter is illustrated on the photo 3.5.
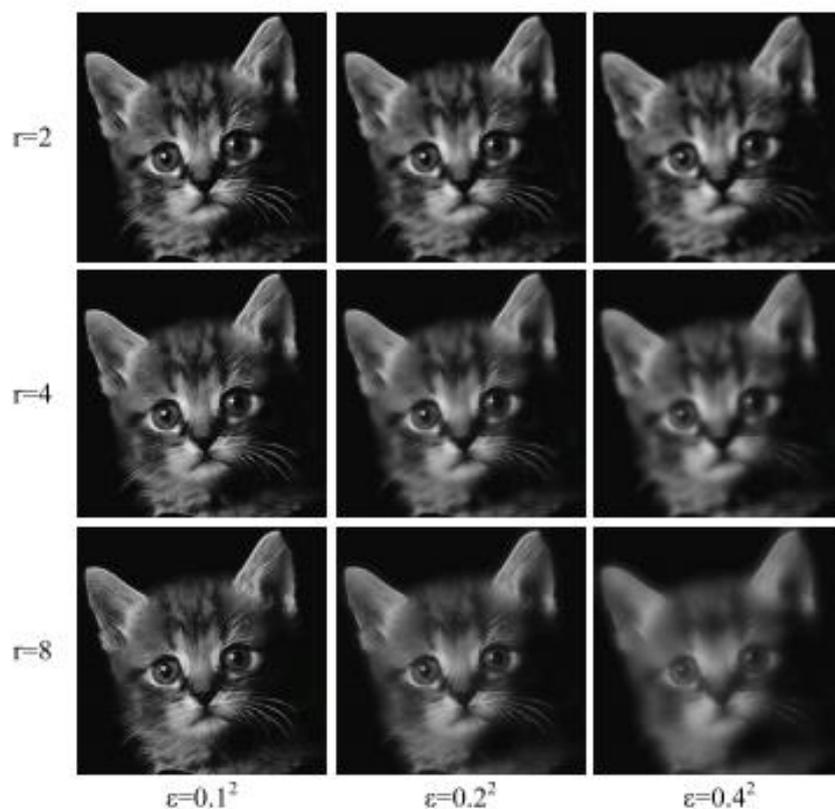
Photo 3.5 Image filtering with guided filter (Scandella L. 2017)

3.3.3.3. Gaussian filter

The Gaussian smoothing operator is a two-dimensional convolution operator that is used to blur images and remove detail and noise. Simple smoothing filters such as the Gaussian filter are able to reduce the noise that exists in an image by filtering and smoothing the high frequencies. However, these filters might remove also intensity variations in an image which might result to the destruction of some structures. Sometimes crucial information has been smoothed; thus this information is lost (Fisher R. 2003).

A multivariate Gaussian form is:

$$G(x, y) = \frac{1}{2\pi\sigma^2} e^{-\frac{x^2+y^2}{2\sigma^2}} \tag{3.1}$$
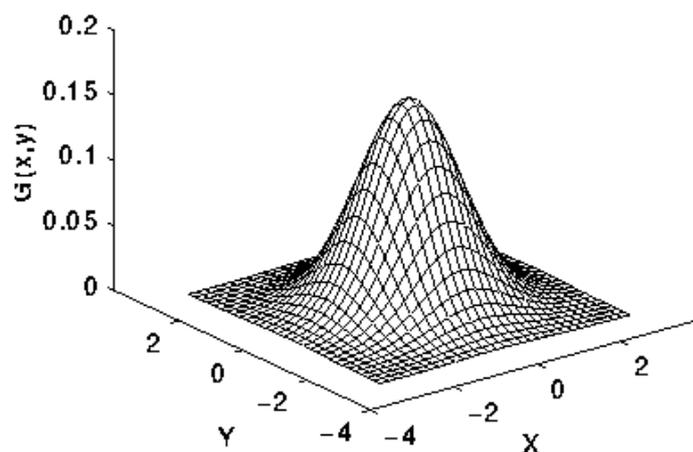
Figure 3.8 Multivariate Gaussian density with mean (0,0) and σ=1
(stackexchange.com)

3.3.3.4. Image sharpening

The third way of image preprocessing, which is recommended for most of the cases, is using an unsharp masking method, which returns an enhanced version of the grayscale or truecolor (RGB) input image, where the image features, such as edges, have been sharpened. Sharpness is apparently the contrast between different colors. A quick transition from black to white looks sharp, however a gradual transition from black to gray and from gray to white looks blurry. Sharpening images increases the contrast along the edges where different colors meet (Mathworks Sharpening 2018). The technique uses a blurred, or "unsharp", image to

create a mask of the original image. The unsharped mask is then combined with the original image, creating an image that is less blurry than the original. Two examples of image sharpening are presented on the photo 3.6 and photo 3.7.
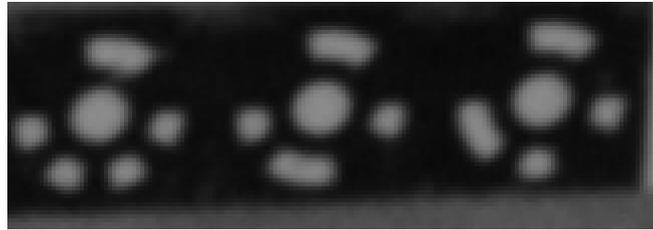
(a)
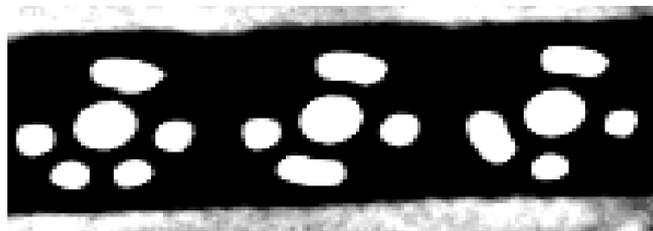
(b)

Photo 3.6 Group of targets before (a) and after (b) image sharpening
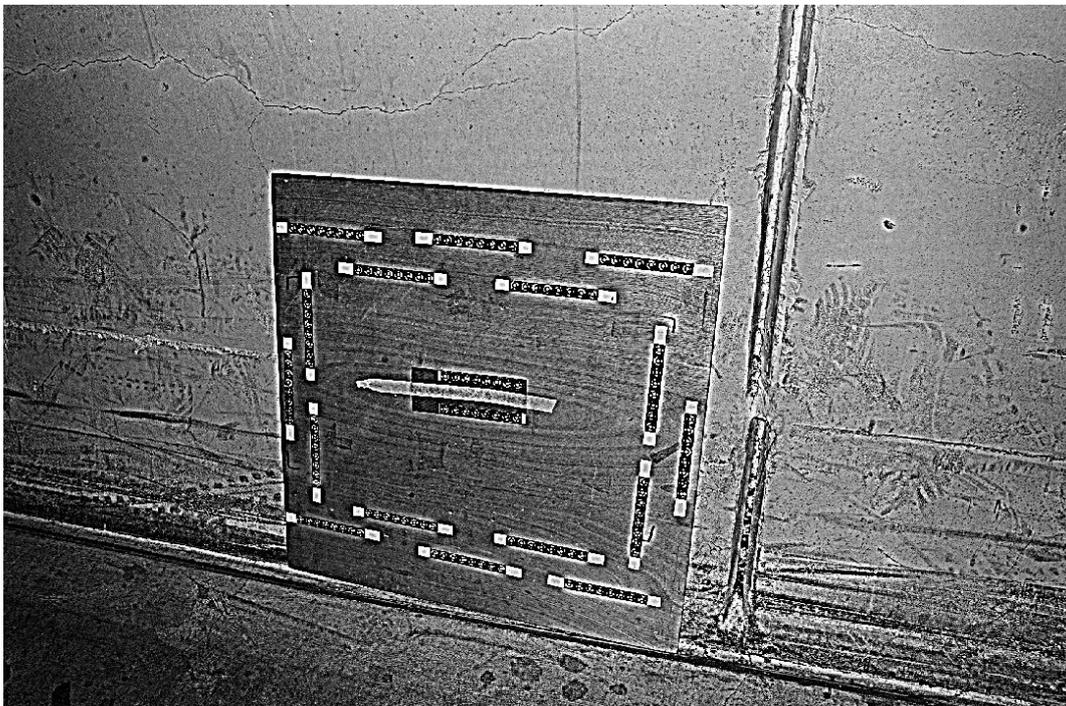
Photo 3.7 Sharpened image

3.3.4. Image binarization

After the preprocessing of the image, a binarization should be applied in order to create a binary image and use it on *regionprops* function for the automatic detection of the targets.

In some cases, where there is sufficient illumination in the environment, Otsu's method has been applied. The algorithm assumes that the image contains two classes of pixels following bimodal histogram so that the pixels either fall in the foreground or background. Then it calculates the optimum threshold separating the two classes so that the sum of the foreground and background spread is minimum (Greensted A. 2010).

Otsu's method exhibits relatively good performance if the histogram approaches a bimodal distribution and possesses a deep and sharp valley between the two peaks. However, if the object area is small compared to the background area, for instance when the object is a target, the histogram no longer exhibits bimodality. If the variances of an object and the background are large with respect to the mean difference, or the image is affected by additive noise, the sharp valley at the histogram is not present anymore, thus an incorrect threshold could be determined by the Otsu's method, resulting to segmentation errors (Chandrakala M. 2016).

Examples of successful implementation of the Otsu's method is presented in photo 3.8 and 3.11, where prior of the execution of the binarization, the images were processed by using the adaptive histogram equalization (Photo 3.10).

In cases where the image is almost entirely dark, for example when retro reflective targets are used, the small objects like these targets are not able to create bimodal histogram (Photo 3.12 & 3.13).

Photo 3.8 Group of targets on binarized image using Otsu's method
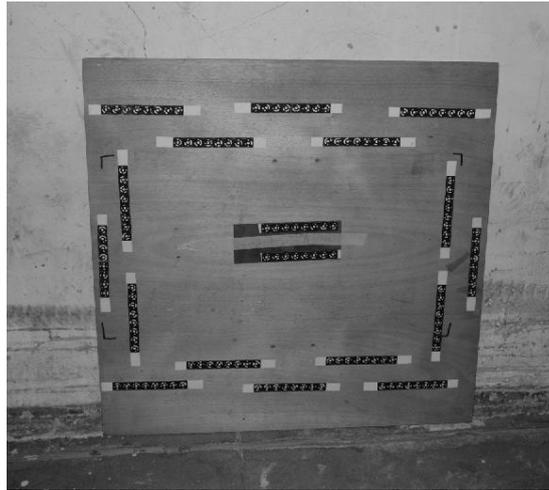
Photo 3.9 Original grayscale image
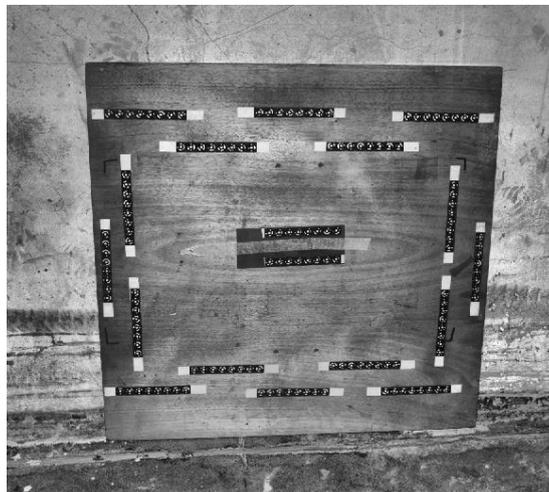
Photo 3.10 Processed image using of adaptive histogram equalization
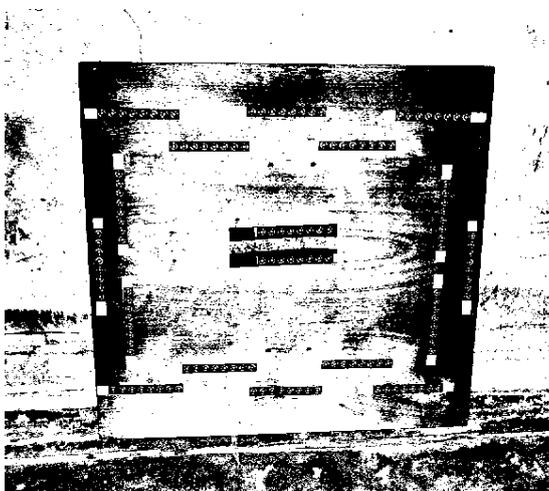
Photo 3.11 Image after the binarization

At these cases, Otsu's method for binarization does not provide sufficient results. Under these circumstances, in order to avoid poor results, the maximum and the minimum value of pixel intensity needs be found. When these values are determined, the following computation will be used in order to find the new threshold value:

$$threshold = (maxValue + minValue) \cdot 40\% \qquad (3.2)$$

For instance, if the maximum value of the intensity of the pixels is 249 and the minimum is 1, then the new threshold will be T=100.

At the photo 3.13 it can be easily seen that Otsu's results are not reliable and the targets in the binary image are destroyed because the threshold value is very low. Hence, the threshold should be calculated by formula (3.2). The new image created from the second binarization presents the targets much clearer than previously and the targets are completely undamaged (Photo 3.14).
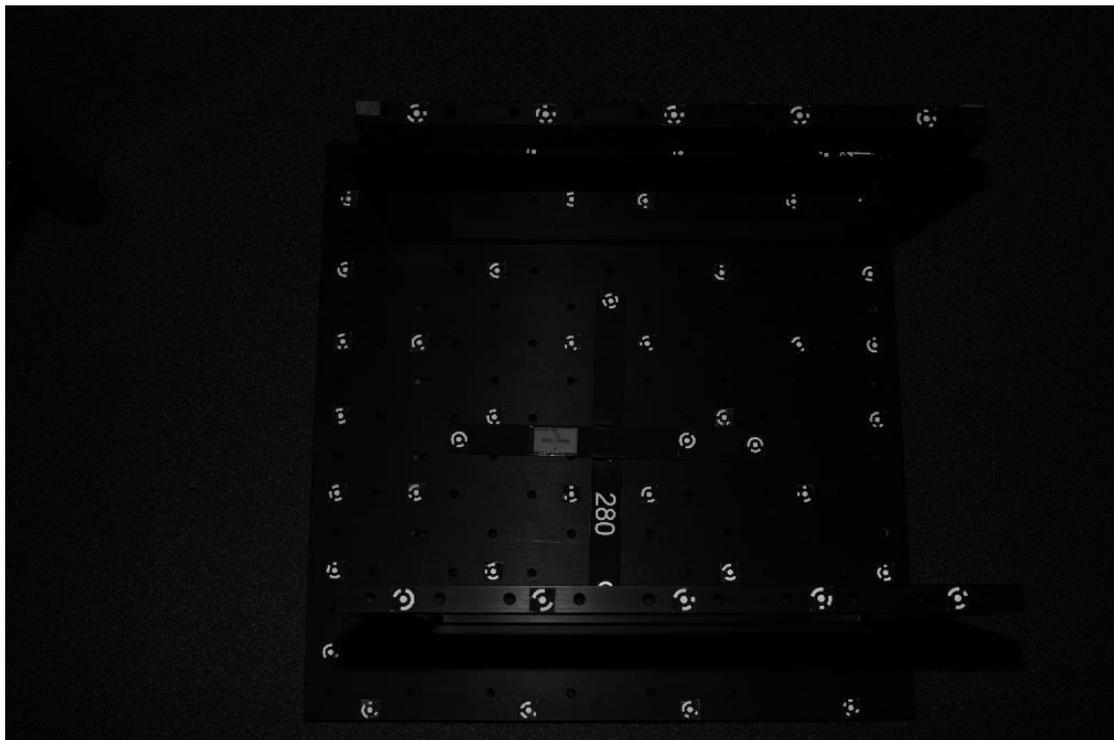
Photo 3.12 Project with retro reflective targets
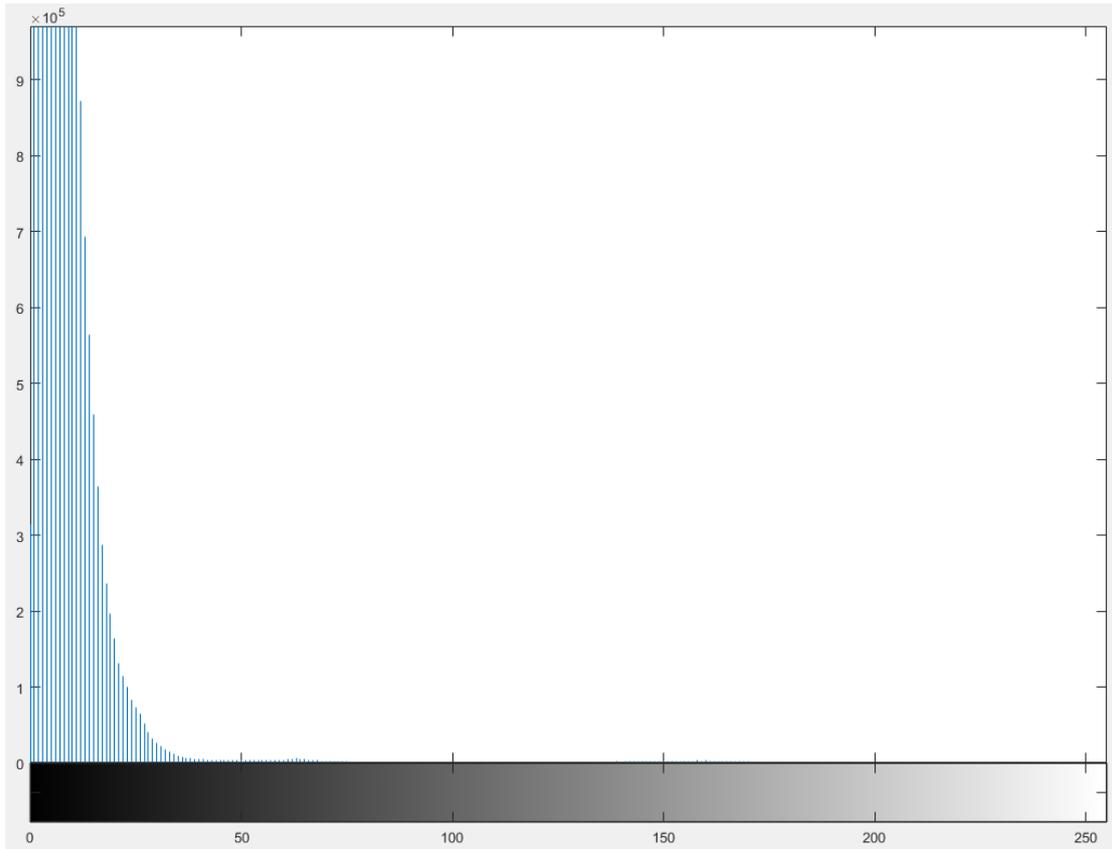
Figure 3.9 Histogram of the project with retro reflective targets
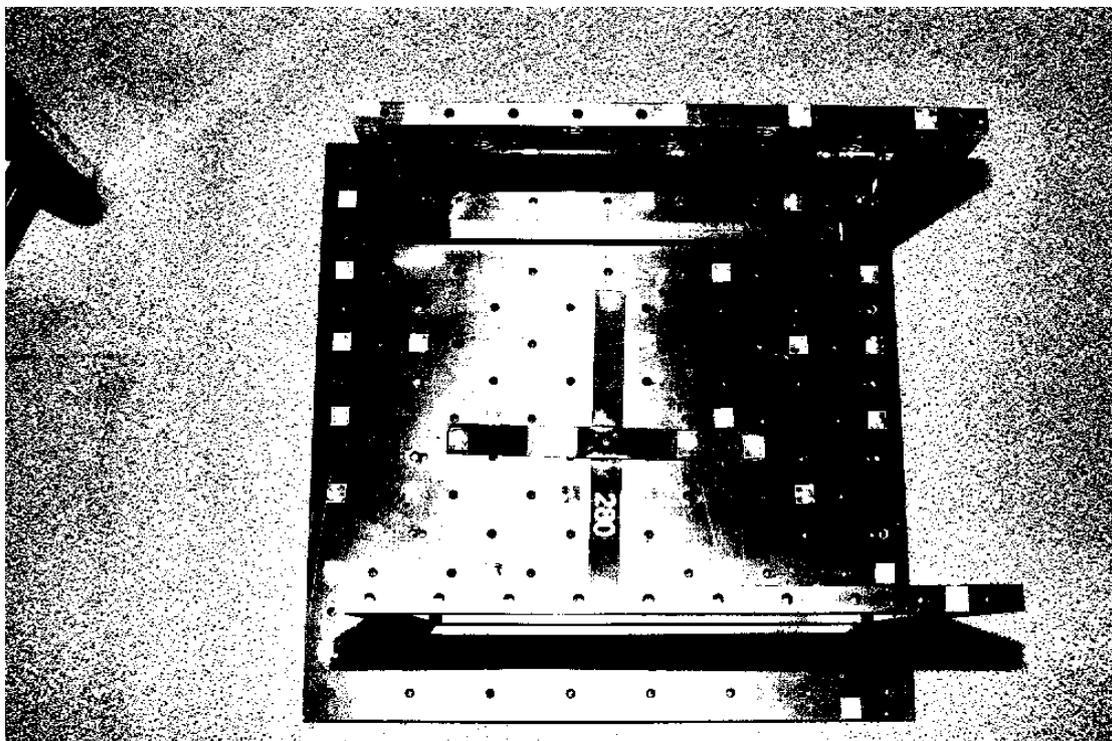
Photo 3.13 Binarization with Otsu's method
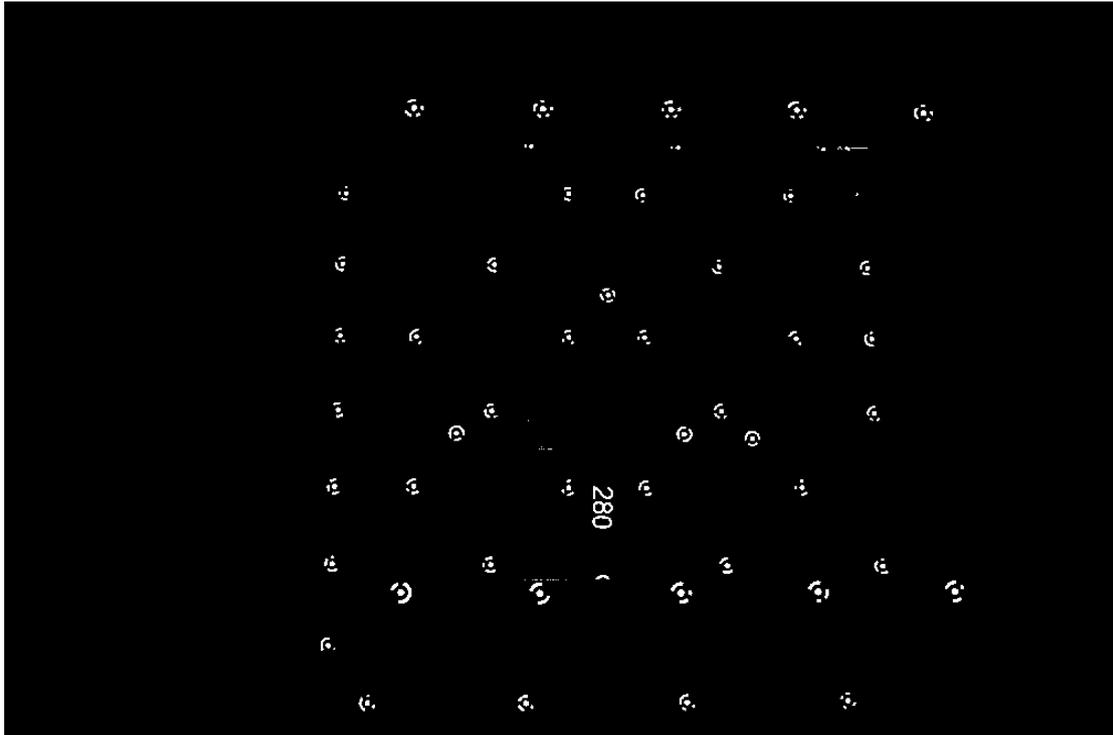
Photo 3.14 Binary image using $(maxValue + minValue) \cdot 40\%$

3.4. Target detection algorithms

During the development of the algorithm for the automatic detection of the photogrammetric targets, a lot of methods had been tested. These methods are the detection of specific features on images and matching between images, circular Hough transformation and analysis of connected objects in a binary image using *regionprops* function. Each of these algorithms has its own advantages and disadvantages. However, the most reliable results out of these three come from the *regionprops* function with the implementation of some conditions. The results are later used for further analysis and development of the algorithm in order to do the measurement and the decoding.

3.4.1. Object detection using point feature matching

This method involves an algorithm for detecting a specific object based on finding point correspondences between the reference and the target image. It is able to detect objects despite a scale change or rotation (Mathworks Feature Matching 2018).

45

This procedure has been one of the first tries during the beginning of the elaboration of the thesis in order to achieve the automatic detection of targets. The principle of this method is the detection of the strongest features on the reference image (Photo 3.15).

The same specific task is going to be applied on a larger image (Photo 3.16).
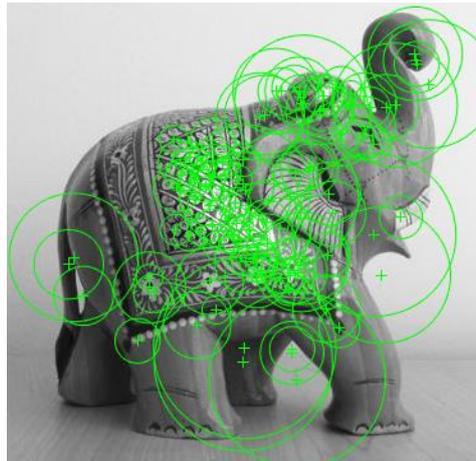
Photo 3.15 Feature detection on the reference image
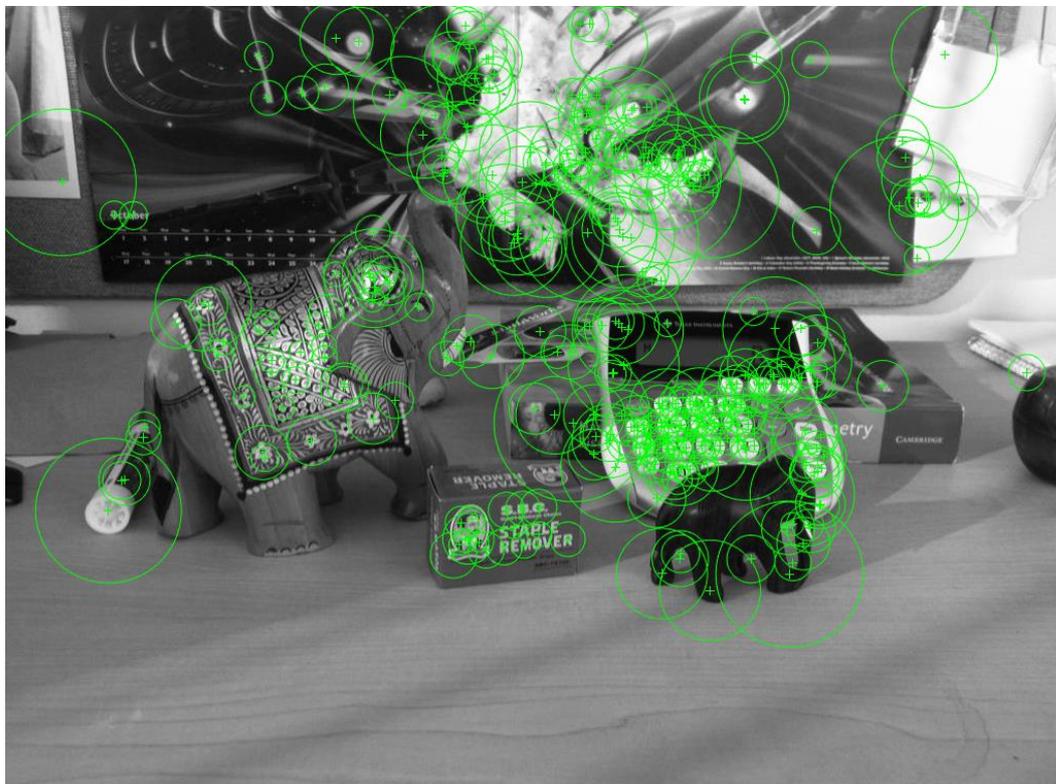
Photo 3.16 Feature detection on target image

On the greater image there is a large number of features which do not match with the features of the reference image. Hence, there should be a matching between the feature points of reference image and the greater image (Photo 3.17).

On this example, a limited number of points were able to be matched. However, the detection has been achieved (Photo 3.18).

The lack of ability to match a great number of corresponding points is the greatest disadvantage of this method. Furthermore, this method is unable to find corresponding points with precision among small targets like the photogrammetric targets, thus the detection is not reliable. Moreover, due to the fact that the photogrammetric targets have a lot of common features, whenever the algorithm was able to make a match, usually it was wrong because the corresponding points were mistakenly chosen as tests revealed.
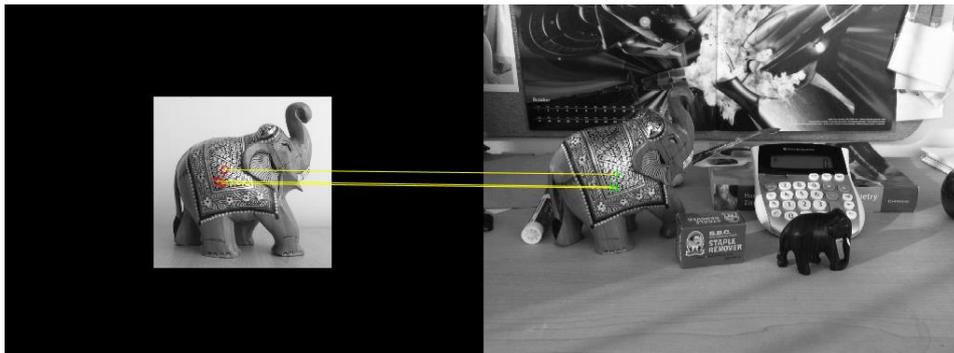
Photo 3.17 Matched points by feature matching
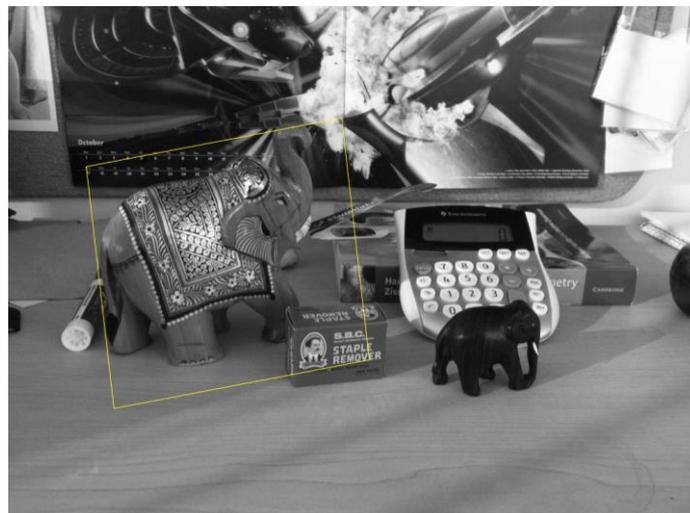
Photo 3.18 Detected target using feature point matching

3.4.2. The use of Hough transformations

The majority of photogrammetric targets commonly used have a circular area in the middle. The center of this area corresponds to the center of the target, which is the aim of the target measurement. Since the shape is a circle, an algorithm, which is able to identify circles, might be really helpful. Such an algorithm is the circle Hough transformation.

The circle Hough Transform (CHT) is a basic technique used in Digital Image Processing, for detecting circular objects in a digital image and is a specialization of the Hough Transform.

3.4.2.1. Linear Hough transformation

The Hough transform can be described as a transformation of a point in a two dimensional region to a parameter space, dependent on the shape of the objects to be identified. The basic functionality of the HT is to detect straight lines. A straight line in the x,y-plane is described by:

$$y = m \cdot x + b \tag{3.3}$$

This line is represented in the Cartesian coordinate system by its parameters b and m where m is the slope and b is the intercept. Due to the fact that perpendicular lines to the x-axis can give unbounded values for parameters m and b (b and m rises to infinity), lines are parameterized in terms of theta θ and r such that:

$$r = x \cdot \cos(\theta) + y \cdot \sin(\theta) \quad for\ \theta \in [0, \pi] \tag{3.4}$$

where r is the distance between the line and the origin, θ is the angle between the x axis and the line r. Thus, given x and y, every line passing through point (x, y) can uniquely be represented by (θ, r) (Fig. 3.10). Both θ and r have finite sizes. The distance r will have the maximum value of two times the diagonal of the image. It is therefore possible to associate a pair (r, θ) with each line on the image. The (r, θ) plane is sometimes referred to as Hough space for the set of straight lines in two dimensions. (Fatoumata D. 2015).

There are infinite number of lines passing through one point (x, y) and the only parameter that varies is the orientation. The representation of the straight lines in the Hough space will result in a sine wave (Fig. 3.11). When multiple points are aligned, the line that connects them can be

found at the parametric space of Hough as an intersection of several sinus curves (Scandella L. 2017).
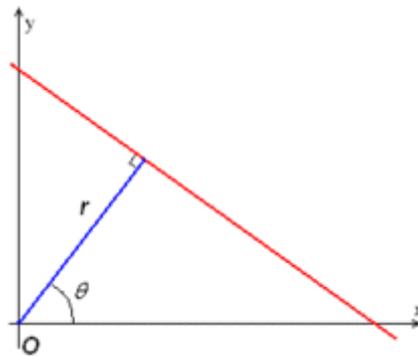
Figure 3.10 Parameterization of a straight line (Fatoumata D. 2015)
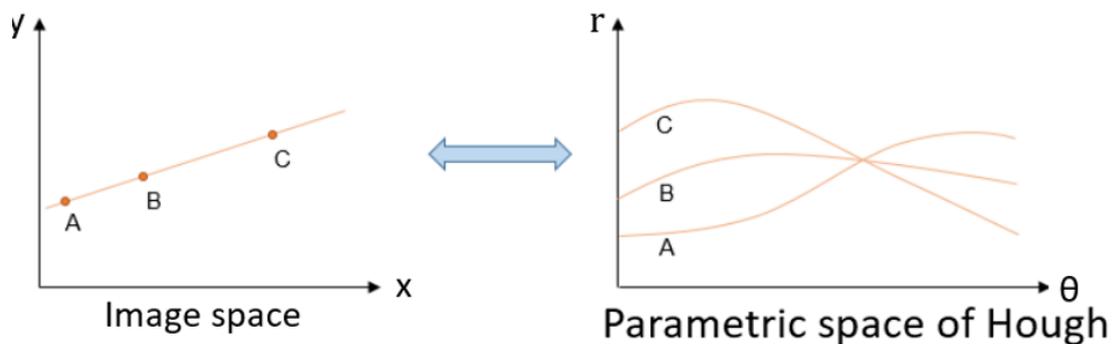
Figure 3.11 Straight line in image and parametric space of Hough
(Scandella L. 2017)

The method of Hough transform uses these properties for detecting sets of pixels lined up in an image, via their representation in the new two-dimensional space.

3.4.2.2. Circular Hough transform

Unlike the linear Hough transform, the circular Hough Transform relies on equations for circles. The equation of the circle is:

$$r^2 = (x - a)^2 + (y - b)^2 \qquad (3.5)$$

Where a and b represent the coordinates for the center, and r is the radius of the circle.

49

In contrast to a linear Hough Transform, a circular Hough transform relies on 3 parameters (a, b, r), which requires a larger computation time and memory for storage, increasing the complexity of extracting information from an image. This is one of the reasons that during the computation on MATLAB interface the amount of time it takes to run the algorithm is a couple of seconds. For simplicity, most circular Hough transformation programs set the radius to a constant value (hard coded) or provide the user with the option of setting a range (maximum and minimum) prior to running the application.

The parametric representation of the circle is:

$$x = a + r \cdot cos(\theta) \tag{3.6}$$

$$y = b + r \cdot sin(\theta) \tag{3.7}$$

Thus, the parameter space for a circle will belong to R^3 (Fig. 3.12) while the line only belonged to R^2. As the number of parameters needed to describe a shape increases, the space R also increases which results to increased complexity of the Hough transform. Therefore, the Hough transform is in general only considered for simple shapes with parameters belonging to R^2 or at most R^3.

The process of finding circles on an image using circular Hough transform is:

First, all edges in the image should be found. For this step any edge detector can be used like Canny or Sobel.
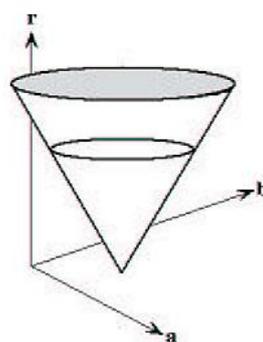
Figure 3.12 Parameter space used for circular Hough transformation
(Pedersen S. 2007)

At each edge points identified, a circle which will have the edge itself as center will be created with the desired radius. This circle is drawn in the parameter space, such that x axis is the 'a' value and the y axis is the 'b'

value while the z axis is the radii. An accumulator can be created which will contain the number of circles passing through individual coordinates. The position which has the highest number corresponds to the center of the circle (Fig. 3.13) (Pedersen S. 2007).
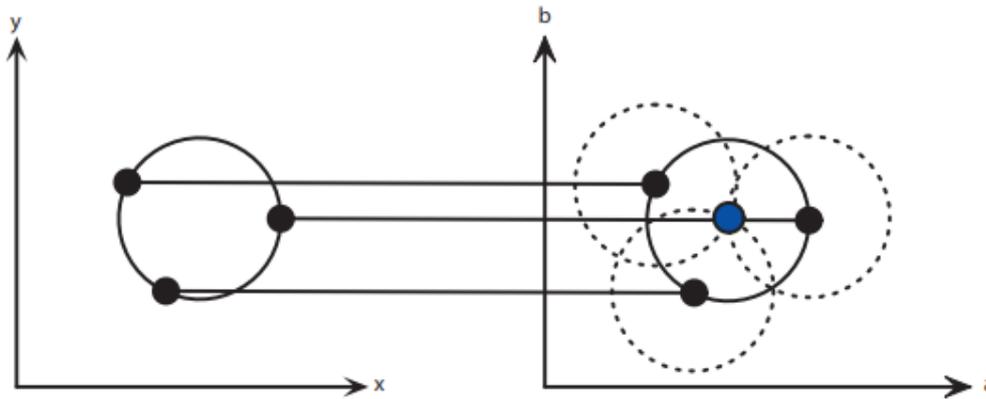
Figure 3.13 Process of finding the center of circle (Pedersen S. 2007)

Having in mind all these, the question is how reliable and precise in each case can circular Hough transform be. As it is known, in order to automate the detection of targets, a hard coded radius cannot be inputted, because depending on the distance and the angle that each picture has been captured, the size of the targets changes.

Furthermore, depending on the angle that each image has been captured, some targets change the geometry that they are projected, thus circles are being transformed to ellipses.

Hence, circular Hough transform is not able to detect and provide reliable results in cases where the angles that images are captured have a high value (Photo 3.19). If the Hough transformation is applied for ellipses the number of parameters increases even more than for the circles and this results to additional calculation time. Finally, the algorithm sometimes depending on the level of sensitivity identifies some "noise" as possible targets, an effect which may be detrimental for further processing. Considering all that, the usage of circular Hough transform for automatic target detection is limited and not sufficient.

Photo 3.19 CHT with radius 20-55 pixels and sensitivity 0.94

In photo 3.20 due to the fact that the perspective projection of the targets is an ellipse the CHT is unable to identify one of the targets. Furthermore, with the radius that is provided the CHT uses the outer side of the targets in order to detect them and not the inner side which is the main object body that should be used for the detection and position determination. Smaller range for radius should be chosen in order to detect the targets using the inner body.
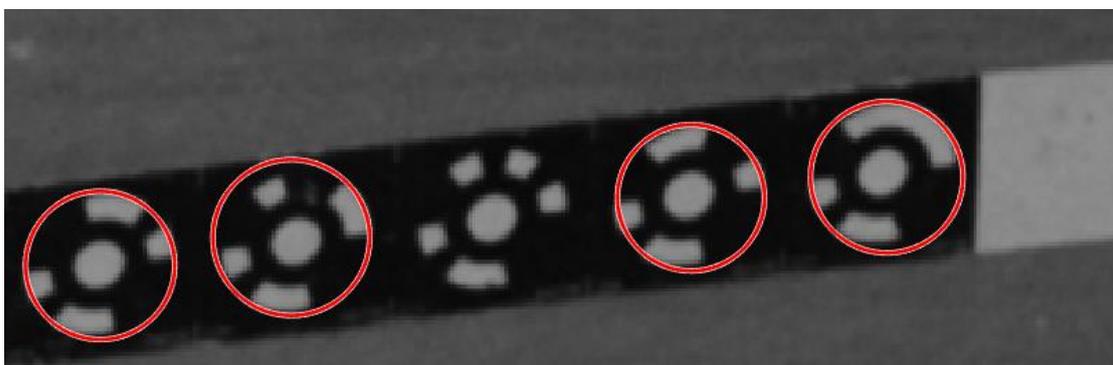
Photo 3.20 CHT unable to find targets that are projected as ellipses

3.4.3. Target detection with analysis of connected objects

The target detection with analysis of connected objects can be achieved by using the function *regionprops* of MATLAB. In order to enhance and make the algorithm for the detection more efficient several conditions should be taken into account. A brief description of the function and a presentation of the conditions follows.

3.4.3.1. Regionprops

The MATLAB function *regionprops* returns measurements for the set of specified properties for each connected component in a binary image.

Regionprops measures a variety of image quantities and features in a black and white image. Specifically, given a black and white image it automatically determines the properties of each contiguous white region that is 8-connected. For instance, one of these particular properties is the coordinates of the centroid or center of mass. Finding the coordinates of the centroid is just one of the properties.

Other useful properties are the area, the perimeter, the major axis length, the minor axis length, the orientation of ellipse and the weighted centroid, which is the center of a region based on location and intensity value.

The first element of weighted centroid is the horizontal coordinate (or x-coordinate) of the weighted centroid. The second element is the vertical coordinate (or y-coordinate) (Regionprops Matlab 2018).

All properties that have been mentioned provide valuable information, which can be used in order to sort out and exclude objects that do not have an elliptical geometry, which the targets have.

A further advantage of the *regionprops* is that it is able to provide approximate coordinates for the center of each targets. This has a significant importance for the ellipse fitting which requires least squares adjustment.

3.4.3.2. Modes of operation and conditions

After gathering all the available data for the objects which have been found, entities that are not photogrammetric targets can be sorted out and excluded. The conditions that are used in order to do that are very simple and reliable.

The geometric shape of the targets when they are projected on an image, as it has been mentioned previously is an ellipse.

An ellipse is a curve in a plane, such that the sum of the distances to the two focal points (F1 and F2) is constant for every point on the curve (Fig. 3.16), usually denoted as 2a where a>0 and higher than the distance between the two focal points. A parameter that defines the shape of an ellipse is the eccentricity, which ranges between 0 and less than 1. For eccentricity equal to 1 the ellipse is a circle. Ellipses have eccentricity higher than 0 and lower than 1 (Adamopoulos L. 2018).

Ellipses can be produced by conic sections (Fig. 3.14).

The general equation for a conic section is:

$$Ax^2 + Bxy + Cy^2 + Dx + Ey + F = 0 \qquad (3.8)$$

The equation of an ellipse whose center is at (0, 0) and has a rotation angle of 0 degrees is:

$$\frac{x^2}{a^2} + \frac{y^2}{b^2} = 1 \qquad (3.9)$$
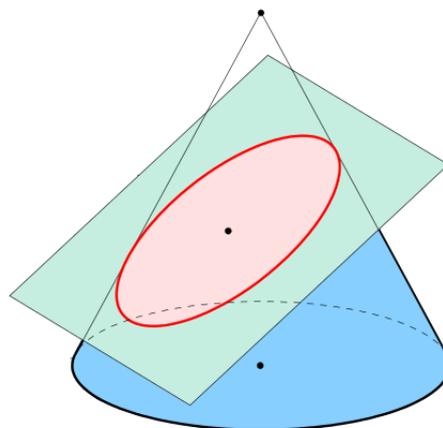
Figure 3.14 Intersection of a cone with an inclined plane
(en.wikipedia.org/wiki/Ellipse)

54

The coordinates of the focal points are F1 = $(c, 0)$ and F2 = $(-c, 0)$ where c is equal to:

$$c = \sqrt{a^2 - b^2} \qquad\qquad (3.10)$$

One of the most important properties of an ellipse for the tests that have been carried out is the area. The area of an ellipse is:

$$A = \pi ab \qquad\qquad (3.11)$$
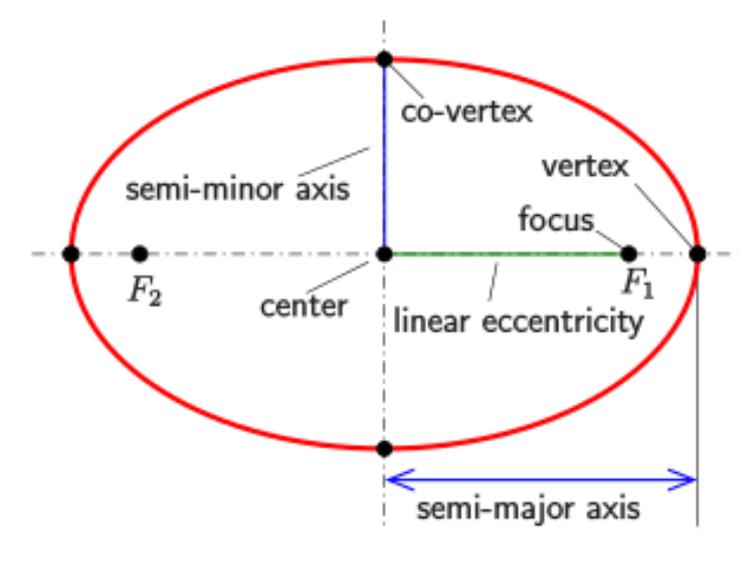
Figure 3.15 Ellipse with its elements (en.wikipedia.org/wiki/Ellipse)
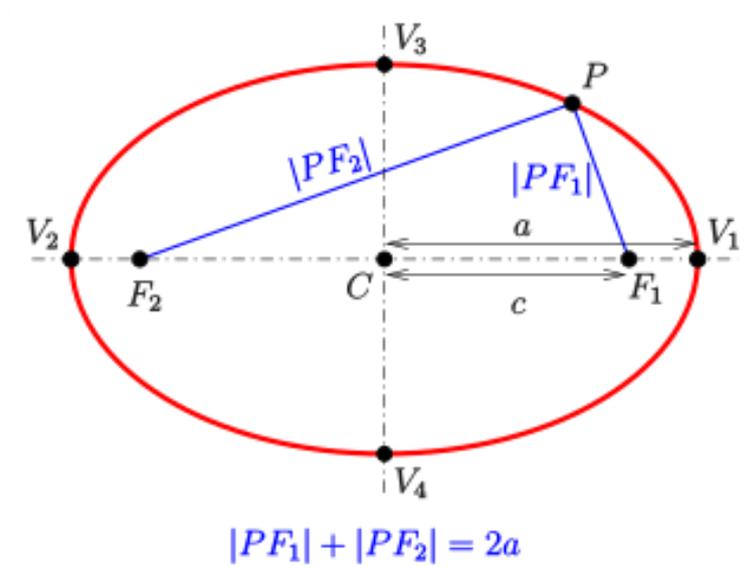
Figure 3.16 Definition of an ellipse (en.wikipedia.org/wiki/Ellipse)

Where a and b are the lengths of the semi-major and semi-minor axes (Fig. 3.15), respectively. The *regionprops* function is able to provide to the user the properties a, b and the area for each object that has been identified. This is very helpful, because in this way the user is able to use the formula of the area of an ellipse.

Hence, the observed area from *regionprops* and the calculated area from the user are available. In this way, a comparison between the values of these areas can be done.

The objects that are truly ellipses fulfill the condition that these two areas should be nearly equal. Thus, the objects that do not fulfill this condition are excluded from the list of targets because the observed area by *regionsprops* and the calculated area from the formula are not equal.

The ratio of the observed area to the calculated should be equal to 1 if the object is an ellipse. Of course, these two areas cannot be exactly equal because an image might have some distortions and each pixel has a pixel size of some microns and the measurement of the area is carried out on a binarized image that has steps of 1 pixel.

Hence, in order to keep an object in the list of the possible targets, the ratio of the observed area from *regionprops* to the calculated area should be in a range. This range is different each time and it depends by the minimum target size. In principle the larger a target is, the more probable it is for the ratio to be closer to a value equal to one.

On the following graph (Fig. 3.17), there are some targets of different sizes and through them it is visible how the size of a target (area) can be related with the range that is required in order to do the detection of the targets.

$$\frac{A_{regionprops}}{A_{calculated}} = 1 \pm range \tag{3.12}$$

This condition is very important for the development of the algorithm because it helps to exclude points, which are not targets. Thus, it increases the speed of algorithm and its reliability.

It is essential to mention that the higher the value of ranges, the more probable is to include as possible targets, points that are not targets. By applying higher range values, the condition is more flexible and small spots which have similar geometry with targets are considered as well as targets, which is an occurrence that may be adverse for further processing.

In order to avoid the selection of some objects, which may have elliptical shapes, but are not targets and to exclude damaged targets and generally unwanted data, a second condition has been set.

The second condition is also a ratio. This time ellipses that have a ratio 'a to b' higher than a specific value are excluded as targets. This increases the reliability of detection because unwanted objects are being removed in this way. The ratio can be defined by the user, however the recommended value is 3 (equation 3.13).

An example of successful target detection is presented on the photo 3.21 where the targets have been attached on the LHC.
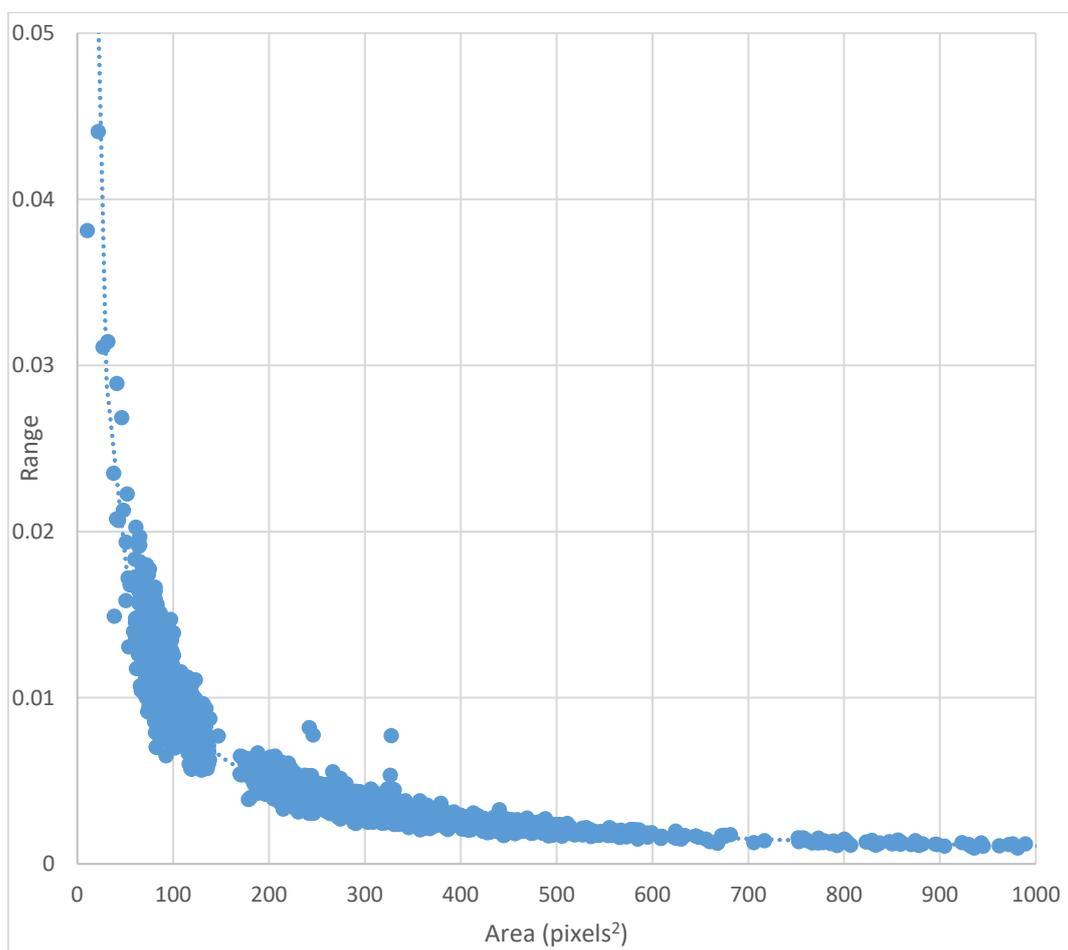
Figure 3.17 Graph for determination of the range value

Depending on the type of target and the minimum target size, a value for the range can be selected from the table 3.1. Targets whose diameter is below 3 pixels, cannot be detected with reliability. For this reason, range values exist for targets that have at least a diameter of 3 pixels.

Type of target	Minimum target size - Diameter (pixels)	Area (pixels^2)	Range
Retro reflective	$3 \leq D < 5$	$7 \leq A < 20$	0.05
	$5 \leq D < 7$	$20 \leq A < 40$	0.03
	$7 \leq D < 10$	$40 \leq A < 80$	0.02
	$10 \leq D$	$80 \leq A$	0.01
Conventional	$3 \leq D < 5$	$7 \leq A < 20$	0.03
	$5 \leq D < 7$	$20 \leq A < 40$	0.025
	$7 \leq D < 10$	$40 \leq A < 80$	0.02
	$10 \leq D$	$80 \leq A$	0.01

Table 3.1 Proposed range with respect to minimum target size

$$\frac{a}{b} < 3 \tag{3.13}$$

As the value of the range gets higher, there is a higher risk that some code segments around the circular area of the real target might be considered also as targets (Photo 3.22).

In order to avoid this, two additional conditions have been introduced.

The first one is:

- if the distance between two possible target centers is less than 3 times the half of the major axis of the object that is tested and
- if the difference of the area between the larger object and the smaller object is higher than 25% the area of the larger object
- then the larger object is the considered as the real target and the smaller object is excluded from the list.

The second one is:

- if the distance between two possible targets' centers is less than 3 times the half major axis
- the difference of area between the larger object and the smaller object is smaller than 30% the area of the larger object and
- if the ratio $\frac{a}{b}$ of the one object is smaller than the ratio $\frac{a}{b}$ of the other object
- then the real target is the one that has the smallest ratio.

This condition has been introduced, due to the fact that two code segments united might have a larger area than the circular region, however their ratio $\frac{a}{b}$ is also larger than the circular region which has a ratio closer to the value 1. Thus, the circular region which is the target itself will be kept as the real target.

58
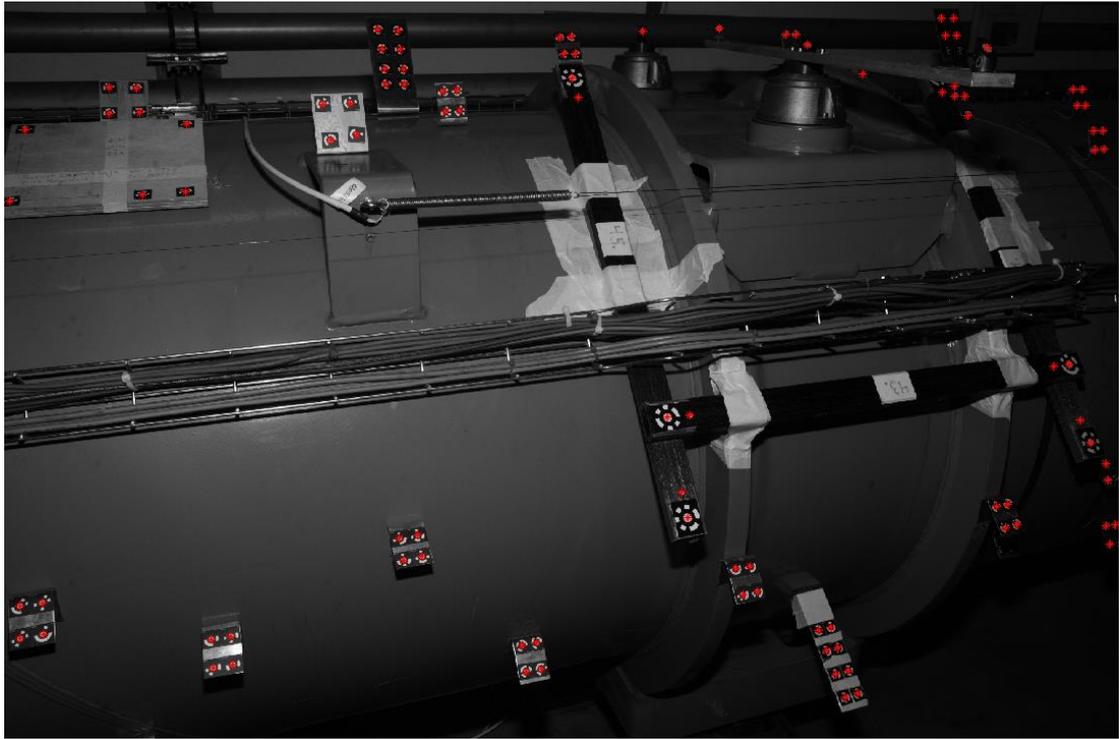
Photo 3.21 Detection of the targets at the LHC
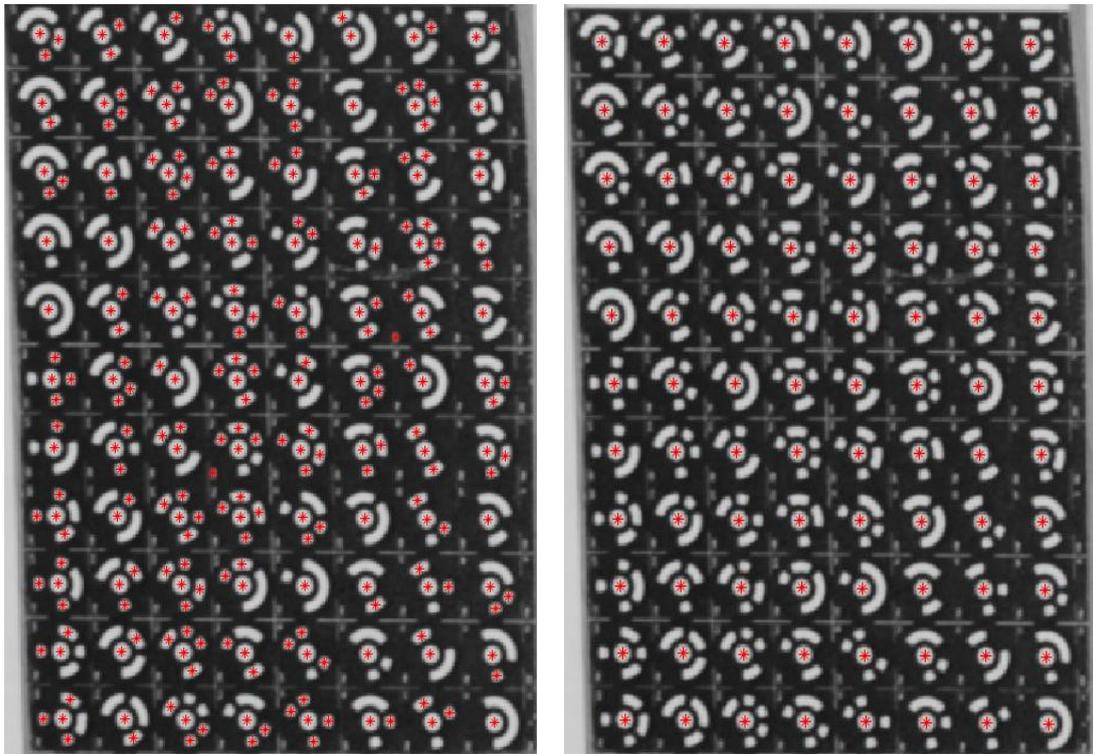
Photo 3.22 Exclusion of code segments as possible targets

In some cases, the algorithm is not able to detect some targets because they might be partially damaged or have some dust which changes the geometry of the targets, thus their shape on the binarized image is not an ellipse and their detection is not possible (Photo 3.23 & Photo 3.23). However, sometimes these undetected targets are detected on other images.
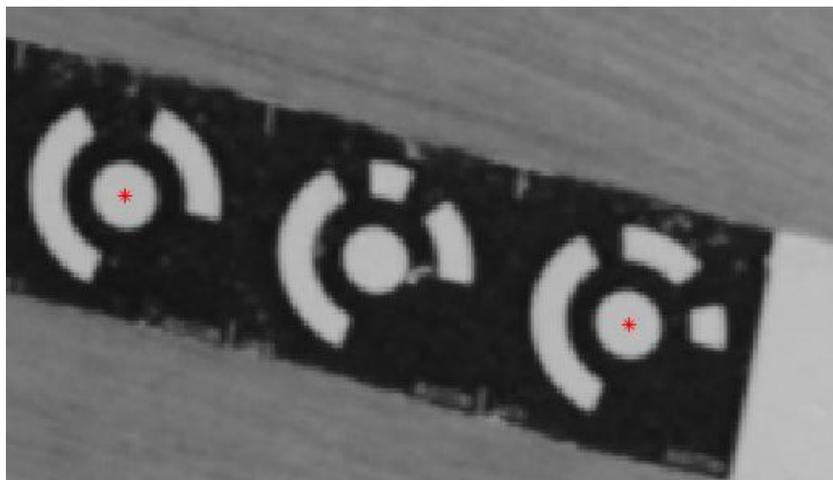
Photo 3.23 Undetected damaged target
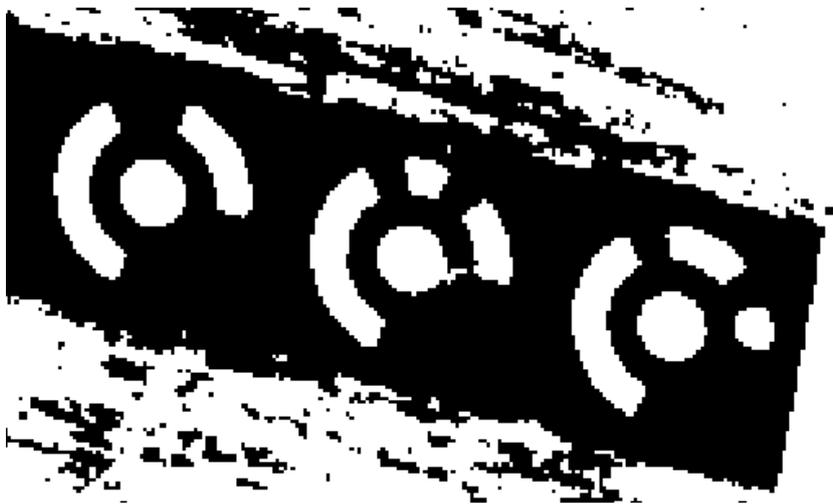
Photo 3.24 Binarization of an image with a damaged target

3.5. Evaluation of the automatic detection algorithm

So far, three possible algorithms have been proposed for the automatic detection of targets. The most reliable of them is the target detection with

analysis of connected objects using the *regionprops* function of MATLAB.

The reliability of this algorithm is higher than the other two. Furthermore, many valuable properties of the ellipses can be extracted by using the aforementioned function. Such properties are the weighted centroid, the half major and half minor axes of the ellipses and the orientation. The values of these properties are going to be used as initial approximate values for the ellipse adjustment using least squares.

AICON is used at CERN as one of the main photogrammetric software, which provides highly reliable results. Thus, AICON results will be used as reference in order to evaluate the outcomes of the detection algorithm that has been developed.

The figures 3.19 and 3.20, present the results of the target detection by AICON and the developed algorithm on a project, which took place at the LHC (Photo 3.25).

The camera that has been used is the Nikon D3X with 28mm AICON Metric Lens, ISO 320, Flash 1/8 with diffusion plate on and large flash angle, Aperture 11, Exposure time 1/125 and focus 1.25m.
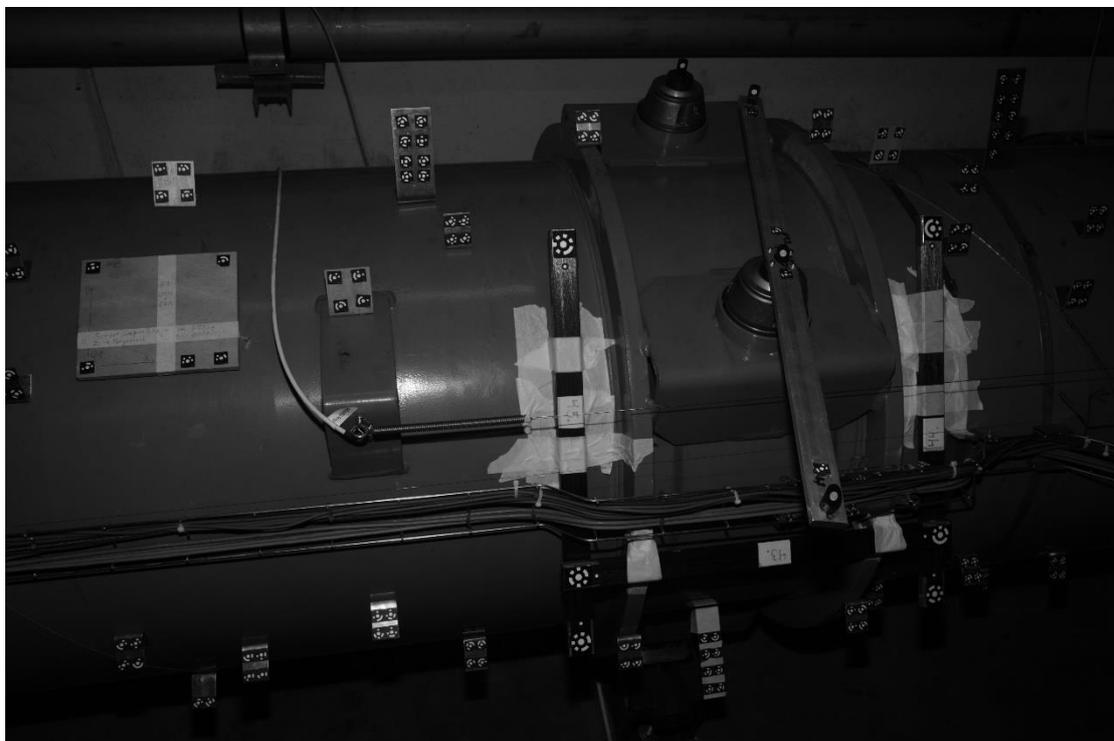
Photo 3.25 Photogrammetric project at the LHC
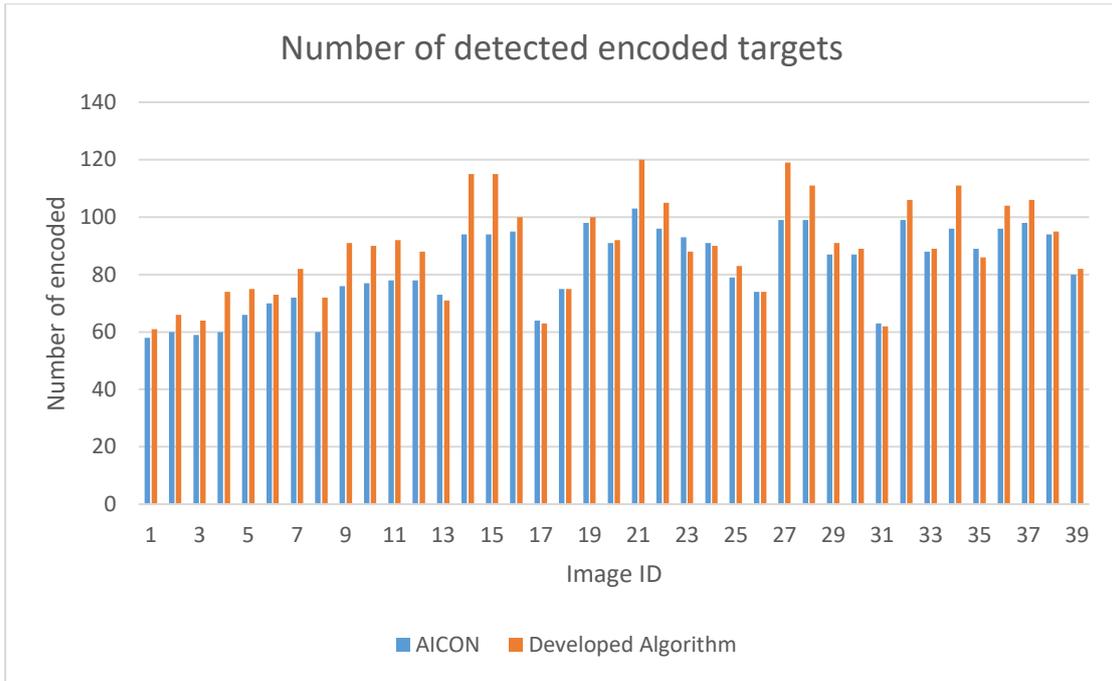
Figure 3.18 Detected encoded targets by using AICON and the developed algorithm
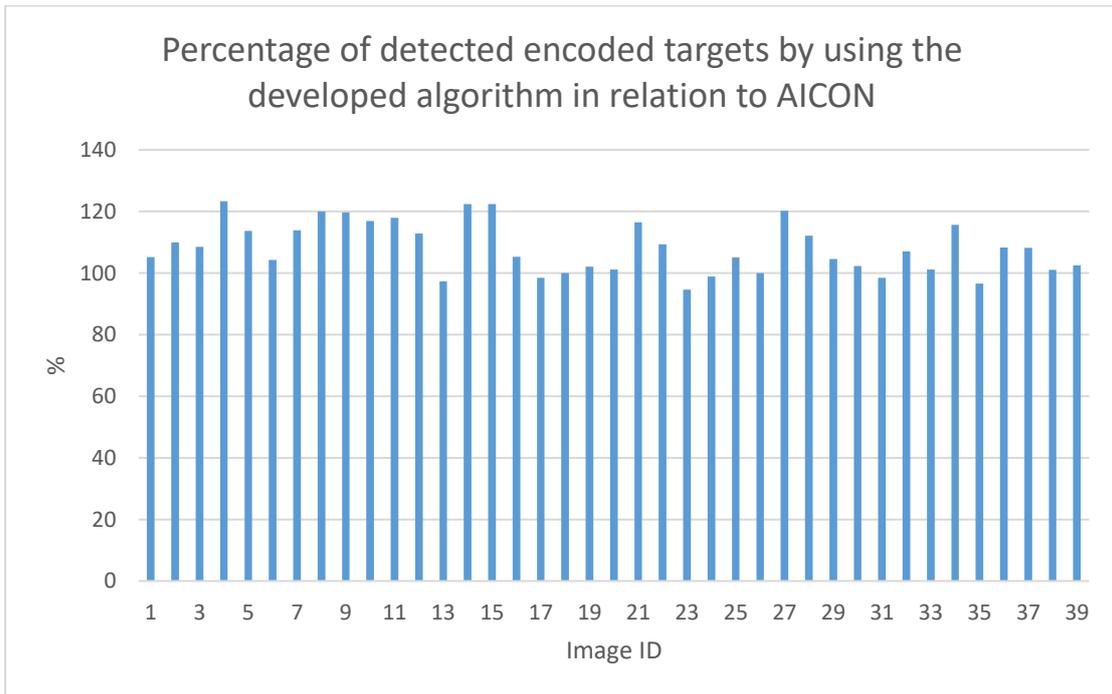
Figure 3.19 Percentage of detected encoded targets by using the developed algorithm in relation to AICON

It is presented in figures 3.19 and 3.20, that the number of detected encoded targets is at the same level as the AICON and some times the number of detected encoded targets is even bigger. This is a very important factor, due to the fact that the number of observations that are going to be used is adequate to have an accurate determination for the interior orientation and also that the risk of neglecting some points and information is lower.

The same analysis is carried out for seven projects with various specifications in order to check the reliability of the developed algorithm and the limits that it can reach.

Projects 1, 2, 3, 6 and 7 have been taken using the D3X camera, however the projects 4 and 5 use different cameras. Furthermore, projects 3 and 5 use retro reflective targets while the rest are conventional targets.

Especially at project 5, targets are relatively small compared to the other projects.

Table 3.3, presents the total number of detected targets by AICON and the developed algorithm on the aforementioned projects, while the figure 3.20 presents the percentage of detected number of targets by the developed algorithm in relation to the number of targets detected by AICON. It is clear, that the number of recognized targets by the developed algorithm and AICON is nearly equal. This fact proves the reliability of the algorithm for the detection of targets.

However, there are some limitations in the ability of the automatic detection. These limits depend on the size and the type of target. If the target is conventionally encoded, then the detection ability abates when they have diameter below 5-6 pixels. This is due to the fact that the code segments are very close to the circular objects which are the targets themselves and they influence their binarization. For the uncoded conventional targets detection ability declines below 4 pixels diameter. Retro reflective encoded targets are hardly detectable for diameters below 5 pixels and also the uncoded retro reflective targets can not be detected with convenience when their diameter is below 4-5 pixels.
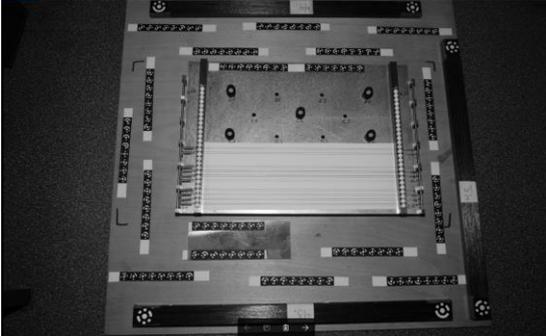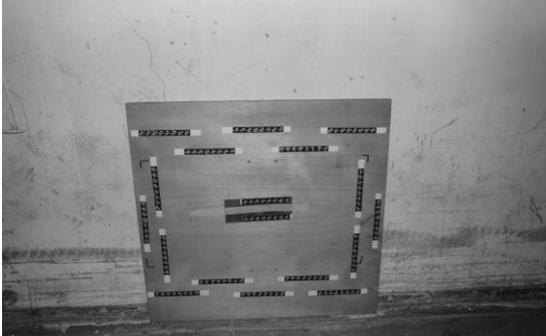
Project 1	Project 2
Project 3	**Project 4**
Project 5	**Project 6**
Project 7	
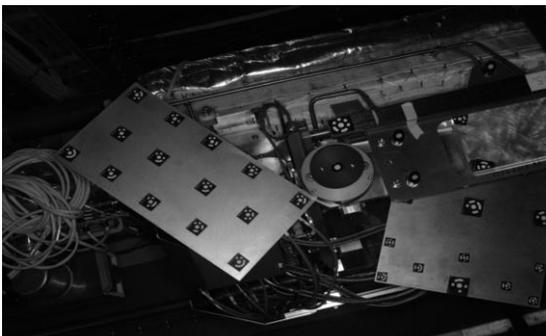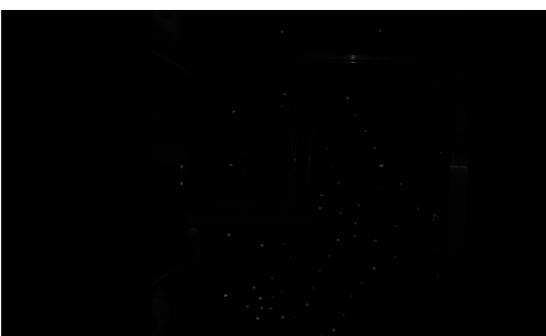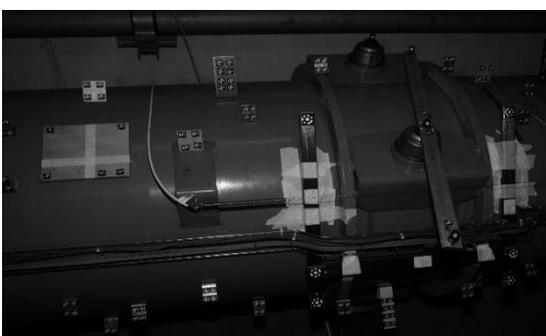
Table 3.2 Photogrammetric test projects
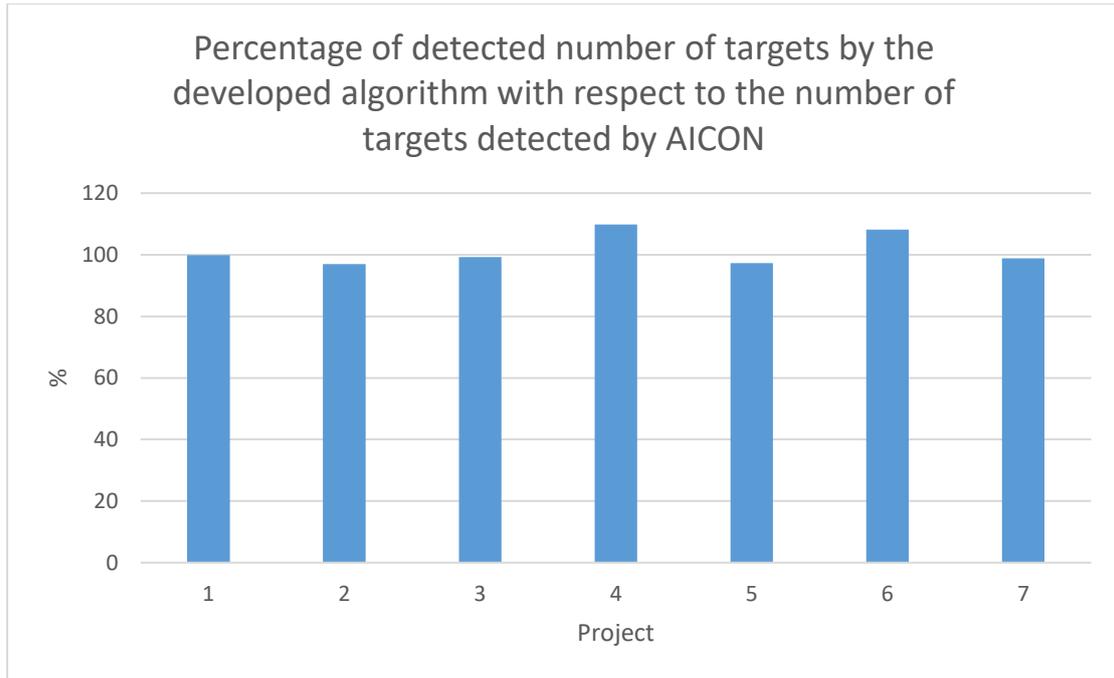
Figure 3.20 Percentage of detected number of targets by the developed algorithm with respect to the number of targets detected by AICON

Project	AICON	Developed Algorithm
1	3733	3727
2	2146	2080
3	1332	1322
4	623	684
5	1537	1496
6	3209	3470
7	2791	2759

Table 3.3 Total number of detected targets by AICON and developed algorithm on each project

Chapter 4

DETERMINATION OF TARGET POSITION

4.1. Target measurement algorithms

After the detection of the targets, a number of ellipses' properties are available to the user such as the coordinates of the ellipses' centers, the half-major and half-minor axis and the orientation of the ellipses. These properties are valuable, for the part of the target position determination.

Since, the approximate position of the targets is already determined, there should be a focus on each specific target in order to achieve the highest possible precision. Thus, each target, is cropped out of the image and a number of algorithms run on these newly cropped images so that the measurement can be implemented precisely.

There are several algorithms that have been tested in order to determine the position of the targets. These are:

- the local *regionprops* providing results with weighted centroid
- local *regionprops* with image resizing providing results with weighted centroid
- ellipse fitting

4.1.1. Image cropping

The approximate position for the center of each target is already determined, as well as the half-major and half-minor axis. With this information a unique rectangle at each target for the image cropping can be generated.

In order to define a rectangle for the cropping, 4 elements should be defined. These are the x_{min}, y_{min}, width and height.

For an ellipse which has an orientation angle smaller than 45° and bigger than 135° the x_{min}, y_{min} are defined as:

$$x_{min} = Cx - a - 2.5a = Cx - 3.5a \qquad (4.1)$$

$$y_{min} = Cy - b - 2.5b = Cy - 3.5b \qquad (4.2)$$

$$x_{max} = Cx + a + 2.5a = Cx + 3.5a \qquad (4.3)$$

$$y_{max} = Cy + b + 2.5b = Cy + 3.5b \qquad (4.4)$$

Where:

Cx : The x-coordinate of the center of the target

Cy : The y-coordinate of the center of the target

a : The half major axis of the ellipse

b : The half minor axis of the ellipse

The coefficient value 2.5 is defined so that the rectangle will include the entire target and its binary code inside, since with the coefficient equal to 2, the cropping rectangle would reach exactly up to the code segments. Thus, the dimension of the cropped image is calculated as 3.5 times the half axis lengths to include the entire binary code of the targets.

For an ellipse which has an orientation angle between 45° and 135° the x_{min}, y_{min} are defined as:

$$x_{min} = Cx - b - 2.5b = Cx - 3.5b \qquad (4.5)$$

$$y_{min} = Cy - a - 2.5a = Cy - 3.5a \qquad (4.6)$$

$$x_{max} = Cx + b + 2.5b = Cx + 3.5b \qquad (4.7)$$

$$y_{max} = Cy + a + 2.5a = Cy + 3.5a \qquad (4.8)$$

Hence, the width and height are:

$$width = x_{max} - x_{min} \qquad (4.9)$$

$$height = y_{max} - y_{min} \qquad (4.10)$$

Figure 4.1 shows an example for the creation of the rectangle for the cropping where half major axis of the target is equal to 2. Thus, the multiplication of 2 by 3.5 times gives 7. Hence, the distance from the center to the side of the rectangle will be equal to 7.
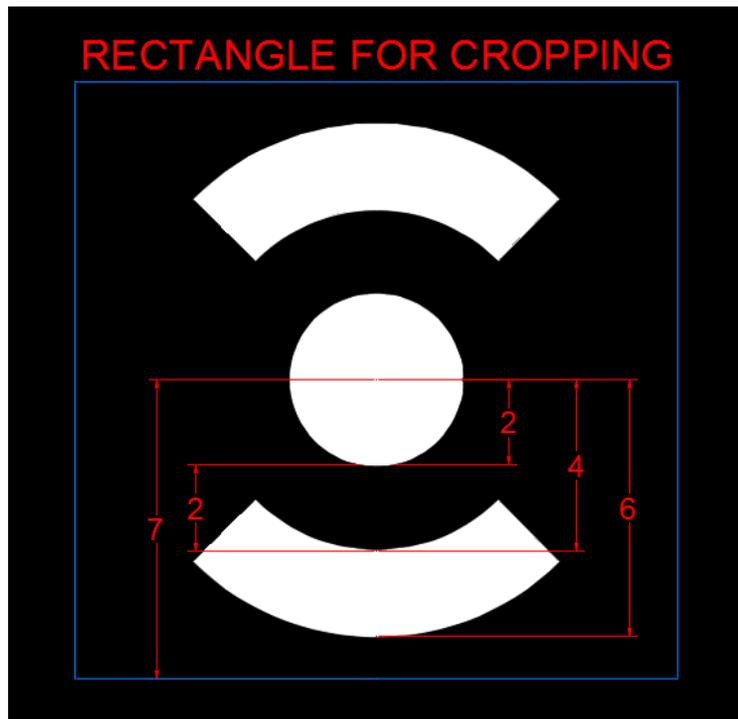
Figure 4.1 Rectangle for target cropping

4.1.2. Local *regionprops* with weighted centroid

The principles in order to do the determination of the position with *regionprops* are more or less the same with the detection algorithm.

The basic idea is to use *regionprops* function on the cropped image in order to find the weighted centroid of the target. The main difference between the usage of *regionprops* in order to achieve the detection and the measurement is the method that the binarization of the image is done.

The binarization of the image, which now is the target itself, is dedicated to it. At the vast majority of the cases, same illumination conditions are present to the whole target and its segments. Keeping this in mind and having available already some approximate values for the image coordinates of the centers of the targets, it is possible to determine a pixel intensity sampling.

Hence, a matrix can be created which will include the intensity pixel values for the center of each target. Because each target has almost the same lighting conditions on its surface the binarization can be applied easily.

69

In order to have a threshold at a level which will not cause problems or delete the code segments of the targets, which are important for the decoding, the threshold value that it is proposed is:

$$threshold = CenterPixValue \cdot 0.55 \qquad (4.11)$$

Of course, instead of 0.55, the value 0.50 can be used, however several tests have revealed that the value 0.55 is very reliable. Every change on the threshold value directly influences the results of the target position since the binarized image that is used on the *regionprops* will be different.

It is important to mention that the cropped images (Photo 4.1) do not need any preprocessing, and the original grayscale images are used, thus the target geometry remains the same and at its original state in order to achieve higher precisions.

4.1.3. Local *regionprops* with image resizing

By the same procedure as in the previous paragraph, *regionprops* is executed once more, however this time on a resized cropped image (Photo 4.2), which is enlarged by a specific scale. In this way, the number of pixels is increased which makes a target more detailed and as it is revealed from the results of the various experiments it seems increase the precision of the measurement. The results from this algorithm are very promising, since the RMS from the bundle adjustment and the σ_0 using the image coordinates from this method, that are produced reveal sufficient precision for photogrammetric works.
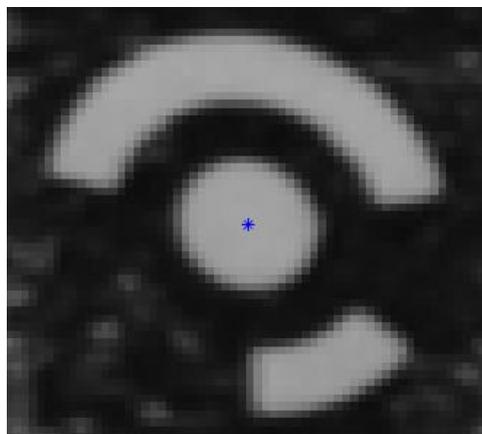
Photo 4.1 Original cropped image
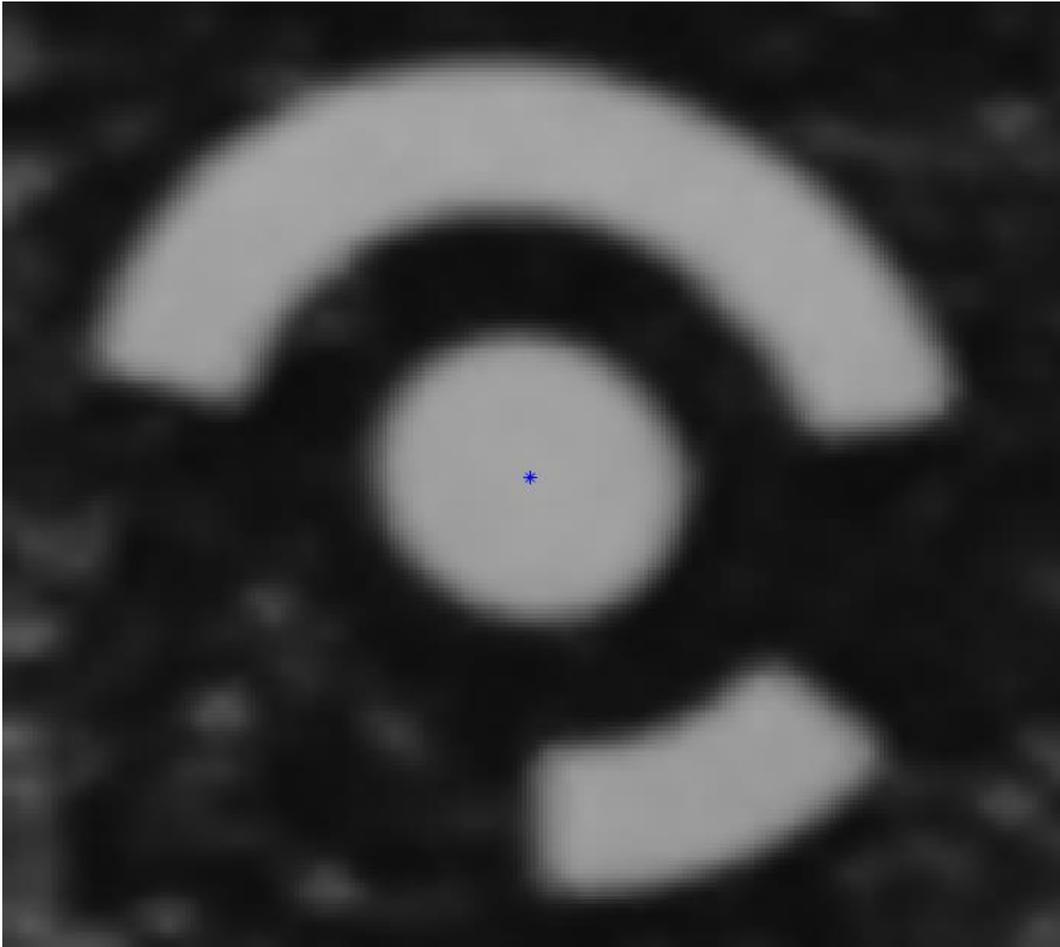
Photo 4.2 Resized cropped image by a factor of 4

4.1.4. Ellipse fitting on each target

The most robust, accurate and reliable method for the measurement of the targets is the ellipse fitting. Extracting elliptic edges from targets and fitting ellipse equations to them is very fundamental because circular objects, are usually projected as ellipses on images. However, in order to do the ellipse fitting with least squares, edge points are required. These edge points of the targets have been identified by an algorithm called subpixel edge detection which has been developed by Agustin Trujillo-Pino.

This edge detector is based on an edge and acquisition model derived from the partial area effect, which does not assume continuity in the image values (Trujillo-Pino A. 2013).
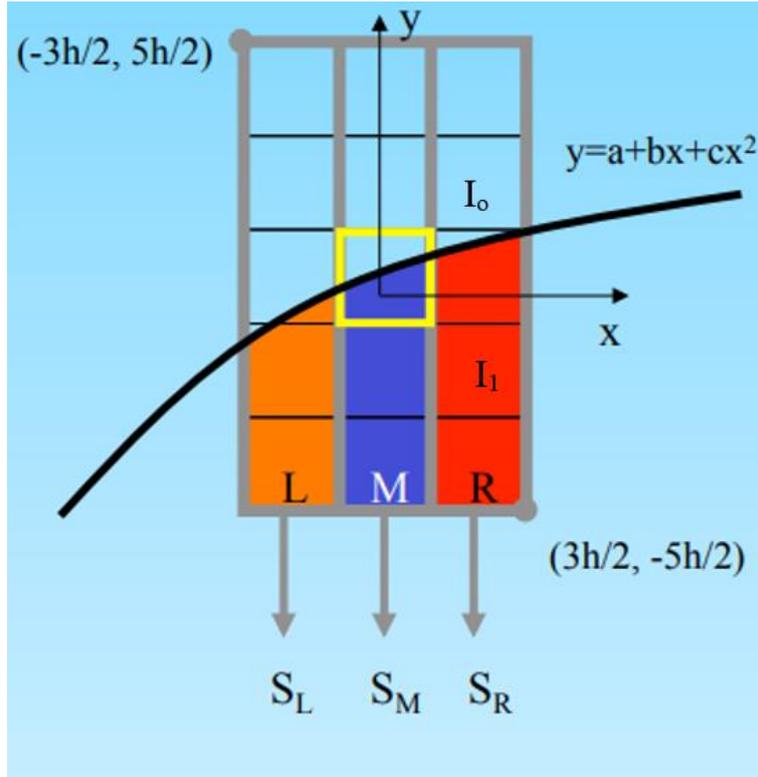
Figure 4.2 Edge estimation (Scandella L. 2017)

Since in most cases the edges are curves (Figure 4.2), these can be estimated by approximating the edge by a second order curve:

$$y = a + bx + cx^2 \qquad (4.12)$$

The intensities on each side are I_o and I_1. The algorithm uses a 5x3 pixel window, centered on a pixel, moving on the image. In each window, the areas under the curve S_L, S_M and S_R are calculated.

Therefore, a 3-equation system is obtained using the sums of the 3 columns of the window. Then, the values of coefficients a, b, c are obtained solving the system (Trujillo-Pino A. 2013).

$$
\begin{aligned}
c &= \frac{S_L + S_R - 2S_M}{2(A - B)} \\
b &= \frac{S_R - S_L}{2(A - B)} \\
a &= \frac{2S_M - 5(A + B)}{2(A - B)} - \frac{1}{12}c
\end{aligned}
\qquad (4.13)
$$

72

From these parameters, the normal vector of the edges can be calculated:

$$N = \frac{I_1 - I_o}{\sqrt{1 + b^2}} [b, -1] \tag{4.14}$$

The curvature is defined by:

$$K = \frac{2c}{(1 + b^2)^{3/2}} \tag{4.15}$$

The algorithm is able to extract all the following information for each edge point with sub-pixel precision:

- The coordinates x and y of the edge in the image coordinate system.
- The normal vector N
- The intensities I_o and I_1 on both sides
- The curvature K

The coordinates of the edge points are going to be used later as observations for the least squares adjustment of the ellipse fitting. There are two ways that the least squares can be used for the adjustment of ellipse fitting.

The first one is to use the parametric equations of an ellipse (Stackexchange Mathematics 2018).

These equations are:

$$x(a) = R_x \cos(a) \cos(t) - R_y \sin(a) \sin(t) + C_x \tag{4.16}$$

$$y(a) = R_x \cos(a) \sin(t) + R_y \sin(a) \cos(t) + C_y \tag{4.17}$$

Where:

- C_x is center x of the ellipse.
- C_y is center y of the ellipse.
- R_x is the half major axis.
- R_y is the half minor axis.
- a is the angle between the half major axis and the line that connects the center of the ellipse with the edge point.
- t is the rotation angle of the ellipse.

The values of the angle 'a' are already known with a good approximation since the center of the ellipse is defined from the regionprops at the detection.
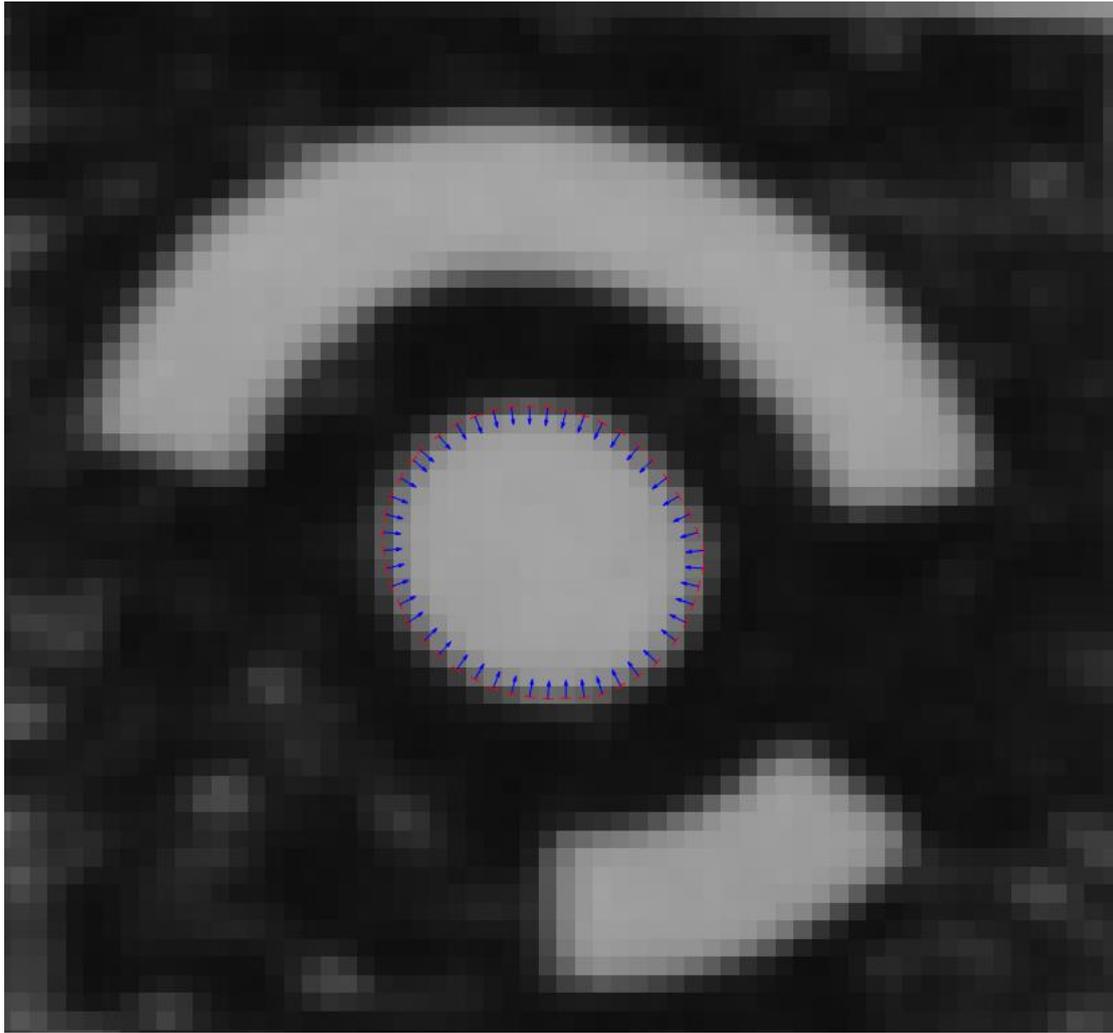
Photo 4.3 Sub-pixel Edge detection on a target

$$a = atan2(\frac{C_x - x_i}{C_y - y_i})$$ (4.18)

Where:

- x_i is the x-coordinate of an edge
- y_i is the y-coordinate of an edge

From the equations 4.16 and 4.17 it is clear that there are six unknown parameters. However, since each point has a unique value for the parameter 'a', the number of parameters is going to be 5+n, where n is the number of the edge points.

The system of the observation equations in least squares is:

$$A\hat{x} = \delta l + v \tag{4.19}$$

The matrix A is equal to:

$$A = \begin{bmatrix} \dfrac{\partial x}{\partial C_{x1}} & \dfrac{\partial x}{\partial C_{y1}} & \dfrac{\partial x}{\partial R_{x1}} & \dfrac{\partial x}{\partial R_{y1}} & \dfrac{\partial x}{\partial t_1} & \dfrac{\partial x}{\partial a_1} & \cdots & \dfrac{\partial x}{\partial a_n} \\[2ex] \dfrac{\partial y}{\partial C_{x1}} & \dfrac{\partial y}{\partial C_{y2}} & \dfrac{\partial y}{\partial R_{x1}} & \dfrac{\partial y}{\partial R_{y1}} & \dfrac{\partial y}{\partial t_1} & \dfrac{\partial y}{\partial a_1} & \cdots & \dfrac{\partial y}{\partial a_n} \\[2ex] \vdots & & & & & & & \vdots \\[2ex] \dfrac{\partial x}{\partial C_{xn}} & \dfrac{\partial x}{\partial C_{yn}} & \dfrac{\partial x}{\partial R_{xn}} & \dfrac{\partial x}{\partial R_{yn}} & \dfrac{\partial x}{\partial t_n} & \dfrac{\partial x}{\partial a_n} & \cdots & \dfrac{\partial x}{\partial a_n} \\[2ex] \dfrac{\partial y}{\partial C_{xn}} & \dfrac{\partial y}{\partial C_{yn}} & \dfrac{\partial y}{\partial R_{xn}} & \dfrac{\partial y}{\partial R_{yn}} & \dfrac{\partial y}{\partial t_n} & \dfrac{\partial y}{\partial a_n} & \cdots & \dfrac{\partial y}{\partial a_n} \end{bmatrix} \tag{4.20}$$

Where:

$$\frac{\partial x}{\partial t} = R_y \sin(a)\cos(t) - R_x \cos(a)\sin(t) \tag{4.21}$$

$$\frac{\partial x}{\partial C_x} = 1 \tag{4.22}$$

$$\frac{\partial x}{\partial C_y} = 0 \tag{4.23}$$

$$\frac{\partial x}{\partial R_x} = \cos(a)\cos(t) \tag{4.24}$$

$$\frac{\partial x}{\partial R_y} = \sin(a)\sin(t) \tag{4.25}$$

$$\frac{\partial x}{\partial a} = R_y \cos(a)\sin(t) - R_x \sin(t)\cos(a) \tag{4.26}$$

$$\frac{\partial y}{\partial t} = -R_x \cos(a)\cos(t) - R_y \sin(a)\sin(t) \tag{4.27}$$

$$\frac{\partial y}{\partial C_x} = 0 \tag{4.28}$$

$$\frac{\partial y}{\partial C_y} = 1 \tag{4.29}$$

$$\frac{\partial y}{\partial R_x} = -\cos(a)\sin(t) \tag{4.30}$$

$$\frac{\partial y}{\partial R_y} = \sin(a)\cos(t) \tag{4.31}$$

$$\frac{\partial x}{\partial a} = R_y\cos(a)\cos(t) + R_x\sin(t)\cos(a) \tag{4.32}$$

Since, there are available approximate values for all the parameters these derivatives can be calculated in order to make the first A matrix.

Then the matrix N is calculated:

$$N = A^T A \tag{4.33}$$

$$\delta l = \begin{bmatrix} x_{observed} - x_{calculated} \\ \vdots \\ y_{observed} - y_{calculated} \end{bmatrix} \tag{4.34}$$

$$u = A^T \delta\lambda \tag{4.35}$$

$$\hat{x} = N^{-1}u \tag{4.36}$$

The matrix $\hat{x}$ will be equal to :

$$\hat{x} = \begin{bmatrix} \delta C_{x1} \\ \delta C_1 \\ \delta R_{x1} \\ \delta R_{y1} \\ \delta t_1 \\ \delta a_1 \\ \vdots \\ \delta C_{xn} \\ \delta C_{yn} \\ \delta R_{xn} \\ \delta R_{yn} \\ \delta t_n \\ \delta a_n \end{bmatrix} \tag{4.37}$$

Hence, the corrections for the unknown parameters are determined. Thus, the new values for the parameters are going to be:

$$C_x{'} = C_x + \delta C_x \tag{4.38}$$

$$C_y{'} = C_y + \delta C_y \tag{4.39}$$

$$R_x{}' = R_x + \delta R_x \tag{4.40}$$

$$R_y{}' = R_y + \delta R_y \tag{4.41}$$

$$t' = t + \delta t \tag{4.42}$$

$$a' = a + \delta a \tag{4.43}$$

The new values for the parameters will be used in order to determine the new matrix A and the least squares adjustment will be carried again. The process will stop when the values δC_x and δC_y of matrix $\hat{x}$ will be minimized and converged.

After the successful calculation of the final values of the parameters, the variance and covariance V_x matrix should be computed in order to determine the precision of the calculation for the ellipse centers and the rest of the parameters (Agatza-Balodimou A.M. 2009).

$$v = A\hat{x} - \delta l \tag{4.44}$$

$$\sigma_o = \sqrt{\frac{[v^T v]}{n - m}} \tag{4.45}$$

$$V_x = \sigma_o N^{-1} \tag{4.46}$$

Where

n   :   the number of the observations

m   :   the number of independent unknown parameters

By the least squares approach the best-fit ellipse can be determined, which will include the most reliable and precise coordinates for each ellipse center (Photo 4.4).

After the end of the ellipse fitting, two conditions have been set in order to check the quality of the measurement.

The first condition is to check if the determination of the center of the ellipse has both on x and y axis a minimum precision of ± 0.5 μm, otherwise if the standard deviation of x and y exceeds that value the point is excluded from the list of targets.

The second condition is to check the residuals of the edge points that have been used during the ellipse fitting. The condition that has been set, aims to exclude edge points which have residuals higher than $3 \cdot \sigma_o$., namely 99.7% confidence level. As it is known 3 standard deviations account for 99.7%. Hence points that have residuals that are higher than this value must be excluded as observations and a new least squares adjustment should be carried out in order to define more precisely the ellipse. It should be mentioned that in order to apply a least squares adjustment a minimum of six edge points should be available.
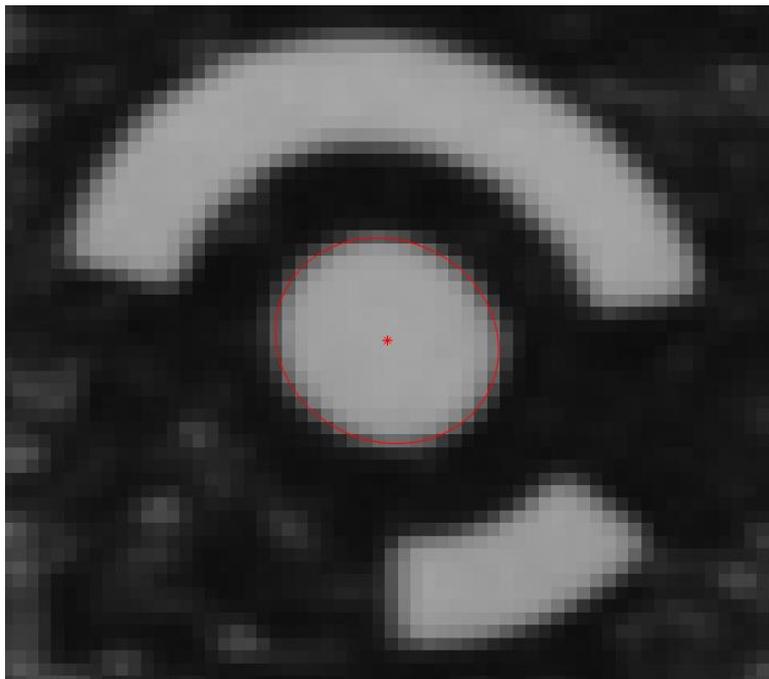
Photo 4.4 Ellipse fitting result

The aforementioned second condition is very important in order to exclude points when targets are damaged. For instance, at the figure 4.3, there is a damaged target which is not circular. The subpixel edge detection will find all the edges as previously, however a calculation of an ellipse with all the edge points will provide an ellipse which is not representative of a target. Thus, the center of the target will not be the correct one. In order to avoid that, the points on the right side of that target should be excluded since they are going to have residuals higher than $3 \cdot \sigma_o$. The new ellipse will be calculated ignoring these edges and using all the others which are not damaged. This will increase the precision of the method and its reliability.
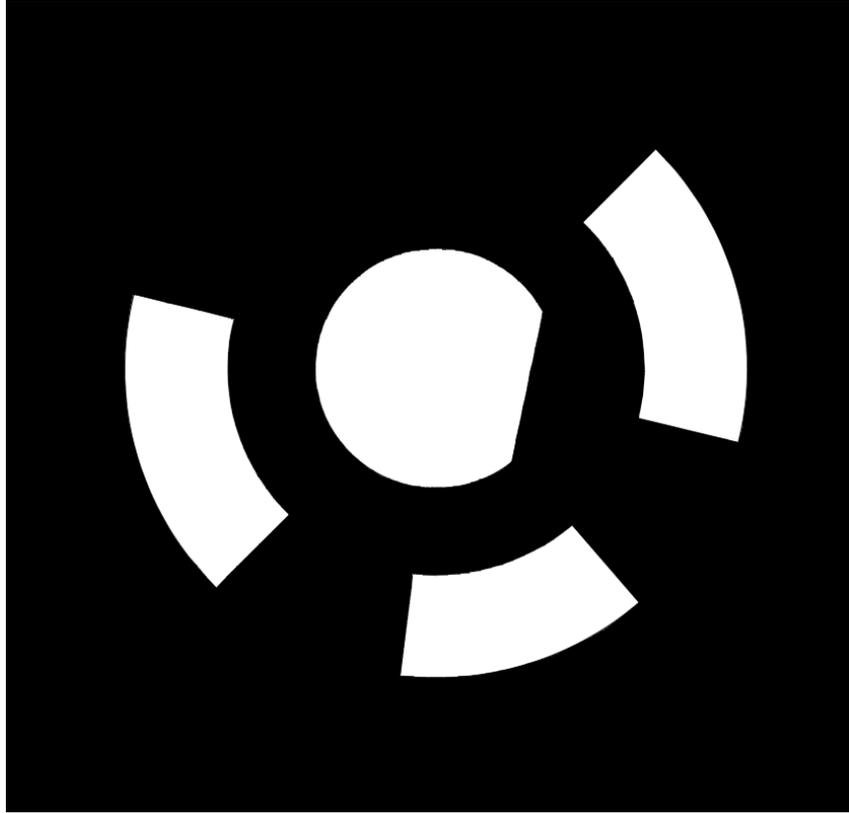
Figure 4.3 Damaged target

Another way to make an algorithm for fit ellipse is to use the general equation for conic section (Zhan Y. 2014):

$$Ax^2 + Bxy + Cy^2 + Dx + Ey + F = 0 \qquad (4.47)$$

The equation 4.47 can be simplified if it is divided by –F to:

$$\tilde{A}x^2 + \tilde{B}xy + \tilde{C}y^2 + \tilde{D}x + \tilde{E}y = 1 \qquad (4.48)$$

Like previously the observations are the x and y coordinates of the edges.

In this case the matrix *A* is as follows:

$$A = \begin{bmatrix} x_1^2 & x_1 y_1 & y_1^2 & x_1 & y_1 \\ x_2^2 & x_2 y_2 & y_2^2 & x_2 & y_2 \\ \vdots & \vdots & \vdots & \vdots & \vdots \\ x_n^2 & x_n y_n & y_n^2 & x_n & y_n \end{bmatrix} \qquad (4.49)$$

The δl matrix is a column matrix of ones and the number of rows is equal to the number of the observations.

Hence after the least square solution, the matrix $\hat{x}$ is equal to :

79

$$\hat{x} = N^{-1}u = \begin{bmatrix} \tilde{A} \\ \tilde{B} \\ \tilde{C} \\ \tilde{D} \\ \tilde{E} \end{bmatrix}$$

The coordinates of the ellipse center (center of gravity) are:

$$x_o = -\cos(\theta)\frac{D'}{2A'} + \sin(\theta)\frac{E'}{2C'} \qquad (4.50)$$

$$y_o = -\sin(\theta)\frac{D'}{2A'} - \cos(\theta)\frac{E'}{2C'} \qquad (4.51)$$

Where:

$$A' = Ac^2 + Bcs + Cs^2 \qquad (4.52)$$

$$C' = As^2 - Bcs + Cc^2 \qquad (4.53)$$

$$D' = Dc + Es \qquad (4.54)$$

$$E' = -Ds + Ec \qquad (4.55)$$

$$\theta = \frac{1}{2}\arctan(\frac{B}{A-C}) \qquad (4.56)$$

$$c = \cos(\theta), s = \sin(\theta) \qquad (4.57)$$

These two methods that are mentioned are proposed for the ellipse fit, however the first one with the usage of the parametric equations of ellipse provides slightly better results due to several simplifications that are accepted in the second method.

4.2. Advantages and disadvantages of the algorithms

Each algorithm presented has its own advantages and disadvantages.

The algorithm that uses the *regionprops* function on the cropped image, is relatively quick. However it lacks precision and this can be verified through various results like the standard deviations of the residuals and the RMS that is achieved by bundle adjustment using the AICON software when the image coordinates that are provided come from this algorithm.

The algorithm that uses the *regionprops* function on the resized cropped image, provides better results. The precision achieved is higher with a relatively quick processing time. However, there is no indication of the quality of the targets image coordinates, that later are going to be used as input in the bundle adjustment. Nevertheless, after various tests the RMS from the bundle adjustment reveals that this method is precise and could be considered as a method for measuring targets.

Finally, the ellipse fitting using the parametric equation of ellipse provides high precision and reliability. The RMS after the bundle adjustment that is achieved is of the same level as the one that is achieved by AICON using AICON image coordinate measurements. Due to the least squares adjustment, standard deviations for each center are provided, which is very important for the evaluation of the quality of the position determination for each target. However, the time required for the processing is slightly higher than for the other algorithms due to the iterations during the least squares calculations.

Overall, it is considered that the algorithm using the ellipse fitting with the parametric equation of ellipse, is the most robust and reliable. Hence it should be chosen as one of algorithms that is going to make the target measurement. The ellipse fitting using the conic section provides almost equivalent results, with the parametric, however the precision is slightly lower due to mathematical simplifications. Thus for the ellipse adjustment the mathematical model was chosen the parametric equations of ellipse and all the tests of precision for the ellipse fit were based on that model.

On the following subchapter, a more in depth analysis for various results concerning 5 different projects (Table 4.1) is going to be presented.

4.3. Analysis of the results for the measurement algorithms

In order to be able to analyze, compare and interpret the results, the same observations should be used for all the algorithms. Hence, filtering and sorting of the targets was carried out in order to keep for all the developed algorithms of the position determination and the AICON, exactly the same observations. Targets which were present as observations for instance to AICON but not for the developed algorithms, were excluded and not used.
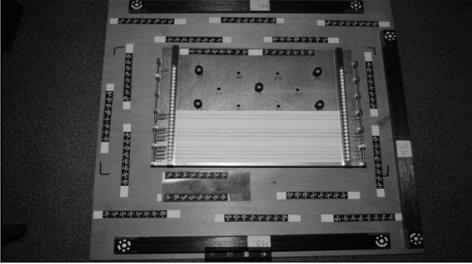
Project 1	Project 2
Project 3 (LHC mockup)	**Project 4 (LHC)**
Project 5 (LHC)	
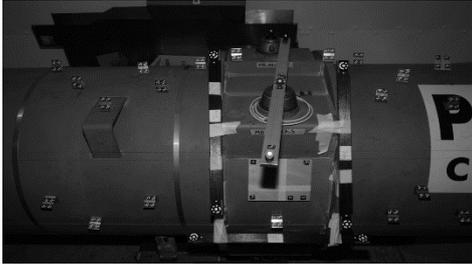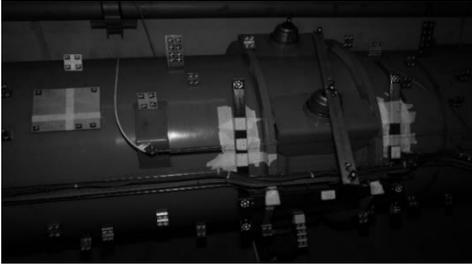
Table 4.1 Photogrammetric test projects

After the bundle adjustment a large amount of data is available to be extracted, which are able to define which algorithm is the most reliable and precise.

As in the chapter of the detection, the reference for the comparison of the detected points that was done, was AICON, also at the position determination of targets, AICON is going to be used again as reference.

After the bundle adjustment, the residuals of the image coordinates on each point on each image are available. The standard deviation of the residuals on each project will provide the precision that was achieved for the two dimensional position determination.

The precision on the 2D target position determination that is achieved by AICON is typically $\pm$ 0.03 pixel up to $\pm$0.05 pixel on both σ_x and σ_y, ellipse fitting also provides equivalent level of precision, which is equal to $\pm$ 0.03 pixel to $\pm$0.05 pixel on both σ_x and σ_y (Fig. 4.6 & 4.7). The rest

of the position determination algorithms provide precisions which are equal or exceed ±0.05 pixel.

The position determination of targets which is achieved by using *regionsprops* on a resized cropped image, even though on some individual targets is able to provide results which are determined with a high precision, however, due to the fact that a quality estimator for each individual point is absent, it is more prone to include blunders on the measurement. The blunders may have a significant impact due to the resizing of target by a scale, which is not the case on the ellipse fitting due to the least squares adjustment where the results of the variance – covariance matrix allow the estimation of the quality of a target.

Both AICON and the developed algorithm for the ellipse fitting use least squares adjustment in order to find the image coordinates for the center of the ellipse. Both provide to the user the standard deviations of the x and y component which can be used in order to evaluate the measured center of the ellipse (Fig. 4.4 & Fig. 4.5). Despite the fact that these values are too optimistic, they are very useful to exclude blunders. AICON provides the option to increase the number of rays at the target measurement. The increasement on the number of rays decreases the values of the standard deviations, however the precision itself is not increased despite the indication that the standard deviation is getting smaller. The default ray value that AICON uses is 64 rays. This value as it is shown on the figures 4.4 and 4.5 provide standard deviations, which are similar to the ones that the developed algorithm for the ellipse fitting.

The precisions for the 2D image coordinates that can be achieved by the least squares adjustment are for the ellipse fitting about ±0.009 pixel on both x and y component. For the AICON 64 rays are abound ±0.010 pixel on both x and y component. These precision values compared to the precisions of the 2D image coordinates after the bundle adjustment which are about ±0.04 pixel, are very optimistic.

There might be several reasons why such a difference is occurred. First is that the observations that are used both in the ellipse adjustment and in AICON are not completely independent. The subpixel edge detector uses a 3X5 pixel window in order to find the edges, which means that nearby edge intensity values are not independent and affect the outcome of the edge detector. The same goes for AICON where it is obvious that the bigger the number of rays is, the smaller the values for the standard deviations become. This is due to the fact that the number of observations increase by using same observations. Furthermore, the camera that is used is a non-metric camera, which might have an influence. The chip itself

and whether is completely flat or not might also have an influence, as well as the parts of the distortion that are linked to the distance. Hence, there might be a great number of reasons that account for these differences, which should to be investigated.
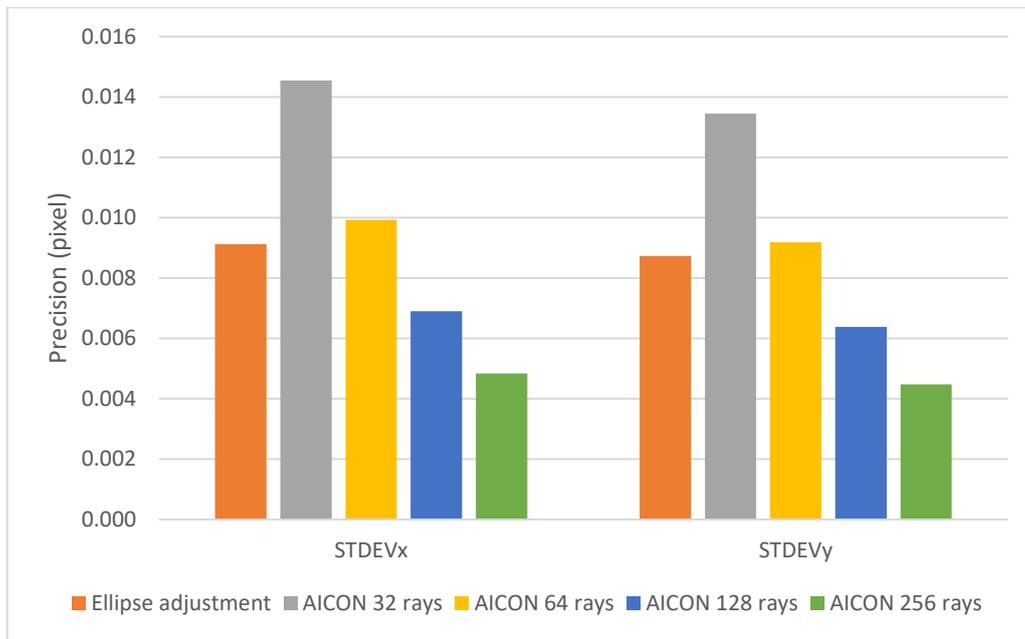
Figure 4.4 Precision of the 2D target position determination for project 1 as a result of least squares adjustment for ellipse fitting and AICON
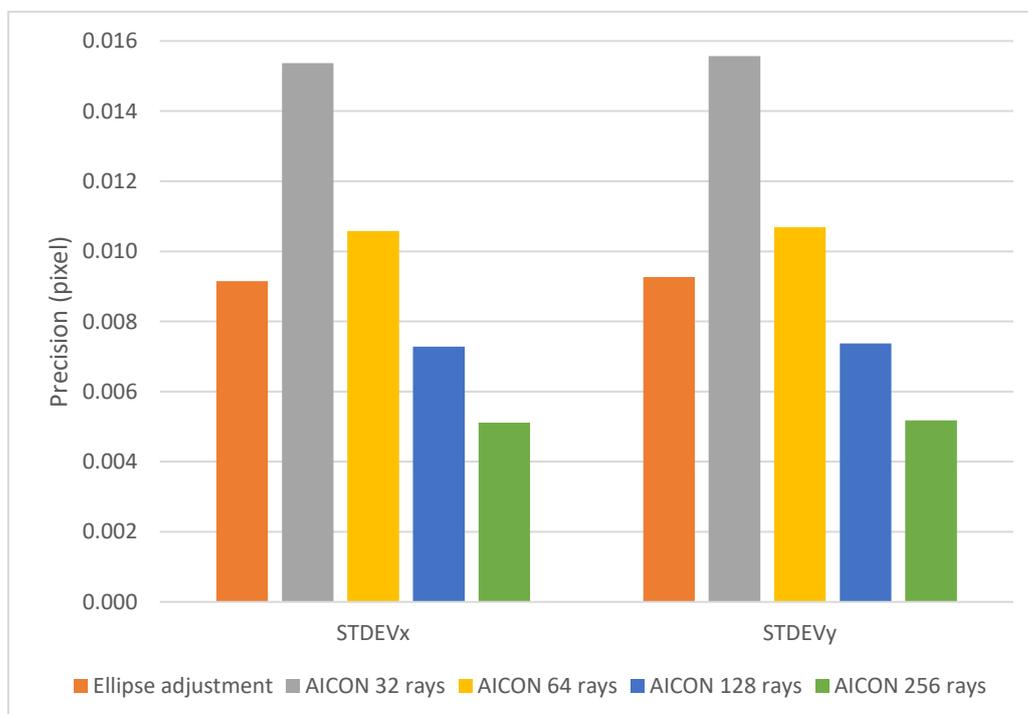
Figure 4.5 Precision of the 2D target position determination for project 4 as a result of least squares adjustment for ellipse fitting and AICON

Figures 4.6 and 4.7, present the precisions of the 2D image coordinates of points after the bundle adjustment. Among the algorithms that have been developed to determine the 2D position of the targets on the images the one that provides the highest precision is the Ellipse fitting. This algorithm provides precisions nearly equal with the ones that AICON provides.

Both they provide precisions around ± 0.03 pixel to ± 0.05 pixel, depending on the distribution of the points and the conditions that are present during the capture of the images.

For the projects 3 (LHC mockup), 4 and 5 (both LHC) which have same configurations, the precisions are of the order of $\pm$ 0.048 pixel for the x component and $\pm$ 0.040 pixel for the y component, by using either AICON and or ellipse fitting.

In the figures 4.8 and 4.9, the residuals of the 2D image coordinates on project 4 for the AICON and the tested algorithms are presented. The figures show that the AICON and the ellipse adjustment are able to provide the best results concerning the residuals, where the concentration of residuals that are between -0.02 pixel to 0.02 pixel is higher compared to the other measurement algorithms.

The distribution of the residuals shows that the most suitable algorithm between the developed algorithms for the target position determination is the Ellipse adjustment-fitting which provides residuals closer to the ones that AICON provides which are concentrated mainly on small values. It should be mentioned that for the tests at the LHC the camera that was used was the Nikon D3X which has a pixel size of 5.9 μm.

By figures 4.8 and 4.9 it is obvious that the concentration of the residuals around 0 pixel is higher on the y component rather than on the x component. One of the reasons that such a phenomenon occurs is the fact that the images are not square, but rather rectangular, with the larger dimension on the x. That means that targets that have large x component values are more distorted since they are further from the center of the image and are prone to have higher residual values. Furthermore, the distribution of the points on the magnet bolstered this issue, because there was a limited spread of points on the y direction and the targets had small values on the y-axis, which makes the points to have smaller residuals on the y direction.
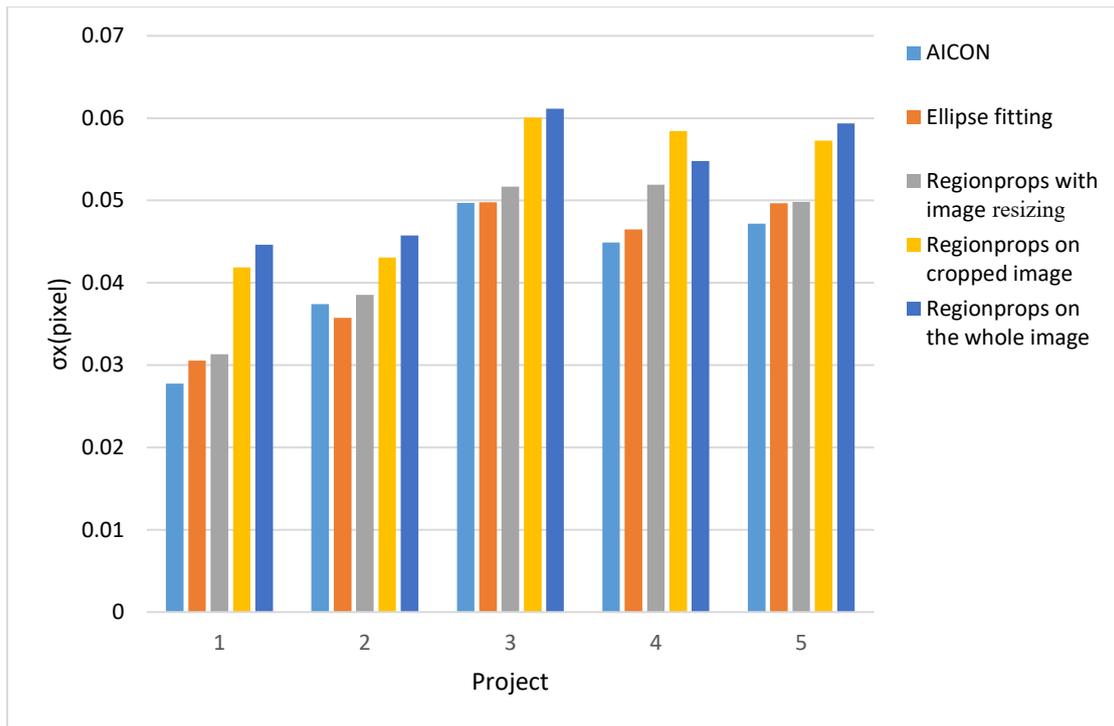
Figure 4.6 Real precision of the 2D target position determination (σ_x) for each project using different position determination algorithms after the bundle adjustment
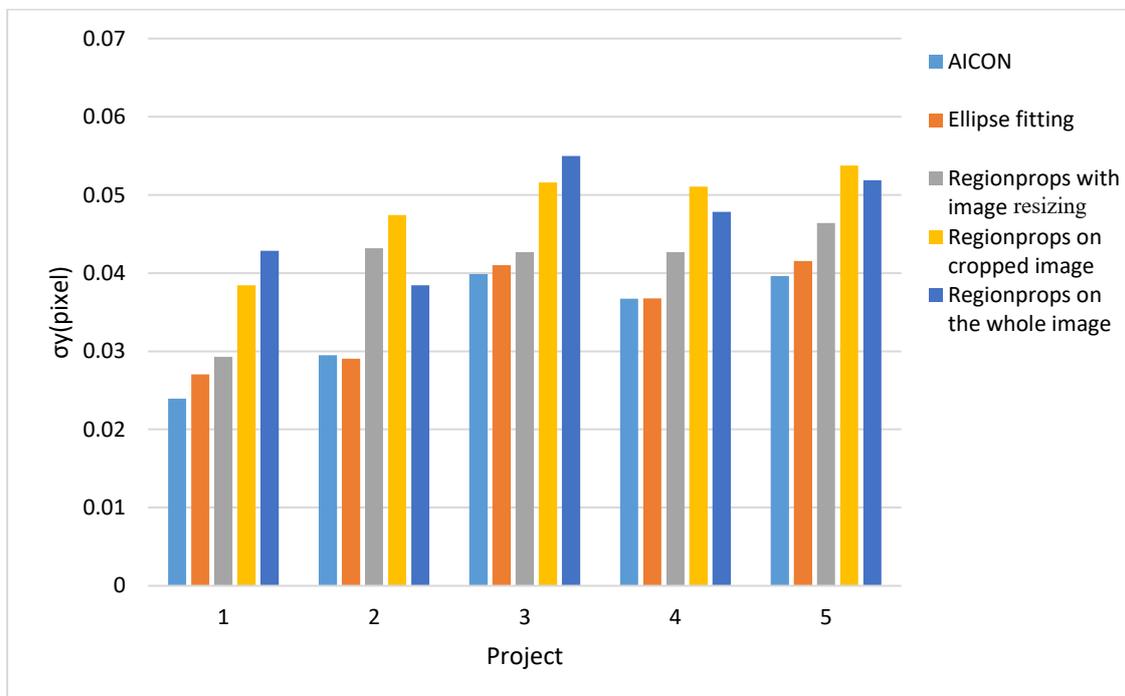
Figure 4.7 Real precision of the 2D target position determination (σ_y) for each project using different position determination algorithms after the bundle adjustment
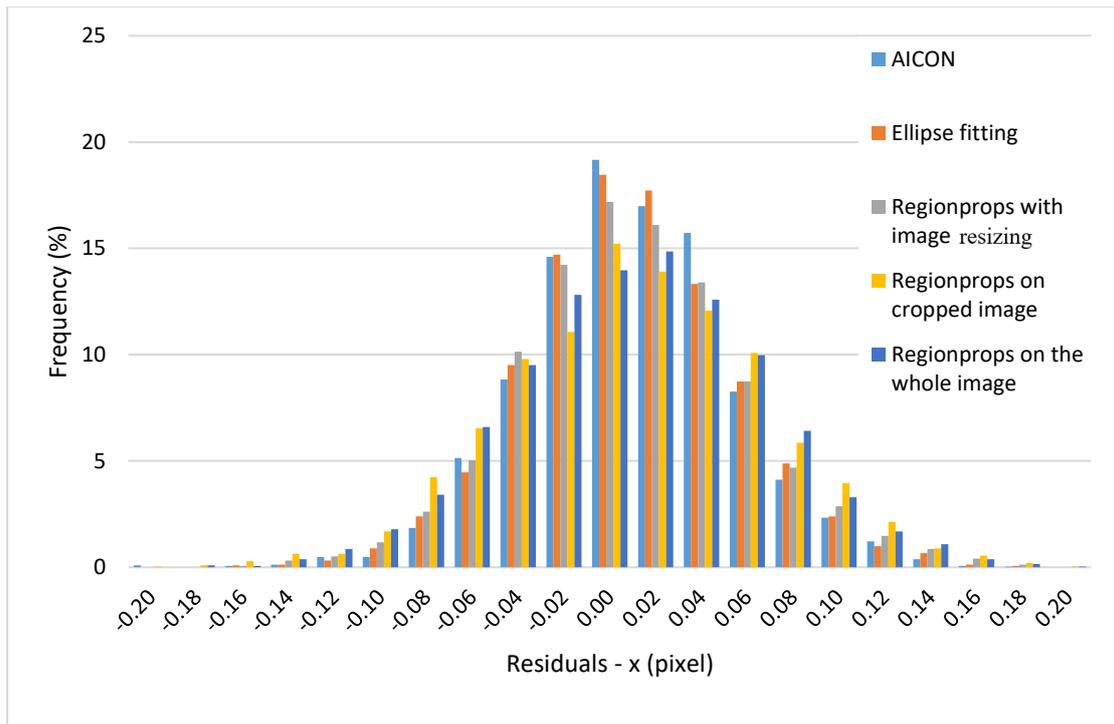
Figure 4.8 Comparison of the 2D image coordinate residuals
(x component) after the bundle adjustment
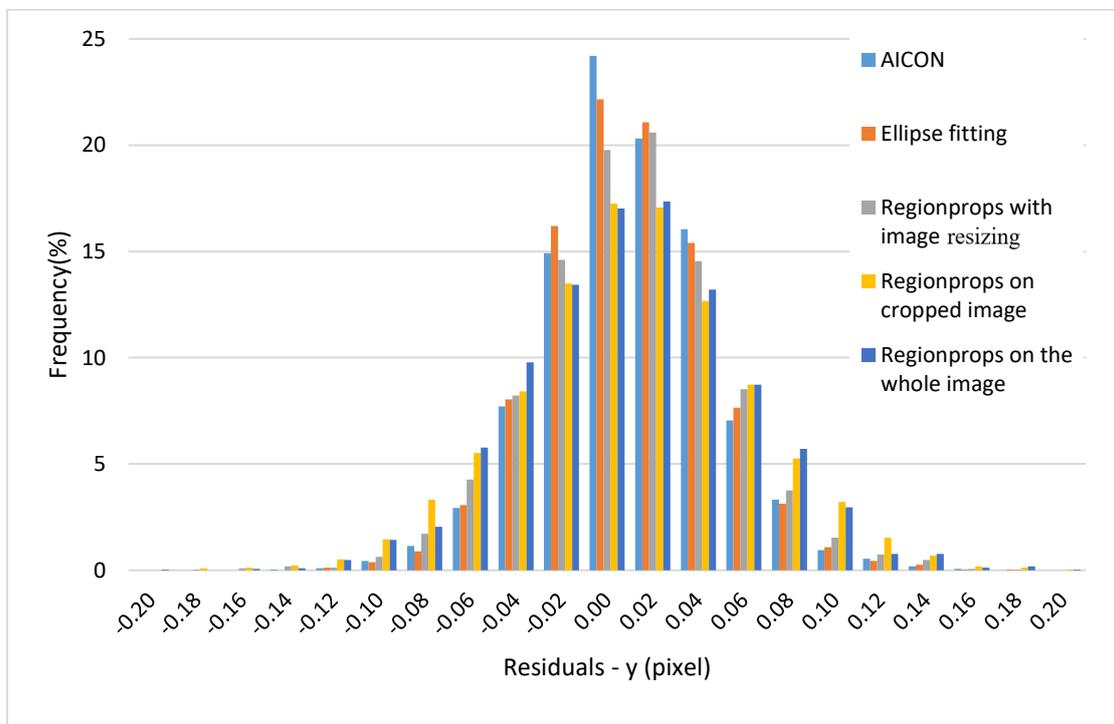
Figure 4.9 Comparison of the 2D image coordinate residuals
(y component) after the bundle adjustment

After the bundle adjustment, the 3D position determination of the targets is available, and the 3D coordinates are generated as well as the σ_o and $RMS_{X,Y,Z}$ for the object points. This verifies that the ellipse fitting provides the closest results to the one that AICON provides.

Figures 4.10 to 4.14 present the RMS on X, Y and Z of the 3D coordinates in the object space for the projects 1 to 5.
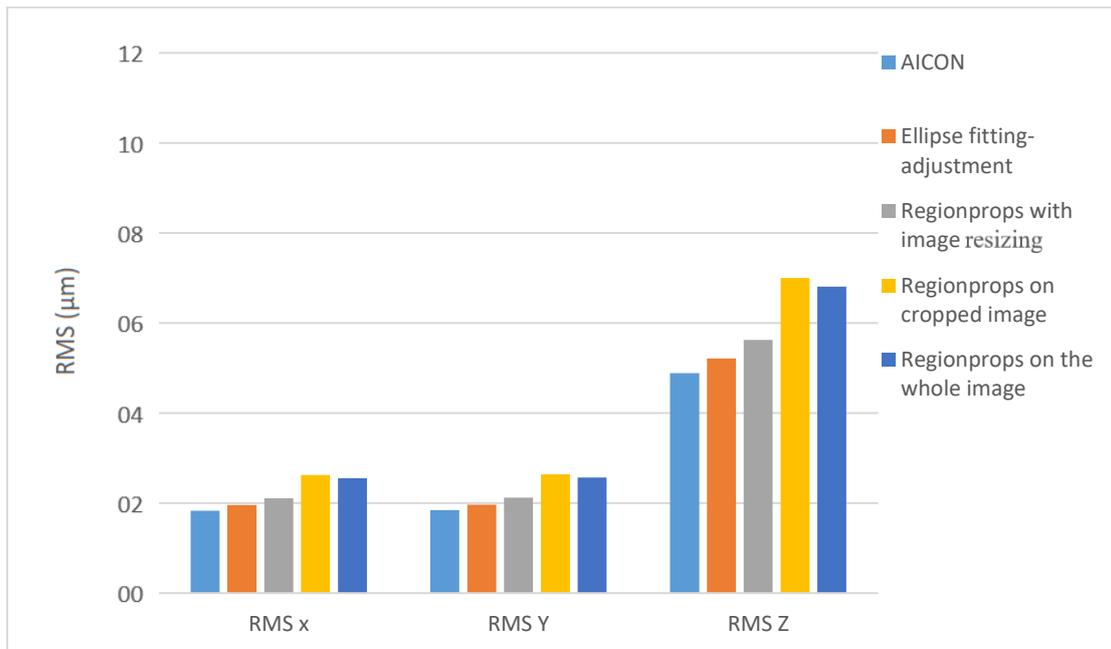
Figure 4.10 RMS for project 1
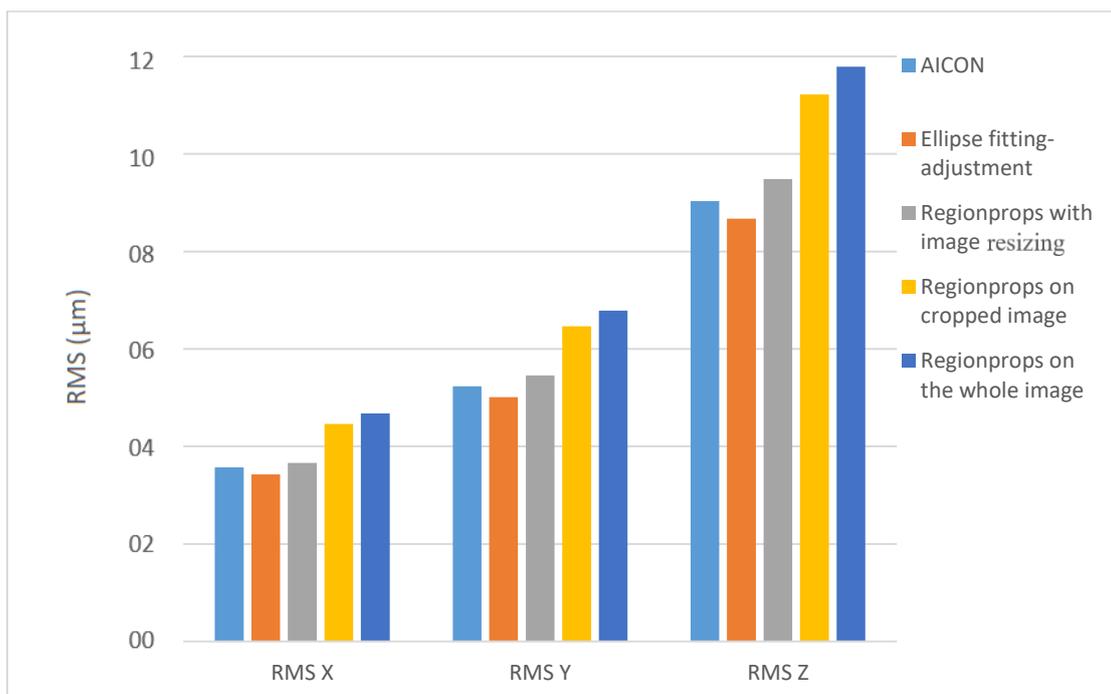
Figure 4.11 RMS for project 2
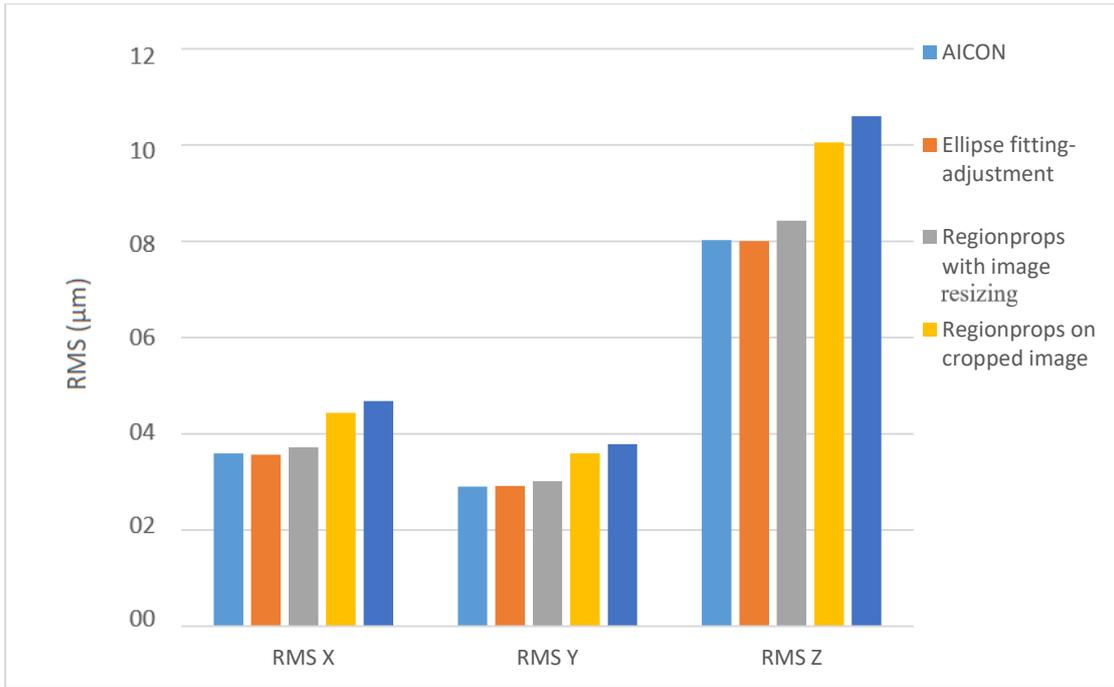
Figure 4.12 RMS for project 3
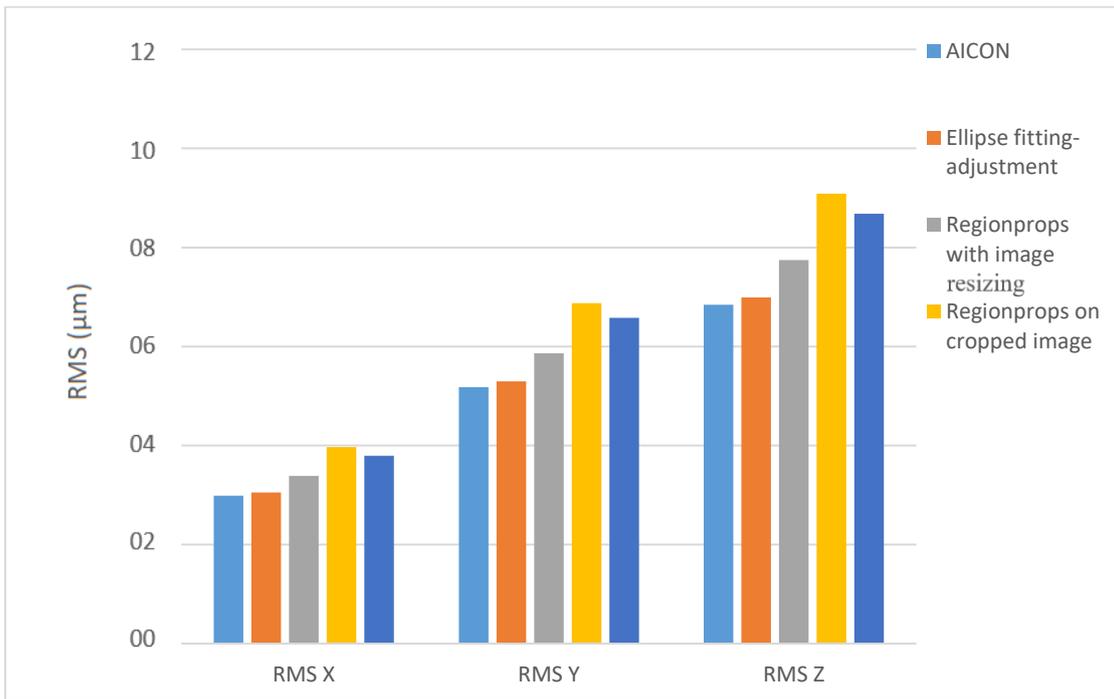
Figure 4.13 RMS for project 4
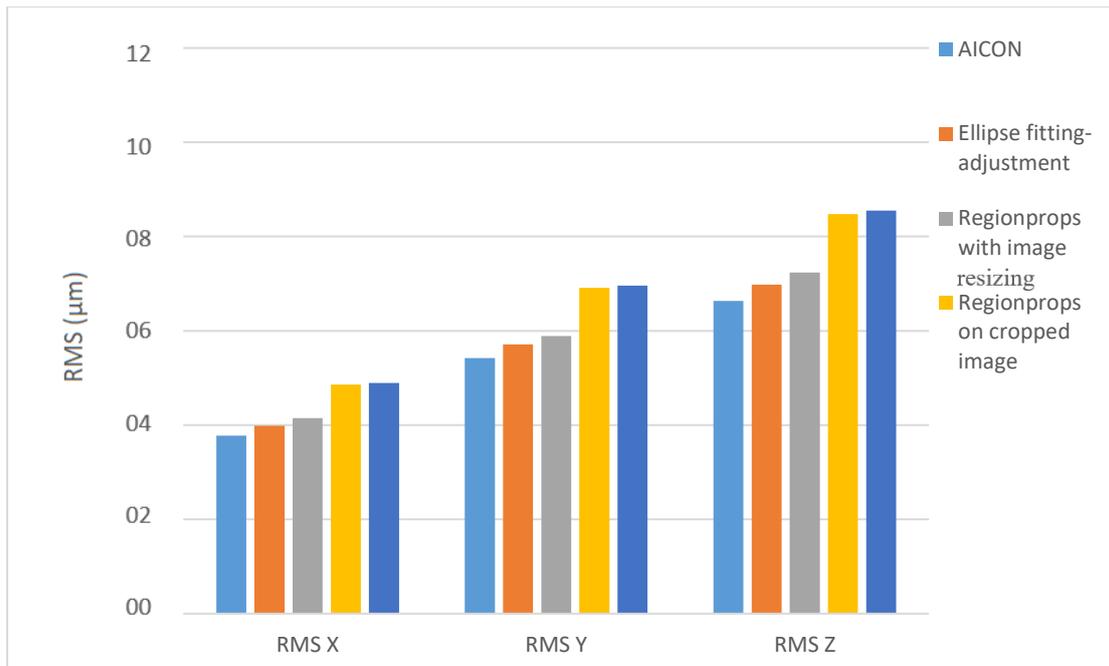
Figure 4.14 RMS for project 5

By executing the bundle adjustment, the object coordinates of the targets are defined. However, in the AICON software, an arbitrary global coordinate system is defined after the bundle adjustment, which is dependent on the cross that has been used to initialize and set the coordinate system. Thus, a point that has been measured with two different algorithms might have different coordinates because the coordinate system after the adjustment has been defined differently. Nevertheless, the relative position of the points should be identical if there is no error during the measurement. Hence, after the best fit transformation there should not be any residuals on the points on the project that has been transformed to another coordinate system. In reality, achieving residuals that are equal to 0 is not possible. However, the lower the residuals are, the better the fitting is done.

Figures 4.19 to 4.23, present the analysis of the results of the best fit transformation has been applied on each project where spatial coordinates have been computed after the adjustment of the target measurements by the different algorithms. The reference spatial coordinates for the transformations have been chosen the ones that have taken into consideration by AICON target measurements.

Once again, the best fit transformation between the points that have been computed using the ellipse fitting and AICON, have much smaller residuals, which indicates the compatibility of the measurements with the AICON measurements.
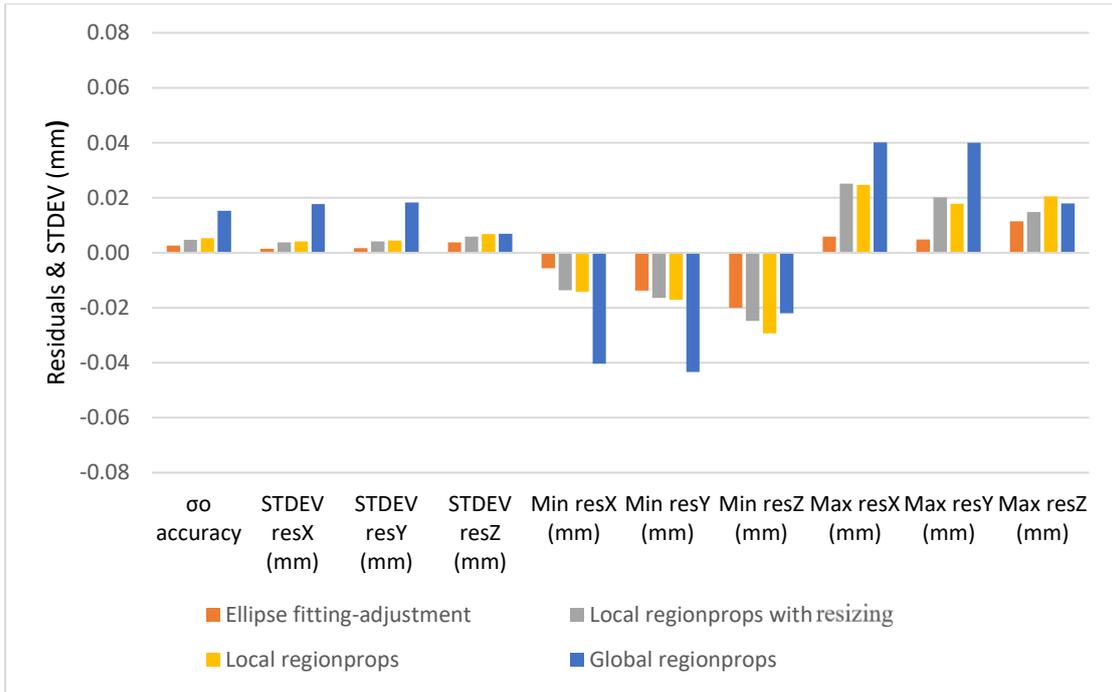
Figure 4.15 Residuals and STDEV of spatial coordinates of targets, measured by the developed algorithms on project 1 after the best fit transformation that uses as reference the spatial coordinates of targets which have been measured by AICON
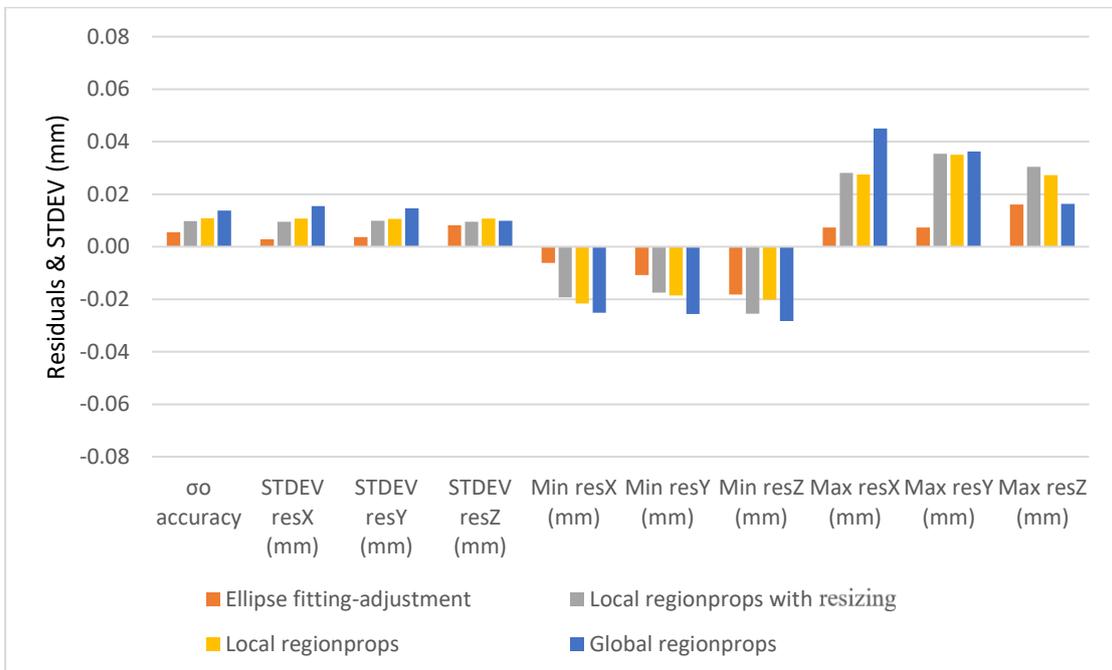
Figure 4.16 Residuals and STDEV of spatial coordinates of targets, measured by the developed algorithms on project 2 after the best fit transformation that uses as reference the spatial coordinates of targets which have been measured by AICON
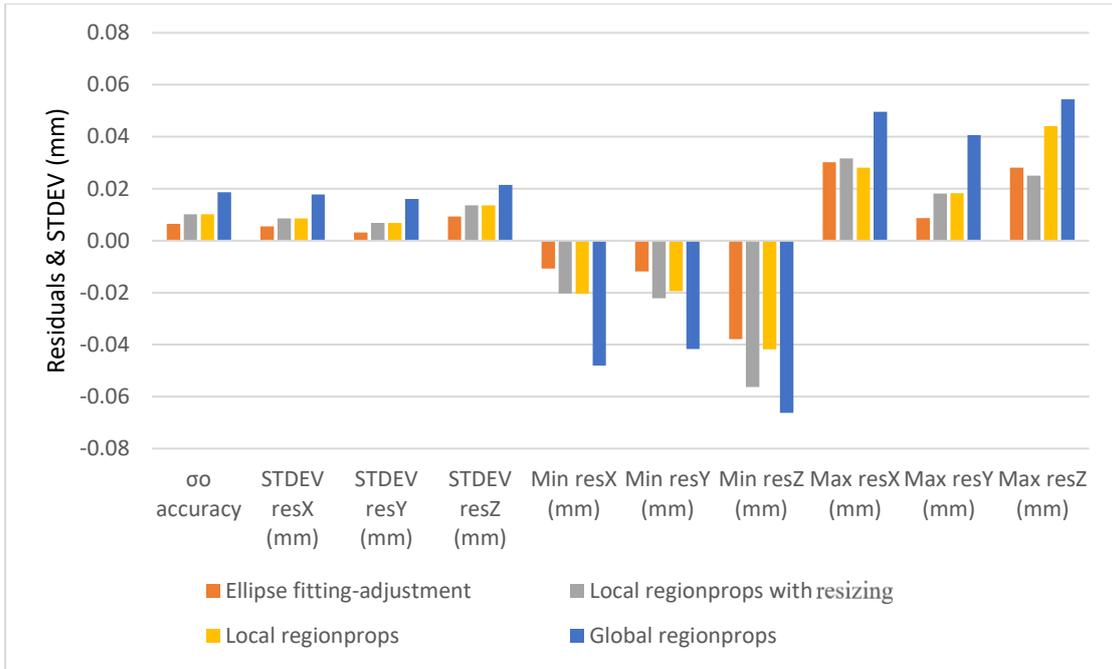
Figure 4.17 Residuals and STDEV of spatial coordinates of targets, measured by the developed algorithms on project 3 after the best fit transformation that uses as reference the spatial coordinates of targets which have been measured by AICON
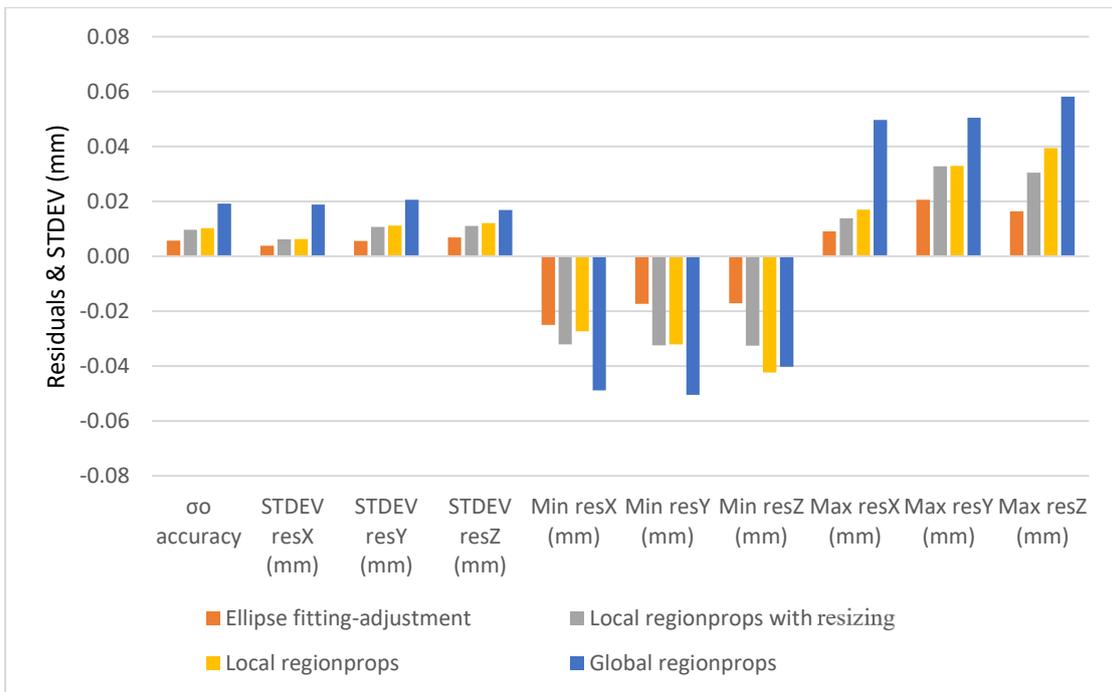
Figure 4.18 Residuals and STDEV of spatial coordinates of targets, measured by the developed algorithms on project 4 after the best fit transformation that uses as reference the spatial coordinates of targets which have been measured by AICON
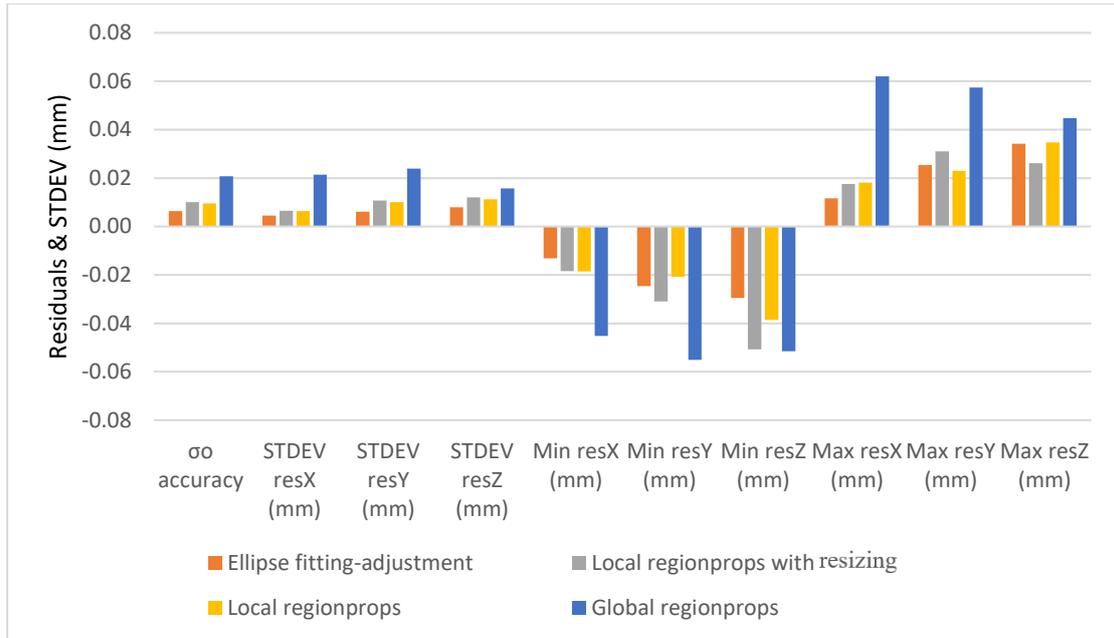
Figure 4.19 Residuals and STDEV of spatial coordinates of targets, measured by the developed algorithms on project 5 after the best fit transformation that uses as reference the spatial coordinates of targets which have been measured by AICON

The standard deviations of the residuals on project 3 (LHC mockup), project 4 (LHC) and project 5 (LHC) for the transformation of the object points whose targets positions have been determined using ellipse fitting, are about 5-6 μm on the X and Y component and for the Z they are of the order of 8 μm. These differences on the object space are not significant because they are on the same order as the RMS at the X, Y and Z component (Table 4.2).

	RMS X (mm)	RMS Y (mm)	RMS Z (mm)	STDEV Transformation Res X (mm)	STDEV Transformation Res Y (mm)	STDEV Transformation Res Z (mm)
Project 1	0.0018	0.0018	0.0049	0.0015	0.0017	0.0038
Project 2	0.0034	0.0050	0.0087	0.0028	0.0036	0.0081
Project 3	0.0036	0.0029	0.0080	0.0055	0.0032	0.0093
Project 4	0.0031	0.0053	0.0070	0.0038	0.0055	0.0068
Project 5	0.0040	0.0057	0.0070	0.0045	0.0061	0.0079

Table 4.2 RMS of bundle adjustment and STDEV of the residuals after best fitting transformation

Chapter 5

TARGET DECODING

5.1. Photogrammetric encoded targets pattern

Encoded targets are useful for automated photogrammetric processing. They can be used for automated calibration on a test field or as control or reference points. Each encoded target has a unique binary ring around the circular center which indicates its code. The code is read along an ellipsoid path around the center (Böhm J. 2018).

The encoded targets that are usually used are 12, 14 and 20bit. The number of bits reveals the total amount of code segments in a target. For instance, a 12-bit encoded target has 12 code segments which might be black or white. Figure 5.1 presents a 12-bit coded target with its code segments.
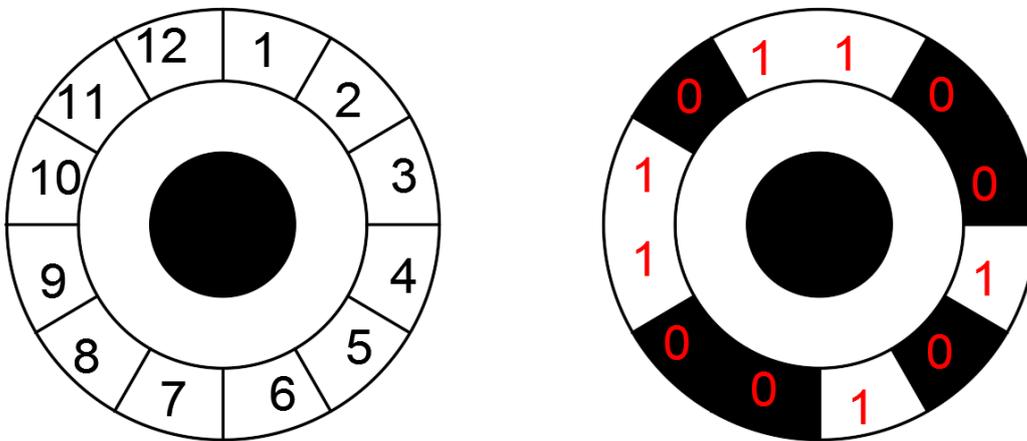
Figure 5.1 Example of 12bit encoded photogrammetric target

The principle for the decoding of the targets is to find the binary number that is generated by the sequence of the code segments. Figure 5.1 presents a possible binary code for the target is 110110010100 which in the decimal system is the number 3476. However, this is not the final ID for the target because the binary number sequence that creates the smallest decimal number needs to be found. Once the smallest number is found, the final code will be assigned from a look up table.

5.2. Decoding algorithm

In order to start the decoding of the targets, points should be distributed around the targets and specifically they should be on the code segments. If for example, the coded target is 14-bit then 14 points should be dispersed.

By using the ellipse fitting, the *regionprops* on the whole image and the execution of *regionprops* on the cropped images, the half minor and half major axis are available for each target and they can be used in order to spread the points.

The coordinates of the points are (Manolopoulos K. 2017):

$$x_i = 2.5 \cdot a \cdot \cos\left(i \cdot \frac{2\pi}{bit}\right) \tag{5.1}$$

$$y_i = 2.5 \cdot b \cdot \sin\left(i \cdot \frac{2\pi}{bit}\right) \tag{5.2}$$

$$i = 0,1,\dots,bit$$

Where :

- a is the half major axis
- b is the half minor axis

The value 2.5 is chosen in order to have the points in the middle of the segments. Figure 4.1 presents that in order to be inside the code segment part, the coefficient required should be between 2 and 3, hence 2.5 is chosen as the most suitable.

Now these points should be transferred to the coordinate system of each cropped image. Since each target has been cropped from the entire image, there is one target center for each image. Furthermore, the points should be rotated according to the rotation angle of the ellipse. Hence, the transformation that is required for the points is done according to the following formulas (LaValle S. 2018) :

$$x'_i = C_x + x_i \cdot \cos(\theta) - y_i \cdot \cos(\theta) \tag{5.3}$$

$$y'_i = C_y + x_i \cdot \sin(\theta) + y_i \cdot \cos(\theta) \tag{5.4}$$

Where:

- C_x and C_y the local coordinates of the centers of the targets
- θ is the rotation angle of the ellipse

Since, the coordinates of the points on the code segments are determined, their pixel values can also be specified easily.

Knowing the position and the pixel value of each point, a binary number sequence can be created which will be a possible candidate for the final ID of the target.

If the targets are 14-bit then each target has 14 different binary code candidates to determine its final ID. The binary sequence that will provide the minimum value in the decimal system for the ID, is the sequence that should be chosen. In order to find the minimum value, multiple transfers of the first digit to the end of the binary sequence should be done. The multiple transfers of the first digit to the end of the binary sequence are illustrated on the example in the figure 5.2 where the minimum value is 1011 which is generated by the sequence 00001111110011, which corresponds to the code number 170 in AICON.
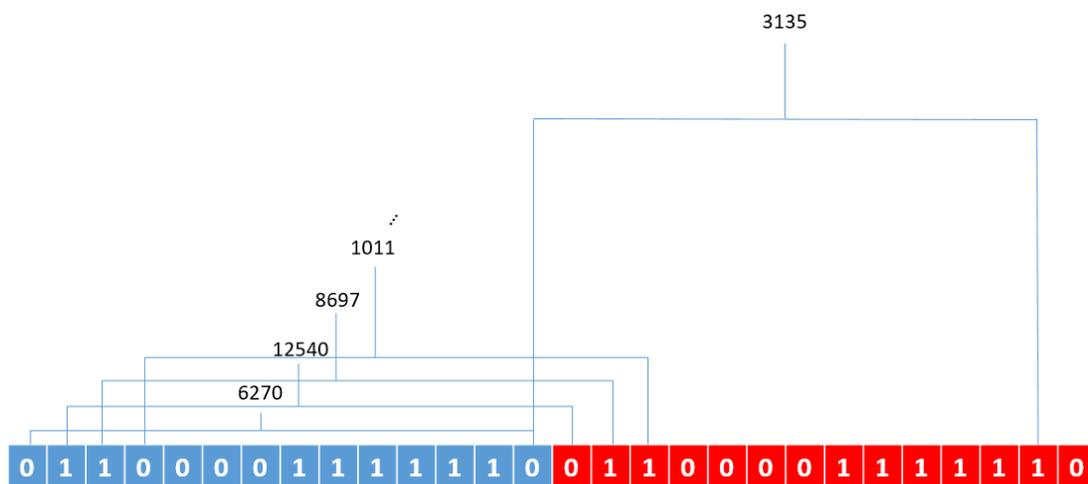
Figure 5.2 Process to find the minimum value from a binary sequence

5.3. The decoding issues

There are several issues, which may cause problems for the correct decoding of the targets. In this section, these issues are presented and a solution for them is proposed.

There are many reasons that the decoding algorithm might not provide satisfactory results. Two of the most common issues are that a target has been identified with a wrong ID and the decoding was not able to provide result.

The first issue is due to the fact that some segments are partially damaged and this may affect the binarization of the image, hence the binary image will include some noise which will be part of the code.

Furthermore, depending on the size of the target, the illumination and the quality of the image, the code segments may be too close, too dark or even their shape may not be the correct one.

In addition, some points spread on the segments might fall on the edge between two code elements, a fact that makes the result of the decoding vague and it is unclear whether the binary sequence that is generated correctly. These factors have an important role on the decoding algorithm and they should be faced.

Another reason why decoding may not be able to provide any results is due to the fact that the target may be uncoded, the target might have damaged or hidden segments or the candidate target identified might not even be a target, thus other objects that have almost same properties as a target have been identified instead.

In order to face these issues, to abate the probability of a false decoding and to make the algorithm more robust, a solution has been proposed.

In order to assure that the code identified is the correct one, the decoding algorithm runs more than one time. Each time using different rotation angle for the ellipse. In this way, the distribution of the points slightly changes, however due to that, it provides more reliability to the decoding. When at least two times, for each target a specific ID is identified then this ID is chosen as the representative of the target.

Depending on the number of segments that each target has, different values for the rotation changes have been chosen (Table 5.1).

BIT	EXTRA ROTATIONS (degrees)				
12	-10+θ	-5+θ	0+θ	5+θ	10+θ
14	-8+θ	-4+θ	0+θ	4+θ	8+θ
20	-6+θ	-3+θ	0+θ	3+θ	6+θ

Table 5.1 Additional rotations in degrees used on the ellipse rotation angle for the identification of the ID of the target

In most cases 14-bit code targets were used during the various tests, hence the decoding algorithm has been run for all the above extra rotation (- 8 deg,-4 deg,+4 deg,+8 deg) with respect to the θ angle.
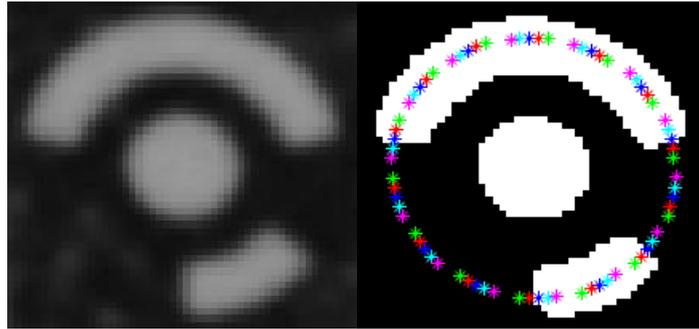
Figure 5.3 Target ID decoding using different rotation angles

In figure 5.3, the blue points are the ones with the initial rotation of the ellipse, which has an extra rotation equal to 0 degrees. The red and the green have extra rotations of 4 and 8 degrees respectively. While the cyan and magenta points have extra rotations equal to -4 and -8 degrees.

All these rotations assure that at least 2 of them will provide the same ID for the target, hence in most cases the ID of the target can be decoded successfully.

During the tests it has been revealed that in order to maximize the efficiency of the decoding, the binarization method should be chosen very carefully. In general, the same illumination and intensity level that the center of a target has, are present also on the code segments. Thus, the intensity value of the center is necessary to be found. Once this is done, the threshold for the binarization is:

$$threshold = 0.55 \cdot PixelValue \qquad (5.3)$$

After several tests, the value 55% is chosen as a reliable value in order to minimize the noise on the targets and in general to distinguish the background with the foreground which is the target itself with its code elements. This value also prohibits the deletion of the code segment during the binarization.

Attention should be given to codes that do not correspond to the lookup tables. If for various reasons a code is generated which does not correspond to the lookup table then the target should be given a random ID and be considered as uncoded target. On the following pages, there are the lookup tables for the 12 (Table 5.3) and 14 (Table 5.4) bit targets which are the most common.

On the projects 1 to 5 as they are mentioned in chapter 4, there have been several tests, in order to find out, how many of the total amount of coded

targets in a project identified by AICON have been assigned the same code number by the developed decoding algorithm.

As it presented in table 5.2 the percentage of mutual codes in all projects is very high, and almost all of the projects have above 95% common decoding. For the missing targets, no codes were assigned.

Project	Coded targets identified by AICON	Same coded assigned both by AICON and developed decoding algorithm	%
1	3724	3722	99.9
2	1320	1248	94.5
3	5441	5292	97.2
4	3187	3150	98.8
5	2746	2657	96.8

Table 5.2 Number of coded targets with mutual code assigned by AICON and developed decoding algorithm and percentage out of the total coded targets identified by AICON

AICON ID	DECODING ID	AICON ID	DECODING ID	AICON ID	DECODING ID	AICON ID	DECODING ID
1	65	45	317	89	621	133	1375
2	71	46	325	90	627	134	1391
3	75	47	329	91	629	135	1399
4	77	48	335	92	639	136	1403
5	83	49	343	93	663	137	1455
6	85	50	347	94	667	138	1463
7	89	51	349	95	669	139	1467
8	95	52	359	96	679	140	1495
9	99	53	363	97	683	141	1499
10	101	54	365	98	685	142	1535
11	105	55	371	99	691	143	1755
12	111	56	373	100	703	144	1791
13	113	57	377	101	715	145	1919
14	119	58	383	102	717	146	1983
15	123	59	399	103	723	147	2015
16	125	60	407	104	725		
17	135	61	411	105	735		
18	139	62	413	106	751		
19	147	63	423	107	759		
20	159	64	427	108	763		
21	163	65	429	109	765		
22	175	66	435	110	821		
23	183	67	437	111	831		
24	187	68	447	112	845		
25	195	69	455	113	853		
26	197	70	459	114	863		
27	201	71	461	115	879		
28	207	72	467	116	887		
29	209	73	469	117	891		
30	215	74	473	118	893		
31	219	75	479	119	927		
32	221	76	485	120	943		
33	231	77	489	121	951		
34	235	78	495	122	955		
35	237	79	503	123	957		
36	243	80	507	124	975		
37	245	81	509	125	983		
38	249	82	585	126	987		
39	255	83	591	127	989		
40	277	84	599	128	1003		
41	287	85	603	129	1005		
42	293	86	605	130	1013		
43	303	87	615	131	1023		
44	311	88	619	132	1365		

Table 5.3 12 bit Target ID lookup table

AICON ID	DECODING ID	AICON ID	DECODING ID	AICON ID	DECODING ID	AICON ID	DECODING ID
1	129	45	359	89	605	133	839
2	135	46	363	90	615	134	843
3	139	47	371	91	621	135	845
4	141	48	383	92	629	136	851
5	147	49	387	93	639	137	853
6	149	50	389	94	645	138	863
7	153	51	393	95	649	139	867
8	159	52	399	96	655	140	869
9	163	53	401	97	657	141	879
10	165	54	407	98	663	142	887
11	169	55	411	99	667	143	891
12	175	56	413	100	669	144	893
13	177	57	417	101	679	145	903
14	183	58	423	102	683	146	907
15	187	59	427	103	685	147	909
16	189	60	429	104	691	148	915
17	195	61	435	105	693	149	917
18	197	62	437	106	697	150	921
19	201	63	441	107	703	151	927
20	207	64	447	108	711	152	931
21	209	65	455	109	715	153	933
22	215	66	459	110	717	154	937
23	219	67	461	111	723	155	943
24	221	68	467	112	725	156	945
25	225	69	469	113	729	157	951
26	231	70	473	114	735	158	955
27	235	71	479	115	739	159	957
28	237	72	483	116	741	160	965
29	243	73	485	117	745	161	969
30	245	74	489	118	751	162	975
31	249	75	495	119	753	163	977
32	255	76	497	120	759	164	983
33	263	77	503	121	763	165	987
34	267	78	507	122	765	166	989
35	275	79	509	123	783	167	999
36	287	80	533	124	791	168	1003
37	291	81	543	125	795	169	1005
38	303	82	549	126	797	170	1011
39	311	83	559	127	807	171	1013
40	315	84	567	128	811	172	1017
41	323	85	573	129	813	173	1023
42	335	86	581	130	819	174	1097
43	343	87	591	131	821	175	1103
44	347	88	599	132	831	176	1115

AICON ID	DECODING ID	AICON ID	DECODING ID	AICON ID	DECODING ID	AICON ID	DECODING ID
177	1117	221	1369	265	1647	309	1913
178	1131	222	1375	266	1655	310	1919
179	1133	223	1379	267	1659	311	1935
180	1145	224	1385	268	1661	312	1943
181	1151	225	1391	269	1677	313	1947
182	1161	226	1399	270	1683	314	1949
183	1167	227	1403	271	1685	315	1959
184	1175	228	1405	272	1689	316	1963
185	1179	229	1419	273	1695	317	1965
186	1181	230	1421	274	1701	318	1971
187	1191	231	1427	275	1705	319	1973
188	1195	232	1429	276	1711	320	1977
189	1197	233	1433	277	1719	321	1983
190	1203	234	1439	278	1723	322	1995
191	1205	235	1443	279	1725	323	1997
192	1209	236	1445	280	1737	324	2003
193	1215	237	1449	281	1743	325	2005
194	1223	238	1455	282	1751	326	2009
195	1227	239	1463	283	1755	327	2015
196	1229	240	1467	284	1757	328	2021
197	1235	241	1469	285	1767	329	2025
198	1237	242	1481	286	1771	330	2031
199	1241	243	1487	287	1773	331	2039
200	1247	244	1495	288	1779	332	2043
201	1251	245	1499	289	1781	333	2045
202	1253	246	1501	290	1785	334	2343
203	1257	247	1511	291	1791	335	2347
204	1263	248	1515	292	1823	336	2355
205	1271	249	1517	293	1829	337	2357
206	1275	250	1523	294	1833	338	2367
207	1277	251	1525	295	1839	339	2379
208	1303	252	1529	296	1847	340	2387
209	1307	253	1535	297	1851	341	2389
210	1309	254	1589	298	1853	342	2399
211	1319	255	1593	299	1865	343	2415
212	1323	256	1599	300	1871	344	2423
213	1325	257	1607	301	1879	345	2427
214	1331	258	1611	302	1883	346	2429
215	1337	259	1613	303	1885	347	2451
216	1343	260	1621	304	1895	348	2453
217	1351	261	1625	305	1899	349	2463
218	1355	262	1631	306	1901	350	2469
219	1357	263	1637	307	1907	351	2479
220	1363	264	1641	308	1909	352	2487

AICON ID	DECODING ID	AICON ID	DECODING ID	AICON ID	DECODING ID	AICON ID	DECODING ID
353	2491	397	2923	441	3485	485	5463
354	2493	398	2925	442	3495	486	5467
355	2511	399	2931	443	3499	487	5483
356	2519	400	2933	444	3501	488	5503
357	2523	401	2943	445	3509	489	5547
358	2525	402	2967	446	3519	490	5567
359	2535	403	2971	447	3541	491	5599
360	2539	404	2973	448	3551	492	5615
361	2541	405	2983	449	3567	493	5623
362	2547	406	2987	450	3575	494	5627
363	2549	407	2989	451	3579	495	5823
364	2559	408	2995	452	3581	496	5855
365	2643	409	2997	453	3701	497	5871
366	2645	410	3007	454	3711	498	5879
367	2655	411	3021	455	3741	499	5883
368	2671	412	3027	456	3755	500	5983
369	2679	413	3029	457	3757	501	5999
370	2683	414	3039	458	3765	502	6007
371	2685	415	3055	459	3775	503	6011
372	2709	416	3063	460	3797	504	6063
373	2719	417	3067	461	3807	505	6071
374	2735	418	3069	462	3823	506	6075
375	2743	419	3279	463	3831	507	6107
376	2747	420	3287	464	3835	508	6143
377	2749	421	3291	465	3837	509	7023
378	2767	422	3293	466	3903	510	7031
379	2775	423	3303	467	3925	511	7095
380	2779	424	3307	468	3935	512	7167
381	2781	425	3309	469	3951	513	7679
382	2791	426	3317	470	3959	514	7935
383	2795	427	3327	471	3963	515	8063
384	2797	428	3383	472	3965	516	8127
385	2803	429	3387	473	3999		
386	2805	430	3389	474	4015		
387	2815	431	3407	475	4023		
388	2863	432	3415	476	4027		
389	2871	433	3419	477	4029		
390	2875	434	3421	478	4055		
391	2877	435	3431	479	4059		
392	2895	436	3435	480	4061		
393	2903	437	3437	481	4075		
394	2907	438	3445	482	4077		
395	2909	439	3455	483	4085		
396	2919	440	3483	484	4095		

Table 5.4 14 bit Target ID lookup table

5.4. Uncoded targets correspondence

A link between the uncoded targets is important to be implemented in order to find the correspondence of these targets on every image. The uncoded targets are placed mostly on the fiducials from which the offset measurements with respect to the stretched wire are computed.

In close range photogrammetry and especially at CERN, uncoded targets are very common because they can be used on the fiducials. In various projects, there might be a group of encoded and uncoded targets (Photo 5.1), which should be identified and measured. Uncoded targets, have a disadvantage that they do not have code segments, thus it is not possible to find the homologous points in the way that it is done with the encoded targets, by decoding their code elements.
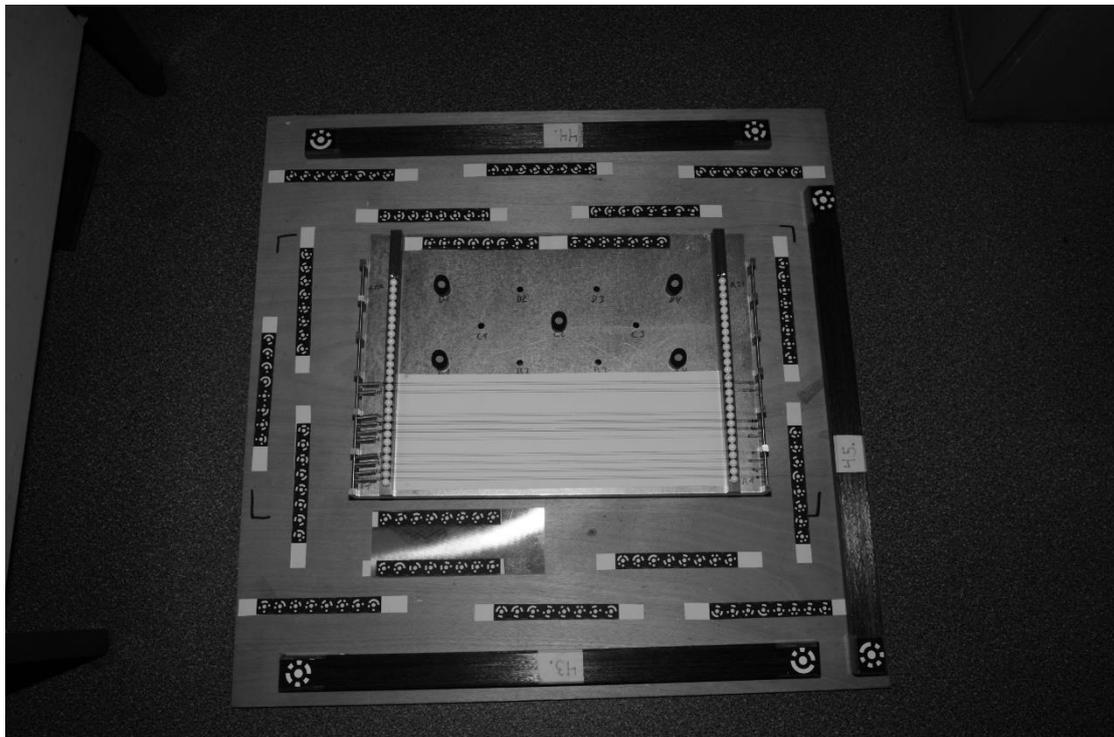
Photo 5.1 Encoded and uncoded targets on a project

Usually the uncoded targets have a rigid black body and on the top there is a white spot, which is the target. In the photo 5.2, three types of uncoded targets are presented. These targets have a base, which fits inside the fiducials sockets (Photo 5.3). They have a high resilience in time which is one of the factors they are preferred. These targets can be

precisely placed in the reference holes and the precision of the placement is ± 10 μm to ± 20 μm according to the manual.
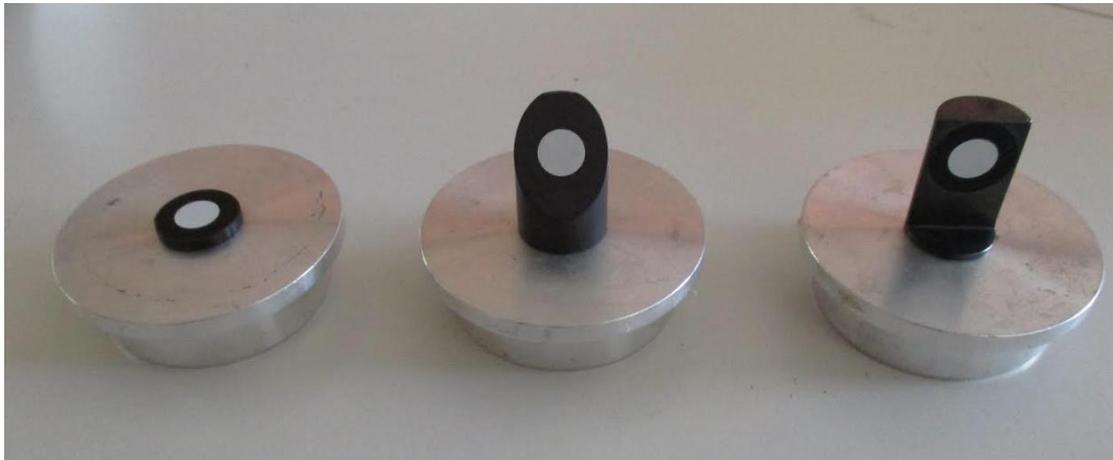
Photo 5.2 Uncoded targets
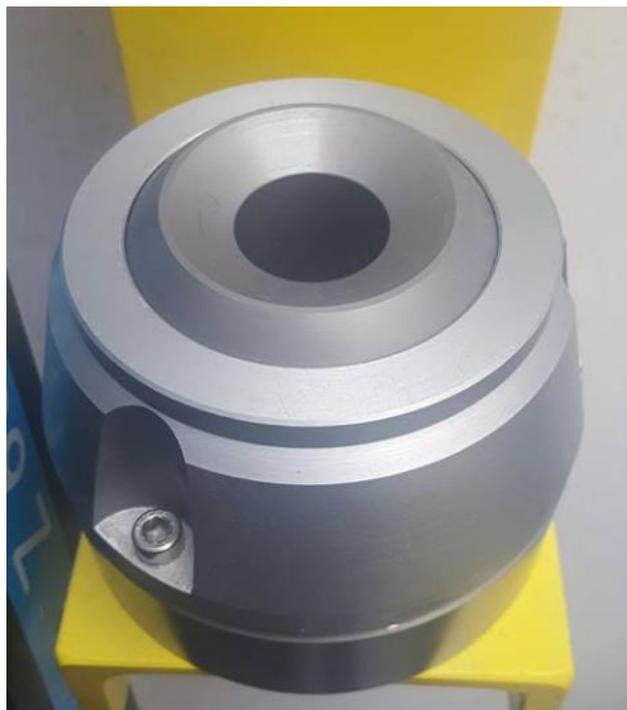
Photo 5.3 Components of a fiducial

5.4.1. The developed method to find the homologous points

The position of both uncoded targets and encoded targets should be determined on the image space and their coordinates should be calculated in the 3D space. In order to achieve that, there should be a

correspondence of each target, to find the homologous points on multiple images. The encoded targets achieve that thanks to their code, however the uncoded targets do not offer this possibility, hence a code should be given to them in order to include these targets in the bundle adjustment.

The first step that is required in order to start the process of finding the correspondence of the uncoded targets on the images is to calculate all the parameters of the interior and the exterior orientation. Hence, a project for the calibration of the camera should be done. Once the interior orientation is defined, the image coordinates of the targets should be corrected from distortion.

Since the exterior orientation is already determined from the calibration or the bundle adjustment of a project using encoded targets the process in order to find the homologous points of the non-coded targets can start. The following procedure and formulas can be applied for multiple images and non-coded targets, however for simplicity there will be a focus on just 2 images and one uncoded target.

After the iterative distortion correction is applied as it is mentioned in Chapter 2, the parameters of the exterior orientation $(X_o, Y_o, Z_o, \omega, \varphi, \kappa)$ for each image should be extracted from the bundle adjustment report.

Then the rotation matrices for the images should be constructed.

In this case, where there are only two images, there will be two rotation matrices, the R_L and R_R.

$$R = \begin{bmatrix} \cos\varphi\cos\kappa & \sin\omega\sin\varphi\cos\kappa + \cos\omega\sin\kappa & -\cos\omega\sin\varphi\cos\kappa + \sin\omega\sin\kappa \\ -\cos\varphi\sin\kappa & -\sin\omega\sin\varphi\sin\kappa + \cos\omega\cos\kappa & \cos\omega\sin\varphi\sin\kappa + \sin\omega\cos\kappa \\ \sin\varphi & -\sin\omega\cos\kappa & \cos\omega\cos\varphi \end{bmatrix} \quad (5.5)$$

Then the image coordinates of the points should be multiplied with the transposed rotation matrices (Ioannidis H. 2018).

$$\begin{pmatrix} x_L{'} \\ y_L{'} \\ -c_L \end{pmatrix} = R_L^T \begin{pmatrix} x_L \\ y_L \\ -c \end{pmatrix} \quad (5.6)$$

$$\begin{pmatrix} x_R{'} \\ y_R{'} \\ -c_R \end{pmatrix} = R_R^T \begin{pmatrix} x_R \\ y_R \\ -c \end{pmatrix} \quad (5.7)$$

Afterwards, the approximate object coordinates for the non-coded target will be:

$$Z = \frac{(X_{oR} - X_{oL}) \cdot (c_L \cdot c_R) - (x_L' \cdot c_R \cdot Z_{oL}) + (x_R' \cdot c_L \cdot Z_{oR})}{-x_L' \cdot c_R + x_R' \cdot c_L} \tag{5.8}$$

$$X = X_{oL} - x_L' \cdot \frac{Z - Z_{oL}}{c_L} \tag{5.9}$$

$$Y = Y_{oL} - y_L' \cdot \frac{Z - Z_{oL}}{c_L} \tag{5.10}$$

The indicators L an R means Left and Right.

The observation equations are the collinearity equations.

$$x - x_o = -c\frac{R_{11}(X - X_o) + R_{12}(Y - Y_o) + R_{13}(Z - Z_o)}{R_{31}(X - X_o) + R_{32}(Y - Y_o) + R_{33}(Z - Z_o)} \tag{5.11}$$

$$y - y_o = -c\frac{R_{21}(X - X_o) + R_{22}(Y - Y_o) + R_{23}(Z - Z_o)}{R_{31}(X - X_o) + R_{32}(Y - Y_o) + R_{33}(Z - Z_o)} \tag{5.12}$$

$$Fx = x - x_o, Fy = y - y_o$$

Hence for the two images

$$U_L = R_{L11}(X - X_{oL}) + R_{L12}(Y - Y_{oL}) + R_{L13}(Z - Z_{oL}) \tag{5.13}$$

$$V_L = R_{L21}(X - X_{oL}) + R_{L22}(Y - Y_{oL}) + R_{L23}(Z - Z_{oL}) \tag{5.14}$$

$$W_L = R_{L31}(X - X_{oL}) + R_{L32}(Y - Y_{oL}) + R_{L33}(Z - Z_{oL}) \tag{5.15}$$

$$U_R = R_{R11}(X - X_{oR}) + R_{L12}(Y - Y_{oR}) + R_{L13}(Z - Z_{oR}) \tag{5.16}$$

$$V_R = R_{R21}(X - X_{oR}) + R_{L22}(Y - Y_{oR}) + R_{L23}(Z - Z_{oR}) \tag{5.17}$$

$$W_R = R_{R31}(X - X_{oR}) + R_{L32}(Y - Y_{oR}) + R_{L33}(Z - Z_{oR}) \tag{5.18}$$

The design matrix A will have the following elements

$$A_{11} = -c\left(\frac{R_{11}}{W_L} - R_{31}\frac{U_L}{W_L^2}\right) \tag{5.19}$$

$$A_{12} = -c\left(\frac{R_{12}}{W_L} - R_{32}\frac{U_L}{W_L^2}\right) \tag{5.20}$$

$$A_{13} = -c\left(\frac{R_{13}}{W_L} - R_{33}\frac{U_L}{W_L^2}\right) \tag{5.21}$$

$$A_{21} = -c\left(\frac{R_{21}}{W_L} - R_{31}\frac{V_L}{W_L^2}\right) \tag{5.22}$$

108

$$A_{22} = -c \left(\frac{R_{22}}{W_L} - R_{32} \frac{V_L}{W_L^2} \right) \tag{5.23}$$

$$A_{23} = -c \left(\frac{R_{23}}{W_L} - R_{33} \frac{V_L}{W_L^2} \right) \tag{5.24}$$

$$A_{31} = -c \left(\frac{R_{11}}{W_R} - R_{31} \frac{U_R}{W_R^2} \right) \tag{5.25}$$

$$A_{32} = -c \left(\frac{R_{12}}{W_R} - R_{32} \frac{U_L}{W_R^2} \right) \tag{5.26}$$

$$A_{33} = -c \left(\frac{R_{13}}{W_R} - R_{33} \frac{U_L}{W_R^2} \right) \tag{5.27}$$

$$A_{41} = -c \left(\frac{R_{21}}{W_R} - R_{31} \frac{V_L}{W_R^2} \right) \tag{5.28}$$

$$A_{42} = -c \left(\frac{R_{22}}{W_R} - R_{32} \frac{V_L}{W_R^2} \right) \tag{5.29}$$

$$A_{43} = -c \left(\frac{R_{23}}{W_R} - R_{33} \frac{V_L}{W_R^2} \right) \tag{5.30}$$

$$A = \begin{bmatrix} A_{11} & A_{12} & A_{13} \\ A_{21} & A_{22} & A_{23} \\ A_{31} & A_{32} & A_{33} \\ A_{41} & A_{42} & A_{43} \end{bmatrix} \tag{5.31}$$

The matrix $\delta\lambda$ will be:

$$\delta\lambda = \begin{pmatrix} x_L - F_{xL} \\ y_L - F_{yL} \\ x_R - F_{xR} \\ y_L - F_{yR} \end{pmatrix} \tag{5.32}$$

Where (x_L, y_L) and (x_R, y_R) are the image coordinates of the point on the left and right image (Ioannidis H. 2018).

$$N = A^T A \tag{5.33}$$

$$u = A^T \delta\lambda \tag{5.34}$$

$$\hat{x} = N^{-1} u \tag{5.35}$$

$$\hat{x} = \begin{bmatrix} \delta X \\ \delta Y \\ \delta Z \end{bmatrix} \tag{5.36}$$

Then the object space coordinates of the target are going to be:

$$\begin{bmatrix} X' \\ Y' \\ Z' \end{bmatrix} = \begin{bmatrix} X \\ Y \\ Z \end{bmatrix} + \begin{bmatrix} \delta X \\ \delta Y \\ \delta Z \end{bmatrix} \tag{5.37}$$

This procedure continues until the vector $\hat{x}$ reaches a minimum value that the user provides.

After the calculation of the final coordinates, the variance and covariance V_x matrix should be computed in order to determine the precision of the intersection.

$$v = A\hat{x} - \delta l \tag{5.38}$$

$$\sigma_o = \sqrt{\frac{[v^T v]}{n - m}} \tag{5.39}$$

$$V_x = \sigma_o N^{-1} \tag{5.40}$$

Thus, the standard deviations σX, σY, σZ of the spatial coordinates can be calculated. If the standard deviations that came as results of the intersection (Fig. 5.4) have values smaller than the value the user has set (for most cases 50 μm), the points that were targeted are the same and they are homologous, hence a number can be assigned for these targets. If the standard deviations have big values then the intersection is not precise. This means that the points were not correspondent and they should not have the same number because they are different targets.

By this method, homologous points can be found with reliability.
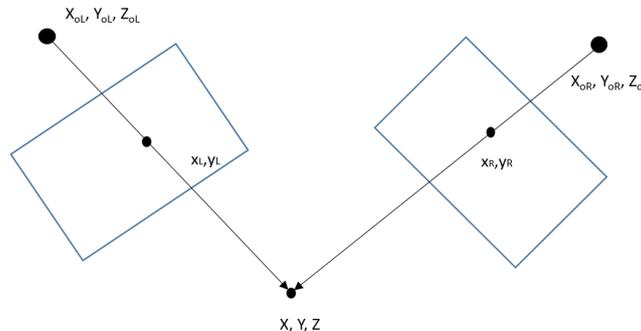
Figure 5.4 Intersection

110

Chapter 6

LGC & LGC2 SOFTWARE

6.1. LGC

LGC is a surveying software that has been developed at CERN. This software enables a survey measurement network to be analyzed and processed in three different ways:

- Processing of the observed measurements through a least squares algorithm for the calculation of the unknown coordinates of the network and other additional unknown parameters such as instrument highs, total station orientations and measurement constants.
- Error detection process for the observed measurements, where the unknown parameters such as the instrument heights and total station orientations are calculated.
- A simulation of a given network configuration.

A least squares solution requires that sufficient constraints are included in the network so that the process will converge. The position orientation and scale of the network need to be fixed. This is possible by introducing points which have fixed positions or distances. An alternative is to make a free network adjustment (CERN LGC 2018).

Due to the fact that new equipment and sensors were integrated at CERN so as to allow a larger field of applications and measurements such as the unlevelled polar measurement with the laser tracker, the LGC program was upgraded in order to cover the needs for the processing of the measurements and to include the new instruments.

At the LGC2, UVEC and UVD observations can be used for measurements by camera (Fig. 6.1). A ray which passes from the chip of the camera, the center of projection and the target itself can be converted in a unit vector, u, with u=(i,j,k) representing the direction of the measurements. To express this kind of observation,

- UVD, Unit Vector with a distance
- UVEC, Unit VECtor, as a simplification of UVD

have been defined.
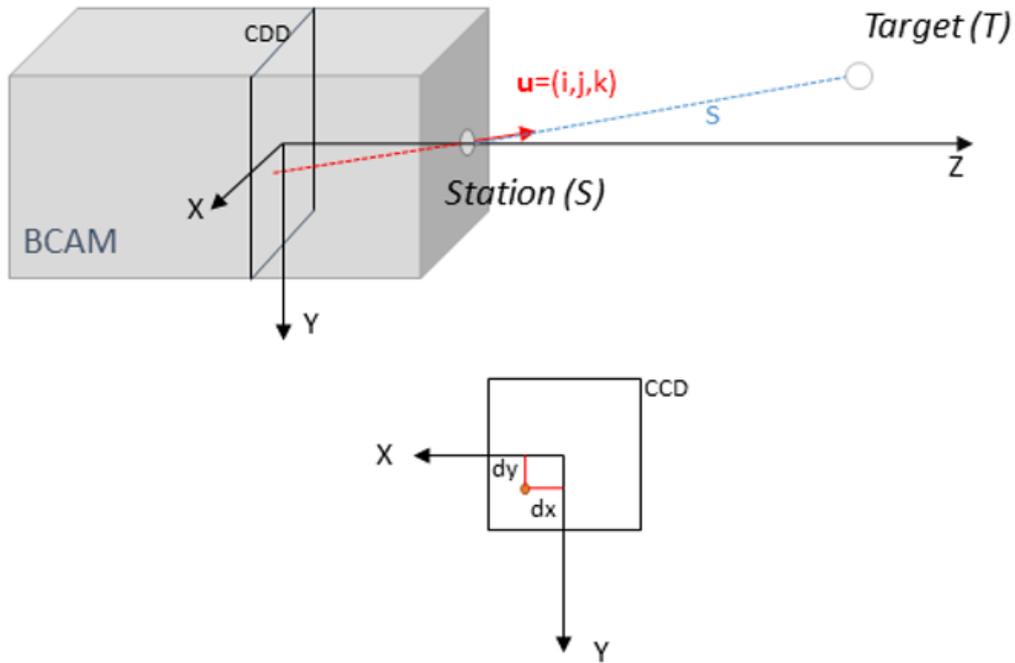
Figure 6.1 Camera representation (Barbier M. 2016)

The corresponding equations for UVD and UVEC are respectively:

$$s \begin{pmatrix} i \\ j \\ k \end{pmatrix} - \begin{pmatrix} X_T - X_S \\ Y_T - Y_S \\ Z_{T-}Z_S \end{pmatrix} = 0 \tag{6.1}$$

$$\begin{pmatrix} i \\ j \end{pmatrix} - \frac{k}{Z_T - Z_S} \cdot \begin{pmatrix} X_T - X_S \\ Y_T - Y_S \end{pmatrix} = 0 \tag{6.2}$$

Where *s* is the distance between the lens of the BCAM (considered as a measuring station) and the target (Barbier M. 2016). BCAM is a camera looking at one or more light sources.

6.2. LGC2

The new version of LGC, the LGC2 is improved in many ways from the previous version. Not only does it offer a better maintainability, but also a stack of local Cartesian frames can be introduced for observations and

112

parameters. It is also able to take more parameters and instruments into account. All these newly introduced features increase the complexity of the input file, however the new data provides a better control of the error propagation and provide more sophisticated setups using local frames (Fig. 6.2) (LGC2 User Guide 2018).
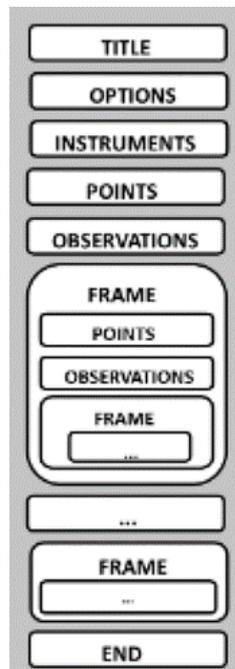
Figure 6.2 General file layout (LGC2 User Guide 2018)

Two of the new features introduced in the LGC2software are the creation of frames and the introduction of a new type of observations.

The new type of observations such as PLR3D (Fig. 6.3), ANGL, ZEND and DIST provide the ability to combine a horizontal angle, a zenith distance (vertical angle) and a spatial distance. The values typically come from a laser tracker or total station and can offer a better contribution to the adjustment when they are supplied together.

Stacking local Cartesian frames (FRAME) in the configuration is a major new feature of the LGC2. A FRAME contains points and measurements like the UVEC, UVD, PLR3D, ANGL, ZEND, DIST and even further frames. Each FRAME section that opens must be closed by the keyword ENDFRAME. A frame is for example useful to create a group of points that can only move together. The points must be declared using the CALA keyword inside the frame declaration to achieve a moving point group. A frame is defined by three translations relative to its parent frame, three rotations and a scale factor.

113

By default, a frame is fixed, the rotations around the axes may be enabled by adding the RX, RY and RZ flags, translations are enabled by the TX, TY and TZ flags and scale by SCL flag.

The transformations into a frame is done by using the rotation matrix $R_{xyz} = R_x \cdot R_y \cdot R_z$, where firstly rotation about Z axis is applied, followed by a rotation about Y axis, and ending with a rotation about the X axis.

A typical input file for the LGC2 which includes measurements for target points and for a wire is presented on photo 6.1.
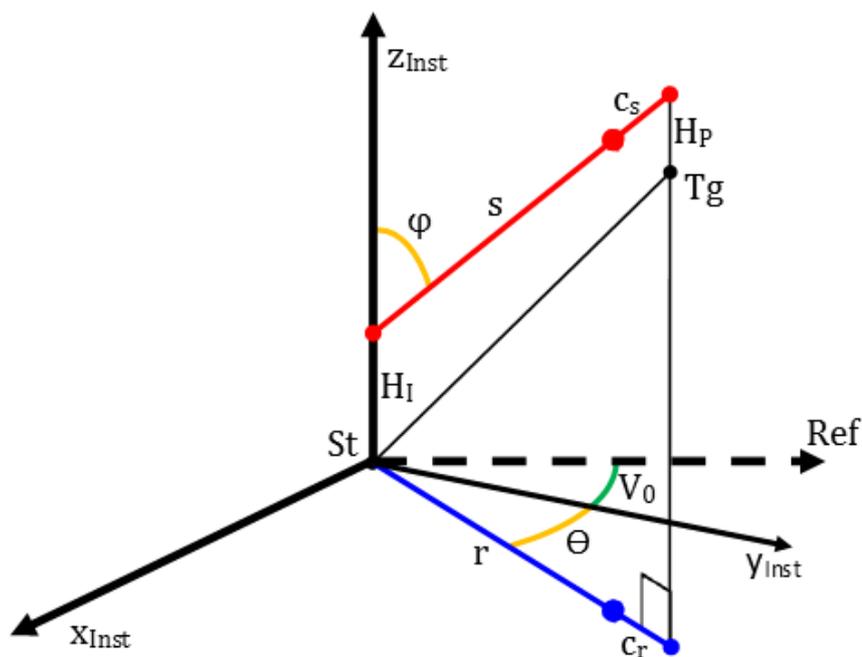
Figure 6.3 PLR3D observation (LGC2 User Guide 2018)

```
*TITR
MEASUREMENTS
*OLOC
*PUNC    T
*PREC 7
*FAUT
*INSTR
*CAMD    TS1    TGT1    0.0
TGT1    0.008    0.008    0.1    0
TWIRE   0.005    0.005    0.1    0
*CAMD    WIRESIM    TGT_WIRE    0.0
TGT_WIRE    0.00001    0.00001    0.00001    0.005
*POIN
10005        0.9607291        0.5309268        -0.0566531
10006        1.0609921        0.4351970        -0.0072686
10007        0.9692596        0.0447912         0.1487603
10012        0.8780961       -0.3353053         0.3276910
%   Photo 11
%-----------------------
*FRAME    PHOT11    0.2534995   -0.9375629    0.6188366  -48.4362534   19.5315831    7.8889356   1
%-----------------------
*CALA
PHOTO11        0         0         0
*CAM PHOTO11 TS1
*UVEC
10005    0.0822147080    0.3516868564    -0.9325004540
10006    0.1605658525    0.3512515719    -0.9224103969
10007    0.2487704121    0.3305020071    -0.9104294071
10012    0.4087562368    0.3101381192    -0.8583313381
WP21   -0.5308888570    0.1006504418    -0.8414431116 TRGT TWIRE
WP22    0.5199494162    0.1729422885    -0.8365067659 TRGT TWIRE
*ENDFRAME
%   Photo 19
%-----------------------
*FRAME    PHOT19    0.5255377   -0.5005894    1.1782740  -19.7765022   10.2030936    1.4736233   1
%-----------------------
*CALA
PHOTO19        0         0         0
*CAM PHOTO19 TS1
*UVEC
10005    0.1065476000    0.3653115486    -0.9247675824
10006    0.1812701125    0.3341423217    -0.9249270540
10007    0.2007060593    0.1687942552    -0.9650002990
10012    0.2277664984   -0.1044449506    -0.9680979674
WP37   -0.5319791481   -0.0778493999    -0.8431711908 TRGT TWIRE
WP38    0.5276486318   -0.0310940921    -0.8488934438 TRGT TWIRE
*ENDFRAME
%   Photo 26
%-----------------------
*FRAME    PHOT26    0.8588928   -0.4882243    1.1769590  -21.9928315    1.4077223    1.9672258   1
%-----------------------
*CALA
PHOTO26        0         0         0
*CAM PHOTO26 TS1
*UVEC
10005    0.0322810043    0.3386920639    -0.9403433536
10006    0.1029311442    0.3120927632    -0.9444592563
10007    0.0688973018    0.1339957389    -0.9885839892
10012    0.0056040603   -0.1663969462    -0.9860429254
WP51   -0.5300556529   -0.1150442374    -0.8401225079 TRGT TWIRE
WP52    0.5266449754   -0.0690203589    -0.8472787380 TRGT TWIRE
*FRAME    WIRE   -0.3324187   -0.2426877    0.1039539    0.0000000 100.0000000    0.0000000   1
*FRAME    WIRE2   0.0000000    0.0000000    0.0000000 399.0716766 399.1051275 351.1680598   1
*CALA
WP0       0.0000000        0.0000000        0.0000000
*POIN
WP21       0.0000000        0.0000000       -0.3739147
WP22       0.0000000        0.0000000       -1.6525815
WP37       0.0000000        0.0000000       -0.3841150
WP38       0.0000000        0.0000000       -1.8448298
WP51       0.0000000        0.0000000       -0.5253490
WP52       0.0000000        0.0000000       -1.9244534
*FRAME  WIREM  0.0000000    0.0000000   -0.8227623    0.0000000    0.0000000    0.0000000   1    TX TY RX RY
*CALA
WPM       0.0000000        0.0000000        0.0000000
Fiducial     0.0000000    0.0000000   -0.4836593 % 10005
ProjectPoint2      0.0000000    0.0000000   -0.5818114 % 10006
FiducialBar      0.0000000    0.0000000   -0.4822111 % 10007
ProjectPoint4      0.0000000    0.0000000   -0.3830086 % 10012
*CAM   WPM   WIRESIM
*UVEC
WP21       0.0000000        0.0000000       -1.0000000
WP22       0.0000000        0.0000000        1.0000000
WP37       0.0000000        0.0000000       -1.0000000
WP38       0.0000000        0.0000000        1.0000000
WP51       0.0000000        0.0000000       -1.0000000
WP52       0.0000000        0.0000000        1.0000000
*ENDFRAME
*ENDFRAME
*ENDFRAME
*END
```

Photo 6.1 LGC2 input file

6.3.   Input data

Each observation type requires its own data preparation and processing. Hence, for instance the UVEC needs different type of data treatment than the ANGL and ZEND. Furthermore, in order to be able to prepare the data concerning the wire to be used for LGC2, several calculations should be done. All data preparations and the calculations required for target points and the wire are presented on this section.

6.3.1. ANGL and ZEND

One type of observations that can be used for the target points are the ANGL and the ZEND (Fig. 6.4 & Fig. 6.5). ANGL is a standard horizontal angle measurement (φ) while the ZEND is the Zenith distance (vertical angle) measurements (θ). Before the calculation of the vertical and horizontal angle, the image coordinates should be corrected from distortion.
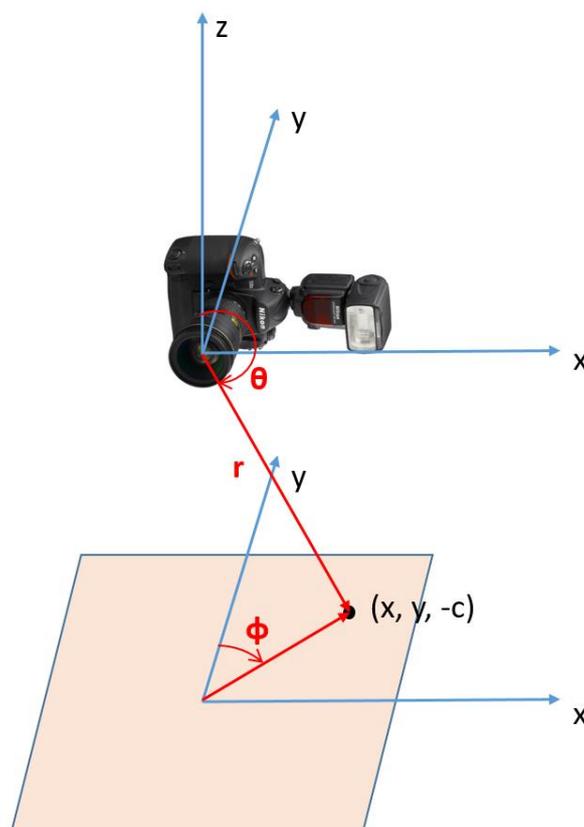
Figure 6.4 ANGL and ZEND observations

Once the correction is applied then the angles can be computed by the following formulas (Spherical Coordinates Wolfram 2018):

$$r = \sqrt{x^2 + y^2 + z^2} \qquad (6.3)$$

$$\theta = arccos\left(\frac{z}{r}\right) \qquad (6.4)$$

$$\varphi = \frac{\pi}{2} - atan2\left(\frac{y}{x}\right) \qquad (6.5)$$

As for the approximate object coordinates of the targets, they can be extracted from the bundle adjustment report for the encoded targets and for the uncoded targets, they can be taken from the 3D intersections that are performed in order to find the homologous points, as it is described in the chapter 5.
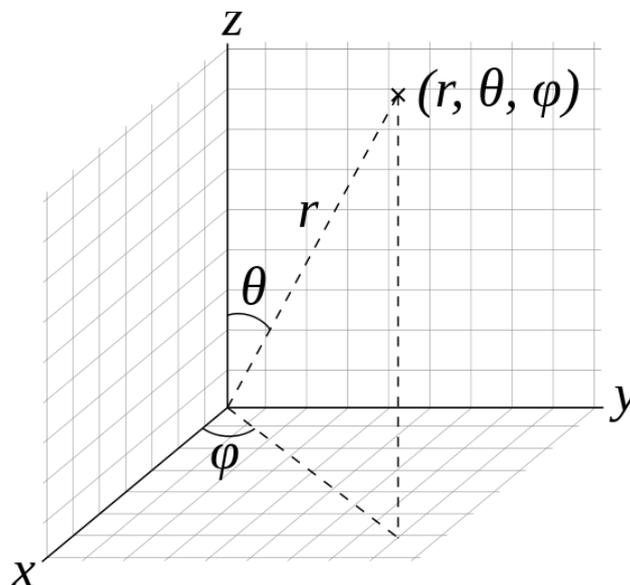
Figure 6.5 Spherical coordinates (r, θ, φ): radial distance r, polar angle θ (theta), and azimuthal angle φ (phi). The symbol ρ (rho) is often used instead of r
(wikipedia.org/wiki/Spherical_coordinate_system)

6.3.2. UVEC

The other type of observations that can be used is the UVEC. UVEC is the measurement of a spatial direction vector made by a camera, therefore the expected vector is a unity vector. The unity vectors are defined by the following formulas:

$$r = \sqrt{x^2 + y^2 + z^2} \qquad (6.6)$$

$$i = \frac{x}{r} \qquad (6.7)$$

$$j = \frac{y}{r} \qquad (6.8)$$

$$k = \frac{z}{r} \qquad (6.9)$$

6.3.3. Stretched wire

Just a part of the entire wire is visible on each image. Hence, from the algorithm that has been developed by Lucie Scandella (Scandella L. 2017), it is possible to extract the image coordinates of the first and the last point of the wire on each image. Thus, if a segment of the wire has been captured by 4 images then from the algorithm, 8 different points can be extracted. All these points in the 3D space should correspond to points on a straight line. However, it should be mentioned that the stretched wire has a small sag, which can be illustrated at the figure 6.7.

Nevertheless, it can be assumed that for small parts of 2-3 meters of the wire that are captured with the camera, the points are on a straight line, since the sag is minimal for these lengths. This assumption holds since a 125 m long wire stretched along ATLAS experiment has a deviation of only 0.04 mm in its central part from the straight line (Quesnel J. 2008).

In order to find these points and to determine their approximate 3D coordinates in the object space in order to be input at the LGC2 file, a specific procedure should be followed.
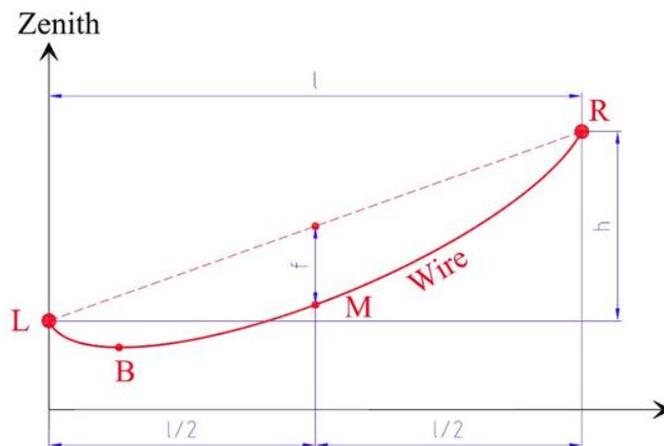
Figure 6.6 Sag of the wire (Touzé T. 2007)

The first step is the correction of the distortion for the image coordinates. The next step is to perform a rotation and translation of the image coordinates from the image space to the object space. The rotation should be applied by the rotation matrix $R_{xyz} = R_x \cdot R_y \cdot R_z$, where R_x, R_y, R_z are equal to (Rotation Matrix Wolfram 2018):

$$R_x = \begin{bmatrix} 1 & 0 & 0 \\ 0 & cos\omega & sin\omega \\ 0 & -sin\omega & cos\omega \end{bmatrix} \tag{6.10}$$

$$R_y = \begin{bmatrix} cos\varphi & 0 & -sin\varphi \\ 0 & 1 & 0 \\ sin\varphi & 0 & cos\varphi \end{bmatrix} \tag{6.11}$$

$$R_z = \begin{bmatrix} cos\kappa & sin\kappa & 0 \\ -sin\kappa & cos\kappa & 0 \\ 0 & 0 & 1 \end{bmatrix} \tag{6.12}$$

It should be mentioned that the ω, φ, κ used by the algorithm, have the opposite sign of the ω, φ, κ that are exported from the bundle adjustment report, but they have the same absolute value. Once the rotations and translations are done, for each image, 3 points in the spatial coordinate system will be available. These are the projection center of the camera, which is already determined by the exterior orientation and the two points of the wire. Three points are required in order to create a plane. For instance, let us suppose that P_1 (X_1, Y_1, Z_1) is the projection center in the object space and P_2 (X_2, Y_2, Z_2) and P_3 (X_3, Y_3, Z_3) are the image points which correspond to the wire that has been translated and rotated to be in the object space. From these three points the following vectors can be created.

$$\overrightarrow{P_1P_2} = \left(X_2 - X_1, Y_2 - Y_1, Z_2 - Z_1 \right) = (DX_{12}, DY_{12}, DZ_{12}) \tag{6.13}$$

$$\overrightarrow{P_1P_3} = \left(X_3 - X_1, Y_3 - Y_1, Z_3 - Z_1 \right) = (DX_{13}, DY_{13}, DZ_{13}) \tag{6.14}$$

Then the normal is computed as:

$$n = \overrightarrow{P_1P_2} \times \overrightarrow{P_1P_3} = \begin{vmatrix} i & j & k \\ DX_{12} & DY_{12} & DZ_{12} \\ DX_{13} & DY_{13} & DZ_{13} \end{vmatrix} = ai + bj + cj \tag{6.15}$$

The function of a plane is:

$$plane = (a, b, c) \cdot [(x, y, z) - (x_o, y_o, z_o)] \tag{6.16}$$

$$plane = ax + by + cz + d = 0 \tag{6.17}$$

Where (x_o, y_o, z_o) the coordinates of a known point, for instance the P$_1$.

This procedure will be carried out for all the photos in order to determine all the planes. Once the equations of the planes are determined, the combination of the two planes which have an intersection angle closer to 90º will be chosen to determine the intersection line (Fig. 6.7). The angle between the two planes is given by the following formula, where n is the normal vector of the plane (Dawkins P. 2018).

$$\theta = \arccos\left(\frac{n_i \cdot n_j}{|n_i| \cdot |n_j|}\right) \tag{6.18}$$

Once the intersection of planes is determined, the line of the intersection is determined from the solution of the equations of the planes.

The solution has the following form:

$$y = A \cdot z + B \tag{6.19}$$

$$x = C \cdot z + D \tag{6.20}$$
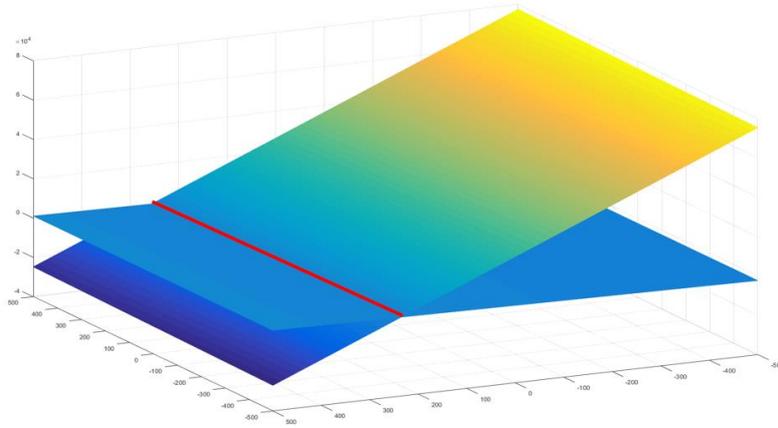
Figure 6.7 Plane intersection and the intersection line

The final step in order to determine the approximate spatial coordinates for the wire is to intersect the line that has been determined from the intersection of planes with the rays that pass from the projection center of the camera to the image points that correspond to the wire which have been rotated and translated as it has been mentioned previously (Fig. 6.8).

From the equations 6.19 and 6.20 if a value is assigned to the variable z, then a point will be created. For instance, if z=0, the coordinates of a point on the intersection line will be (D, B, 0). Hence, two points are

required on the intersection line in order to create a vector. Once the vector is created the equation of the line will be:

$$r = c + t\vec{V}, \ \ t \in R \tag{6.21}$$

where c is a point on the line and $\vec{V}$ is the vector created by two points on the line. Both the intersection line and the ray will have an equation like this. Finally, from the solution of the equations, the outcome will be a point on the wire on the spatial coordinate system.
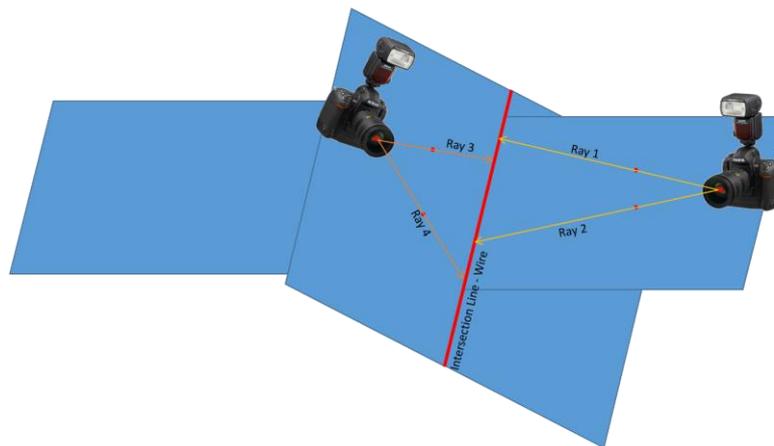
Figure 6.8 Intersection of rays with the intersection line

Depending if the observations that are going to be used are ANGL and ZEND or UVEC, the image coordinates can be converted to the corresponding observation type as it has been mentioned on 6.3.1 and 6.3.2.

6.3.4. FRAME

As it has been mentioned, a FRAME section is a logical block that can contain points and measurements. Each photo or camera, which is going to be input in the LGC2, has its own frame. An example for a frame is the one below:

```
*FRAME   PHOT11   0.2534995  -0.9375629   0.6188366 -48.4362534  19.5315831   7.8889356  1
```

The first parameter after the keyword *FRAME, is the name of the frame, the second, the third and the fourth are the X Y Z coordinates of the projection center of the camera in meters, the fifth the sixth and seventh

parameters are the rotations ω, φ, κ in gons, where these rotations have the opposite sign from the ones that are extracted from AICON, and the last parameter is the scale which usually is set equal to 1.

Whenever a photo has a rotation κ between -150 and -50 gons, an additional FRAME should be created as the one below, where X, Y, Z, ω, φ are equal to 0 and the rotation κ will be assigned equal to 100. This manipulation is done, in order to avoid some numerical problems that are present at the LGC2 which is currently under development.

```
%   Photo 3
%----------------------
*FRAME    PHOT3    -0.1797859   -0.7054912    0.9221013  -35.6710371   24.0680554  -95.7469899  1
*FRAME    PHOTB3    0.0000000    0.0000000    0.0000000    0.0000000    0.0000000  100.0000000  1
%----------------------
```

At this case, the observation sequence is not going to be i, j, k, but –j, i, k.

Also, whenever a photo has a rotation κ between 50 and 150 gons an additional FRAME should be created as the one below, where X, Y, Z, ω, φ are equal to 0 and the rotation κ will be assigned equal to -100.

```
%   Photo 9
%----------------------
*FRAME    PHOT9     0.1034109   -0.6963675    0.9117177  -36.5689670   10.4063835  102.2029185  1
*FRAME    PHOTB9    0.0000000    0.0000000    0.0000000    0.0000000    0.0000000 -100.0000000  1
%----------------------
```

In this case the observation sequence is not going to be i, j, k, but j, -i, k.

At the end of each frame, *ENDFRAME should be added in order to close the frame.

The wire itself should also have its own FRAME. In order to implement this the following procedure should be followed.

First of all, from two points on the wire in 3D, the *DX*, *DY* and *DZ* should be calculated.

After that, the following values ω, φ and κ should be calculated.

$$\omega = \arctan\left(\frac{DZ}{DY}\right) \tag{6.22}$$

$$\varphi = \arctan\left(\frac{DZ}{DX}\right) \tag{6.23}$$

$$\kappa = \arctan\left(\frac{DX}{DY}\right) \tag{6.24}$$

If *DY* is equal to 0 then the ω and κ are going to be calculated as below:

$$\omega = \text{acot}\left(\frac{DY}{DZ}\right) \tag{6.25}$$

$$\kappa = \arctan\left(\frac{DY}{DX}\right) \tag{6.26}$$

If the *DX* is equal to 0 then the φ is going to be calculated as below:

$$\varphi = \arctan\left(\frac{DX}{DZ}\right) \tag{6.27}$$

After the calculation of these parameters the first FRAME should be created. The parameters for the first FRAME are going to be the 3D coordinates of a point on the wire, which for instance could be the first point in the list of points on the wire, and only the rotation that corresponds to φ will be equal to 100 gons while the rest are going to be equal to 0.

After that, an additional FRAME will be created, where the X, Y, Z are going to be equal to 0 and the rotations that are going to be input will be κ-100, φ, ω. The variables ω, φ, κ have been calculated from the formulas 6.22, 6.23 and 6.24.

```
*FRAME    WIRE   -0.3324187  -0.2426877   0.1039539   0.0000000 100.0000000   0.0000000  1
*FRAME    WIRE2   0.0000000   0.0000000   0.0000000 399.0716766 399.1051275 351.1680598  1
```

After this, the observations for the wire using UVEC will have on i and j values equal to 0 and on k will be assigned the 3D distance of each point from the point that was set as the origin of the first FRAME for the wire.

```
*FRAME    WIRE   -0.3324187  -0.2426877   0.1039539   0.0000000 100.0000000   0.0000000  1
*FRAME    WIRE2   0.0000000   0.0000000   0.0000000 399.0716766 399.1051275 351.1680598  1
*CALA
WP0       0.0000000        0.0000000        0.0000000
*POIN
WP1       0.0000000        0.0000000        0.0000001
WP2       0.0000000        0.0000000       -1.9598912
WP3       0.0000000        0.0000000       -0.0307238
WP4       0.0000000        0.0000000       -1.8551996
WP7       0.0000000        0.0000000       -0.1688453
WP8       0.0000000        0.0000000       -1.7045279
WP9       0.0000000        0.0000000       -0.1704930
WP10      0.0000000        0.0000000       -1.6128098
WP11      0.0000000        0.0000000       -0.1785972
```

Finally, one more FRAME should be added, whose parameters are all going to be zero except the value of Z which will be the average value of all distances of the wire points that are calculated with respect to the first point. The observations in this FRAME have values on the k component only, which are either 1 or -1, where -1 is set when a point is on the left of the middle point of the wire and 1 when a point is on the right of the middle point of the wire.

```
*FRAME  WIREM  0.0000000    0.0000000   -0.8227623    0.0000000    0.0000000    0.0000000  1   TX TY RX
*CALA
WPM        0.0000000        0.0000000        0.0000000
Fiducial       0.0000000    0.0000000  -0.4836593 % 10005
ProjectPoint2     0.0000000    0.0000000  -0.5818114 % 10006
FiducialBar    0.0000000    0.0000000  -0.4822111 % 10007
ProjectPoint4     0.0000000    0.0000000  -0.3830086 % 10012
*CAM   WPM   WIRESIM
*UVEC
WP1        0.0000000        0.0000000       -1.0000000
WP2        0.0000000        0.0000000        1.0000000
WP3        0.0000000        0.0000000       -1.0000000
WP4        0.0000000        0.0000000        1.0000000
WP7        0.0000000        0.0000000       -1.0000000
WP8        0.0000000        0.0000000        1.0000000
WP9        0.0000000        0.0000000       -1.0000000
WP10       0.0000000        0.0000000        1.0000000
WP11       0.0000000        0.0000000       -1.0000000
WP12       0.0000000        0.0000000        1.0000000
WP13       0.0000000        0.0000000       -1.0000000
WP14       0.0000000        0.0000000        1.0000000
WP15       0.0000000        0.0000000       -1.0000000
WP16       0.0000000        0.0000000        1.0000000
```

At the end of the LGC2 file three *ENDFRAME keywords should be added in order to close these three FRAMES for the wire and also *END keyword should be added, to indicate the end of the LGC2 file.

```
WP54       0.0000000        0.0000000        1.0000000
WP55       0.0000000        0.0000000       -1.0000000
WP56       0.0000000        0.0000000        1.0000000
WP57       0.0000000        0.0000000       -1.0000000
WP58       0.0000000        0.0000000        1.0000000
WP63       0.0000000        0.0000000       -1.0000000
WP64       0.0000000        0.0000000        1.0000000
WP65       0.0000000        0.0000000       -1.0000000
WP66       0.0000000        0.0000000        1.0000000
WP71       0.0000000        0.0000000       -1.0000000
WP72       0.0000000        0.0000000        1.0000000
WP73       0.0000000        0.0000000       -1.0000000
WP74       0.0000000        0.0000000        1.0000000
*ENDFRAME
*ENDFRAME
*ENDFRAME
*END
```

6.4.   LGC2 and AICON comparison

Both AICON and LGC2 software are able to do adjustments and to provide results for the measurements that are input. In this section, the comparison of the results that are provided by both software for a project (LHC mockup – project 3) are going to be analyzed, in order to prove that both software packages provide equivalent results.

In LGC2 there is the option to put the input points free and calculate their 3D coordinates again. Figure 6.9 presents that the coordinates of points that are calculated from AICON and from LGC2 are practically the same, since on the object space the differences DX, DY, DZ have values which do not exceed 1 μm. These small differences might be present due to slightly different mathematical model and approach that these software programs use.

Furthermore, another indication that everything is correctly calculated is when the target points are totally constrained and set as fixed points using the keyword CALA and the positions of the photos (projection centers) are set free. In this way the differences among the parameters of exterior orientation for each image can be calculated.

The average differences of translations and rotations are presented on table 6.1:

DTX	1μm
DTY	0μm
DTZ	1μm
Dω	-0.06 cc
Dφ	-0.32 cc
Dκ	0.06 cc gon

Table 6.1 Differences of translations and rotations between fixed and free camera frame for the LHC mockup project

The values on table 6.1 are very small, and this means that the calculated translations and rotations from AICON and the from LGC2 are identical and the algorithm provides equivalent results. The differences of Dω, Dφ, Dκ for 1 m distance are respectively -0.09 μm, -0.50 μm, 0.09 μm.
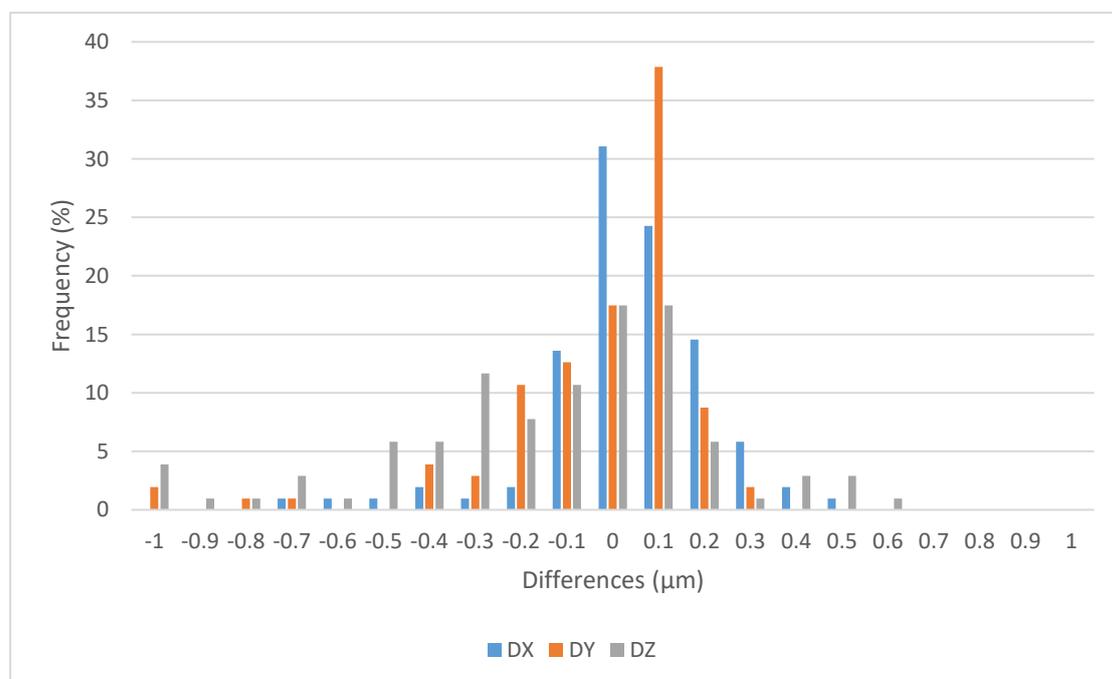
Figure 6.9 Differences between AICON and LGC2 computed object coordinates on X, Y, Z component

Chapter 7

OFFSET CALCULATION WITH RESPECT TO STRETCHED WIRE AT LHC

7.1. Measurement projects at the LHC

After the development of the algorithm for the target detection, position determination, decoding and the integration of the results from the developed algorithm to measure stretched wires, there is enough data in order to proceed to computing the offset distance from each fiducial with respect to the stretched wire. Offset measurements with respect to stretched wires are used for accelerator alignments at CERN.

In order to start such a calculation, several projects took place on July 19, 2018 at a small part of the LHC accelerator, where targets and a stretched wire were installed (Photo 7.1). The role of the encoded targets is for the calibration and the determination the of the interior and of exterior orientation. On the other hand, the fiducials whose 3D position should be determined and the stretched wire, are the data that take part at the offset measurement.

Each project consisted of approximately 30-35 photos with a regular geometry to cover the area (Fig. 7.1). The coverage of the camera positions as depicted in figure 7.1 had been chosen in such a way to have ensure geometry for intersections, both for the wire and for the targets. Special effort was made to replicate similar conditions on all the 10 projects with almost similar geometry of the field coverage by the photos.

The settings of the Nikon D3X camera that was used for these projects are presented at the table 7.1.

Camera settings
28MM AICON Metric Lens
Flash 1/8 with diffusion plate on and flash of large angle
ISO 320
Aperture 11
Exposure time 1/125

Table 7.1 Camera settings
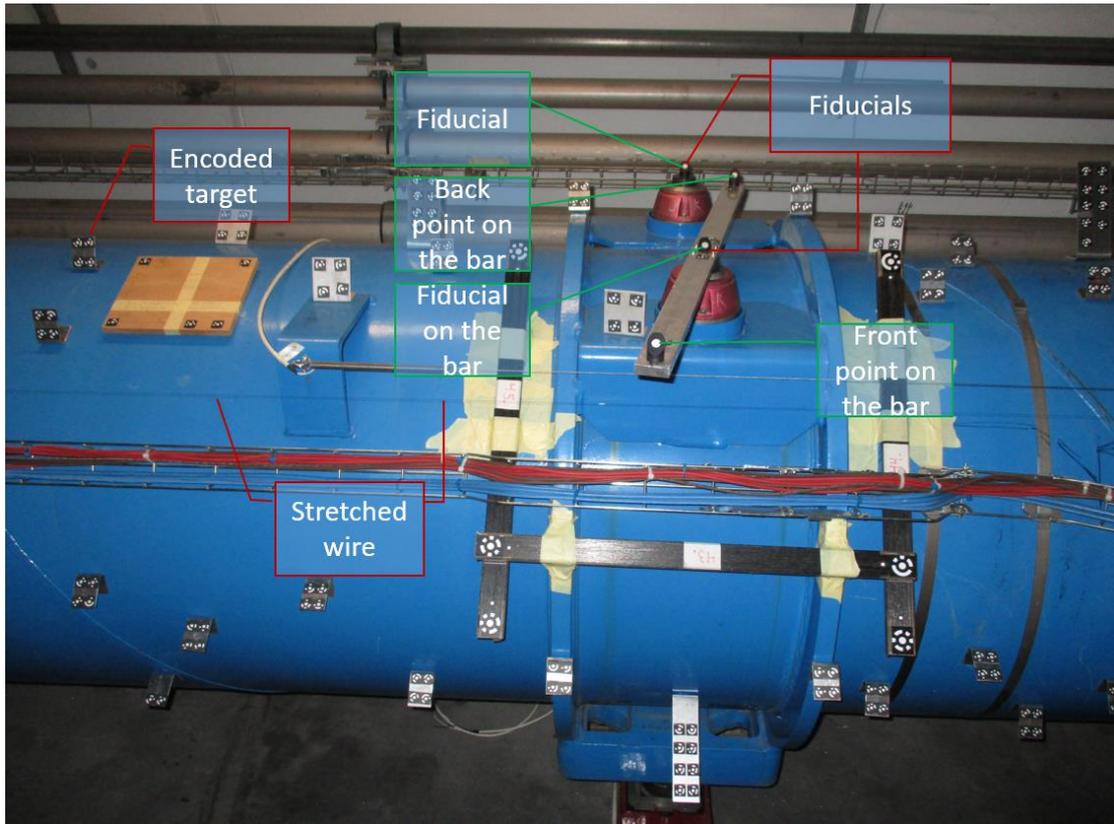
Photo 7.1 Installation of the targets and the stretched wire at the LHC
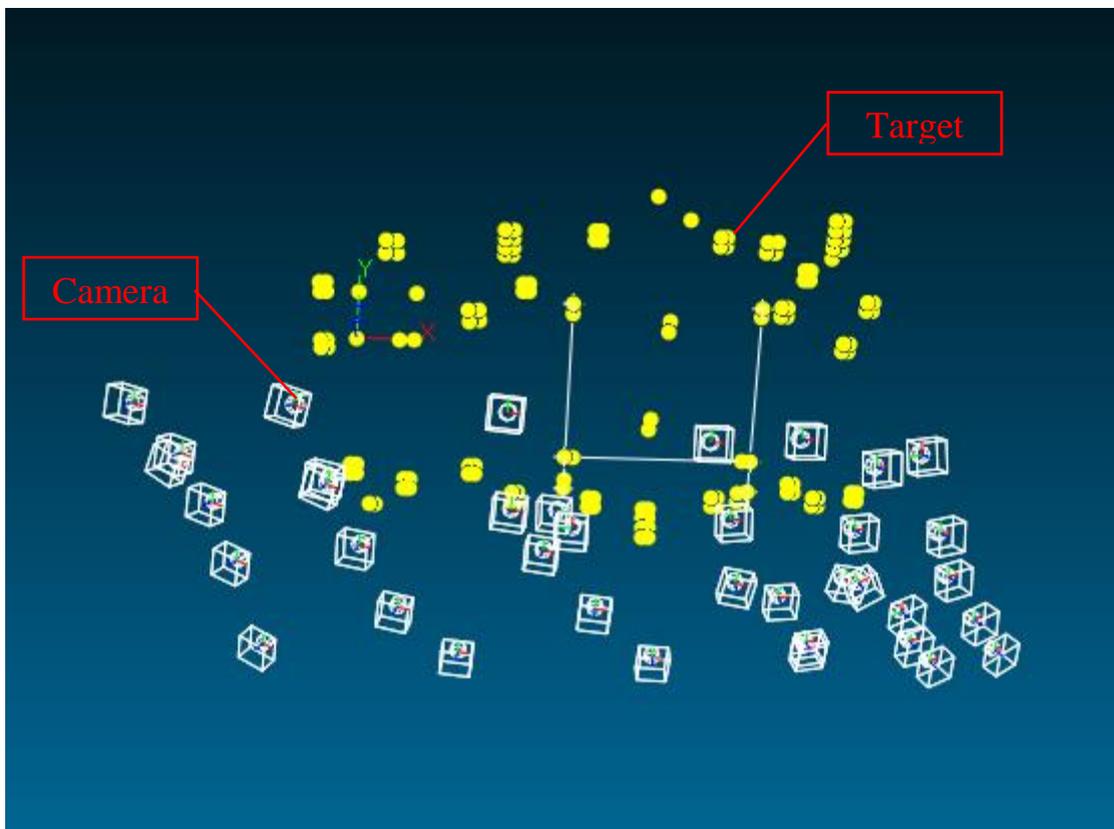
Figure 7.1 Camera positions for a project at the LHC

7.2. Offset measurements

Until now, the radial offset measurements are carried out using ecartometry, which requires a manual procedure and despite the high precision ($\pm$ 15μm to $\pm$ 20μm for single measurement by repeatability) that it provides, it is time consuming. On the other hand, the applied procedure has also several advantages as it is a non-contact measurement technique which is advantageous for automation and the targets as well as the wires can be measured precisely simultaneously.

The key targets for the offset measurements are the fiducials. In order to start the offset measurements, the points on the fiducials should be projected on the wire.

There are two ways that a point can be projected on the wire.

The first one is to do an orthogonal projection of a point to the wire, which basically projects the target perpendicularly to the closest point on the wire, while the second way is to project first the target and the wire on a horizontal plane and then project the point to the wire. If a wire does not have any inclination, the projected points from the aforementioned methods of projection, would be the same. However, this is not the case in the projects that took place at the LHC.

In order to achieve the projection of the fiducials on the wire using the second method, several transformations of the coordinate system should be applied.

The arbitrary 3D coordinate system should be transformed to a system where the front and the back point on the bar, that contains two uncoded targets, will have the same height, thus the same coordinate Z.

The object coordinates of the points that were used for the 3D best fit transformation of all the projects in order to transform their coordinate systems are presented in the table 7.2.

Target	X(mm)	Y(mm)	Z(mm)
Front point	-99.3838	-418.051	12.5587
Fiducial on the Bar	0	0	0
Back point	99.438	418.4869	12.5587
Fiducial of LHC	1.4094	527.8119	2.8586

Table 7.2 Object coordinates of the targets used for the 3D best fit transformation for the verticalization of the coordinate system

It should be mentioned that these coordinates were taken by applying several rotations on an initial project which had an arbitrary coordinate system. Thus, the new coordinates for these points are influenced by the precision that they had as points before the transformation and the error propagation by the transformation. However, due to the fact that a lot of elements such as the precision of the parameters of the interior orientation, the precision of the parameters of exterior orientation, errors during the transformations and others that are not taken into account, an error propagation is too complicated be applied and an estimation of the final precision of the points in the table 7.2 is not possible. Thus, these points might include some errors which will later influence the precision that will be provided on the DY and DZ offset, because all the projects should be transformed with respect to these points which are not defined as errorless. However, the 3D distance, which is independent of any kind of transformation and coordinate system, is able to reveal the precision of the offset measurement, as a 3D distance between the fiducial and its projection on the stretched wire.

Tables 7.3 to 7.7 present the results of the offset measurements of the fiducials with respect to the stretched wire. In the table 7.3, for each project all of the available photos were used during the bundle adjustment.

The tables 7.4 to 7.7, include offset measurements which were calculated using 3, 4, 5 and 6 camera positions. The base of the cameras was approximately 0.75 m to 0.80 m and the distance to the accelerator was approximately 1.0-1.5 m up to. The configurations that were tested are visible in the figure 7.2. The configurations C and D include one and two additional cameras inside the rectangular frame respectively. This is because all the cameras need to be installed on a panel with limited dimensions, hence they can not be put outside of the frame.
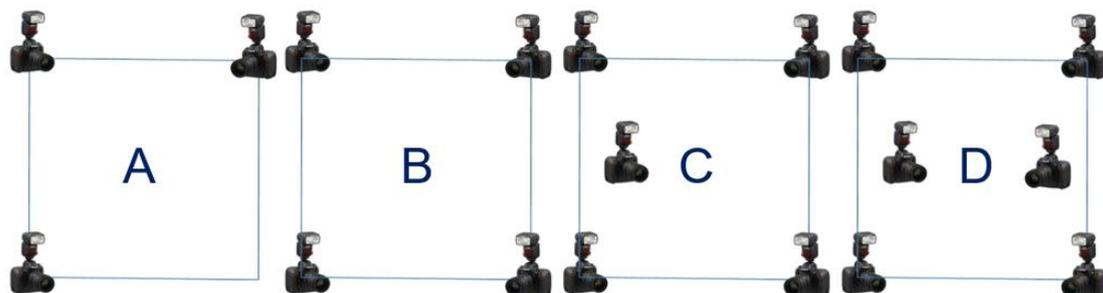
Figure 7.2 Four camera positions configurations for installation on a frame

Project	Fiducial on the bar				Fiducial				Front point on the bar				Back point on the bar			
	DX(mm)	DY(mm)	DZ(mm)	D(mm)	DX(mm)	DY(mm)	DZ(mm)	D(mm)	DX(mm)	DY(mm)	DZ(mm)	D(mm)	DX(mm)	DY(mm)	DZ(mm)	D(mm)
1	0.000	221.838	163.878	275.804	0.000	749.649	166.717	767.964	0.000	-196.213	177.796	264.785	0.000	640.324	175.076	663.828
2	-0.006	221.832	163.887	275.805	-0.021	749.659	166.726	767.975	0.006	-196.217	177.804	264.794	-0.018	640.319	175.086	663.825
3	0.000	221.869	163.875	275.827	0.001	749.676	166.715	767.989	0.000	-196.170	177.796	264.753	0.001	640.350	175.073	663.852
4	0.002	221.841	163.883	275.810	0.006	749.649	166.722	767.965	-0.002	-196.196	177.797	264.773	0.005	640.314	175.086	663.820
5	0.005	221.853	163.883	275.820	0.016	749.669	166.721	767.984	-0.004	-196.192	177.799	264.771	0.014	640.344	175.077	663.847
6	0.005	221.834	163.909	275.819	0.017	749.644	166.749	767.965	-0.005	-196.205	177.824	264.797	0.015	640.318	175.110	663.831
7	-0.008	221.841	163.907	275.824	-0.027	749.661	166.743	767.981	0.007	-196.201	177.818	264.791	-0.023	640.332	175.100	663.841
8	0.006	221.855	163.897	275.829	0.020	749.639	166.740	767.959	-0.005	-196.203	177.826	264.797	0.017	640.322	175.096	663.830
9	0.002	221.878	163.877	275.836	0.006	749.689	166.715	768.002	-0.002	-196.166	177.795	264.749	0.005	640.361	175.070	663.861
10	0.002	221.859	163.919	275.846	0.006	749.657	166.759	767.981	-0.001	-196.194	177.844	264.803	0.005	640.334	175.111	663.846
AVG	0.001	221.850	163.892	275.822	0.002	749.659	166.731	767.977	-0.001	-196.196	177.810	264.781	0.002	640.332	175.089	663.838
STD of the AVG	0.001	0.005	0.005	0.004	0.005	0.005	0.005	0.004	0.001	0.005	0.005	0.006	0.004	0.005	0.005	0.004
STD	0.005	0.015	0.015	0.013	0.016	0.015	0.016	0.013	0.004	0.017	0.017	0.019	0.013	0.015	0.015	0.013

Table 7.3 Offset measurements using all photos

| Project | 3 Photos | | | | | | | | | | | | | | | |
	Fiducial on the bar				Fiducial				Front point on the bar				Back point on the bar			
	DX(mm)	DY(mm)	DZ(mm)	D(mm)	DX(mm)	DY(mm)	DZ(mm)	D(mm)	DX(mm)	DY(mm)	DZ(mm)	D(mm)	DX(mm)	DY(mm)	DZ(mm)	D(mm)
2	-0.001	221.844	163.874	275.807	-0.004	749.644	166.708	767.957	0.001	-196.174	177.784	264.748	-0.004	640.319	175.067	663.820
3	0.004	221.790	163.927	275.794	0.014	749.589	166.766	767.916	-0.004	-196.243	177.853	264.846	0.012	640.292	175.118	663.807
4	-0.005	221.892	163.863	275.839	-0.018	749.686	166.699	767.996	0.005	-196.155	177.782	264.732	-0.016	640.378	175.051	663.873
5	0.005	221.867	163.863	275.819	0.018	749.657	166.709	767.970	-0.005	-196.193	177.797	264.771	0.016	640.332	175.068	663.833
6	0.001	221.845	163.912	275.831	0.002	749.632	166.741	767.953	0.000	-196.213	177.835	264.811	0.002	640.340	175.076	663.843
7	0.008	221.863	163.892	275.833	0.028	749.629	166.729	767.947	-0.007	-196.185	177.815	264.777	0.024	640.366	175.076	663.868
8	-0.013	221.845	163.913	275.830	-0.043	749.660	166.742	767.980	0.011	-196.196	177.823	264.790	-0.037	640.330	175.092	663.837
9	0.007	221.858	163.893	275.830	0.024	749.623	166.735	767.942	-0.006	-196.175	177.825	264.776	0.020	640.313	175.085	663.819
10	-0.008	221.872	163.878	275.832	-0.028	749.675	166.715	767.989	0.007	-196.168	177.797	264.753	-0.024	640.355	175.071	663.855
11	-0.014	221.820	163.961	275.839	-0.048	749.654	166.791	767.985	0.013	-196.214	177.869	264.835	-0.041	640.331	175.146	663.853
AVG	-0.002	221.850	163.897	275.825	-0.006	749.645	166.734	767.963	0.001	-196.192	177.818	264.784	-0.005	640.336	175.085	663.841
STD of the AVG	0.003	0.009	0.010	0.005	0.009	0.009	0.009	0.008	0.002	0.008	0.009	0.012	0.007	0.008	0.009	0.007
STD	0.008	0.029	0.031	0.015	0.028	0.028	0.028	0.025	0.007	0.026	0.029	0.037	0.024	0.026	0.028	0.022

Table 7.4 Offset measurements using configuration A

	4 Photos															
Project	Fiducial on the bar				Fiducial				Front point on the bar				Back point on the bar			
	DX(mm)	DY(mm)	DZ(mm)	D(mm)	DX(mm)	DY(mm)	DZ(mm)	D(mm)	DX(mm)	DY(mm)	DZ(mm)	D(mm)	DX(mm)	DY(mm)	DZ(mm)	D(mm)
2	-0.002	221.851	163.867	275.808	-0.007	749.654	166.709	767.967	0.002	-196.180	177.790	264.756	-0.006	640.320	175.071	663.822
3	0.008	221.794	163.912	275.789	0.028	749.604	166.748	767.927	-0.007	-196.242	177.837	264.834	0.024	640.307	175.092	663.815
4	-0.001	221.893	163.863	275.840	-0.003	749.666	166.702	767.977	0.001	-196.153	177.794	264.739	-0.003	640.374	175.044	663.867
5	0.006	221.860	163.868	275.816	0.021	749.647	166.714	767.961	-0.006	-196.204	177.807	264.786	0.018	640.338	175.069	663.839
6	-0.002	221.824	163.919	275.818	-0.007	749.643	166.749	767.964	0.002	-196.221	177.835	264.817	-0.006	640.326	175.094	663.834
7	0.008	221.861	163.894	275.833	0.028	749.660	166.727	767.976	-0.007	-196.186	177.804	264.769	0.024	640.373	175.080	663.875
8	-0.013	221.845	163.910	275.829	-0.045	749.665	166.740	767.985	0.012	-196.199	177.815	264.787	-0.039	640.323	175.098	663.832
9	0.007	221.857	163.898	275.831	0.024	749.637	166.739	767.956	-0.006	-196.187	177.822	264.783	0.021	640.309	175.092	663.817
10	-0.007	221.872	163.884	275.836	-0.025	749.682	166.718	767.996	0.007	-196.170	177.788	264.747	-0.021	640.351	175.082	663.855
11	-0.004	221.852	163.920	275.840	-0.013	749.679	166.748	767.999	0.003	-196.186	177.821	264.782	-0.011	640.358	175.104	663.867
AVG	0.000	221.851	163.893	275.824	0.000	749.654	166.729	767.971	0.000	-196.193	177.811	264.780	0.000	640.338	175.083	663.842
STD of the AVG	0.002	0.008	0.007	0.005	0.008	0.007	0.006	0.007	0.002	0.008	0.006	0.009	0.007	0.008	0.006	0.007
STD	0.007	0.027	0.022	0.016	0.025	0.023	0.018	0.021	0.007	0.025	0.018	0.029	0.021	0.025	0.018	0.022

Table 7.5 Offset measurements using configuration B

	5 Photos															
Project	Fiducial on the bar				Fiducial				Front point on the bar				Back point on the bar			
	DX(mm)	DY(mm)	DZ(mm)	D(mm)	DX(mm)	DY(mm)	DZ(mm)	D(mm)	DX(mm)	DY(mm)	DZ(mm)	D(mm)	DX(mm)	DY(mm)	DZ(mm)	D(mm)
2	-0.001	221.848	163.868	275.807	-0.004	749.651	166.710	767.964	0.001	-196.182	177.791	264.758	-0.003	640.322	175.072	663.824
3	0.006	221.796	163.914	275.792	0.019	749.601	166.751	767.924	-0.005	-196.242	177.834	264.832	0.016	640.295	175.106	663.807
4	0.000	221.880	163.867	275.832	-0.002	749.666	166.706	767.977	0.000	-196.163	177.794	264.747	-0.001	640.369	175.052	663.864
5	0.003	221.848	163.879	275.814	0.011	749.638	166.722	767.954	-0.003	-196.208	177.810	264.791	0.009	640.335	175.076	663.838
6	-0.001	221.828	163.913	275.817	-0.005	749.648	166.742	767.968	0.001	-196.222	177.819	264.807	-0.004	640.327	175.095	663.835
7	0.009	221.861	163.893	275.831	0.031	749.672	166.728	767.989	-0.008	-196.189	177.804	264.772	0.027	640.367	175.086	663.871
8	-0.013	221.843	163.909	275.827	-0.044	749.671	166.739	767.990	0.012	-196.198	177.819	264.789	-0.038	640.333	175.092	663.840
9	0.008	221.846	163.900	275.824	0.027	749.628	166.743	767.949	-0.007	-196.203	177.822	264.795	0.023	640.306	175.104	663.817
10	-0.007	221.872	163.886	275.836	-0.024	749.681	166.722	767.996	0.006	-196.171	177.788	264.749	-0.021	640.353	175.089	663.859
11	-0.005	221.856	163.906	275.836	-0.017	749.686	166.736	768.004	0.005	-196.176	177.809	264.766	-0.015	640.363	175.094	663.870
AVG	0.000	221.848	163.893	275.822	-0.001	749.654	166.730	767.972	0.000	-196.195	177.809	264.780	-0.001	640.337	175.087	663.842
STD of the AVG	0.002	0.007	0.006	0.005	0.008	0.008	0.005	0.008	0.002	0.008	0.005	0.009	0.006	0.008	0.005	0.007
STD	0.007	0.023	0.018	0.014	0.024	0.026	0.015	0.025	0.006	0.024	0.015	0.027	0.020	0.026	0.016	0.023

Table 7.6 Offset measurements using configuration C

	6 Photos															
Project	Fiducial on the bar				Fiducial				Front point on the bar				Back point on the bar			
	DX(mm)	DY(mm)	DZ(mm)	D(mm)	DX(mm)	DY(mm)	DZ(mm)	D(mm)	DX(mm)	DY(mm)	DZ(mm)	D(mm)	DX(mm)	DY(mm)	DZ(mm)	D(mm)
2	-0.005	221.845	163.869	275.805	-0.016	749.658	166.711	767.971	0.004	-196.194	177.791	264.767	-0.014	640.330	175.074	663.832
3	0.005	221.804	163.911	275.796	0.015	749.616	166.751	767.939	-0.004	-196.247	177.837	264.837	0.013	640.301	175.106	663.812
4	0.002	221.879	163.868	275.832	0.006	749.668	166.706	767.980	-0.002	-196.158	177.794	264.742	0.005	640.372	175.053	663.867
5	0.002	221.848	163.880	275.814	0.008	749.641	166.721	767.957	-0.002	-196.208	177.809	264.789	0.007	640.334	175.076	663.837
6	-0.004	221.838	163.913	275.825	-0.013	749.662	166.745	767.983	0.003	-196.221	177.823	264.809	-0.011	640.330	175.101	663.840
7	0.009	221.863	163.891	275.832	0.031	749.675	166.727	767.991	-0.008	-196.187	177.802	264.769	0.026	640.369	175.084	663.873
8	-0.012	221.843	163.905	275.824	-0.040	749.671	166.739	767.990	0.010	-196.197	177.813	264.784	-0.034	640.331	175.099	663.840
9	0.006	221.838	163.904	275.820	0.020	749.637	166.747	767.959	-0.005	-196.215	177.824	264.805	0.017	640.310	175.110	663.822
10	-0.008	221.870	163.888	275.836	-0.026	749.688	166.722	768.002	0.007	-196.171	177.787	264.748	-0.022	640.359	175.090	663.865
11	-0.002	221.862	163.899	275.837	-0.007	749.693	166.732	768.010	0.002	-196.170	177.801	264.757	-0.006	640.366	175.097	663.873
AVG	-0.001	221.849	163.893	275.822	-0.002	749.661	166.730	767.978	0.001	-196.197	177.808	264.781	-0.002	640.340	175.089	663.846
STD of the AVG	0.002	0.007	0.005	0.004	0.007	0.007	0.005	0.007	0.002	0.009	0.005	0.009	0.006	0.008	0.006	0.007
STD	0.007	0.021	0.016	0.013	0.022	0.024	0.015	0.022	0.006	0.027	0.016	0.030	0.019	0.025	0.018	0.022

*Table 7.7 Offset measurements using configuration D*

133
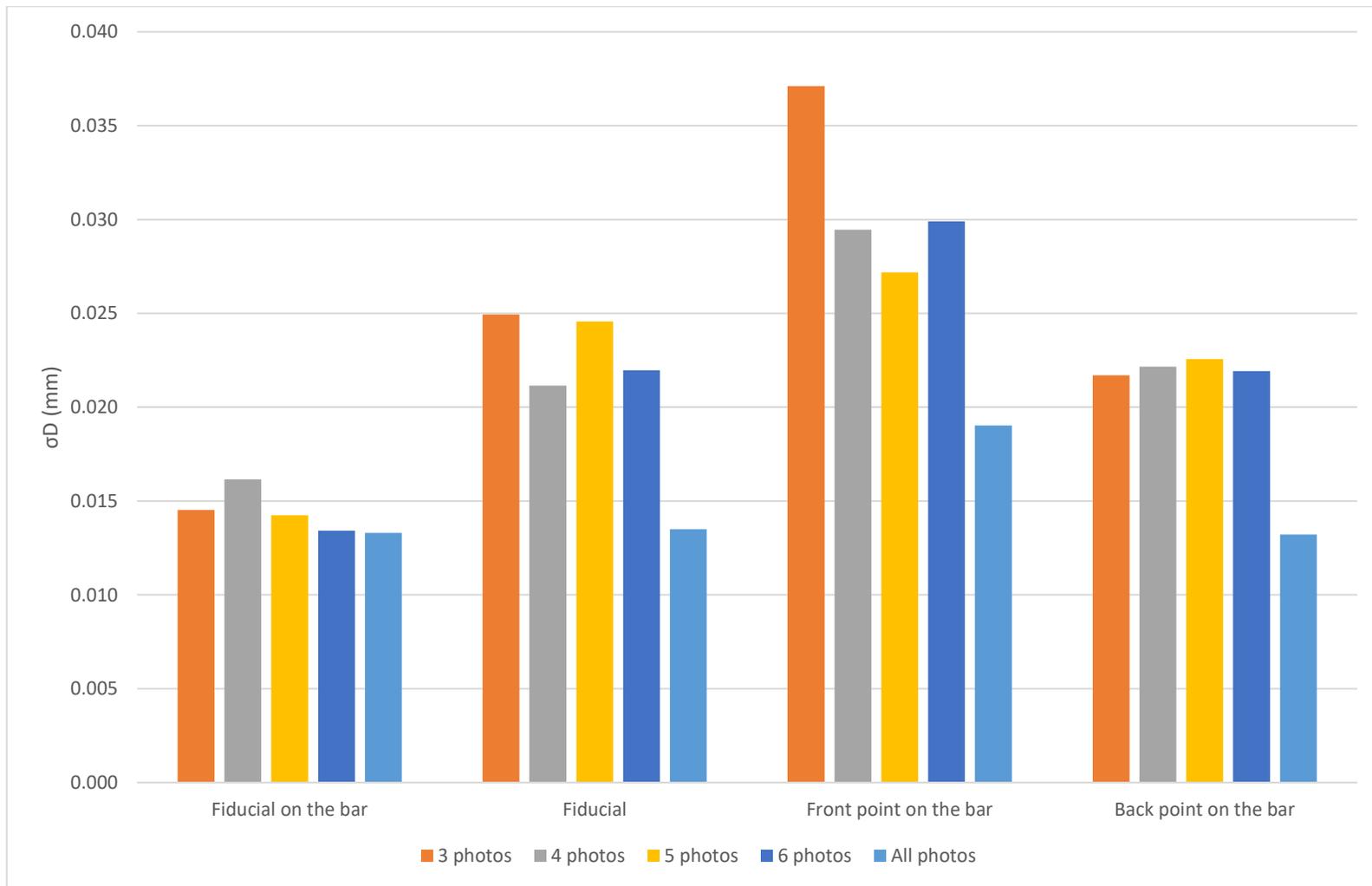
Figure 7.3 Precision of the 3D offset distance with various camera position configurations

Tables 7.3 to 7.7 present that an estimation of the precision of the offset measurement is better to be given by the 3D distance. The radial and vertical offsets (DY and DZ) cannot be estimated as precisely as the 3D distance due to the absence of a lot of information to execute the error propagation while doing a best fit transformation to change the coordinate system. In addition to that, the equipment and the conditions that were available during the tests, make the precise transformation difficult. Thus, the 3D distance which is independent from the transformations is chosen to evaluate the offset measurements. In order to achieve high precision, which will reveal purely the radial and vertical offset measurements precisions, precise bi-directional inclinometers might be required.

Depending on the configuration of the installation of the stretched wire with respect to the fiducials, different inclinometers might need to be installed with different precision.

In particular, if the wire and the fiducials are approximately on the same height, and the focus is set to measure only the radial offset then the 2 inclinometers that will be mounted do not need to be very precise and they can have precision of 5-10 microradian, however if the vertical offset needs to be measured as well, then due to the configuration, it is highly influenced by the inclinations, then very precise inclinometers might be necessary with precision at a level of 1 microradian.

Hence, depending on the configuration that is going to be chosen and which measurements are needed to be done, the inclinometers that will be mounted should have the respective precisions.

It is clear that the bigger the number of photos (cameras) is, the better is the precision achieved, due to the bigger number of observations and the usage of a great variety of positions for the intersections. When all the photos (30-35 photos) on each project are used in order to calculate the offsets, the precision on the fiducials and the points on the bar, are almost the same, between ± 13 μm to ± 19 μm (Fig. 7.3).

Since the number of photos gets limited, when a great number of cameras cannot be installed on a frame, there is a variance among the precisions of the points, which depends on the number of the cameras that were used. The configuration of the cameras and the distance of the frame from the points have an influence on the intersection geometry.

For the fiducial on the bar it is clear from the figure 7.3 that the precision achieved using all photos or a limited number of photos is almost the same. However, for the other points there is a variance. For the second fiducial, which is on the back, the smallest value for σD is achieved using

4 photos which is equal to ±21 μm, however also the 3, 5, and 6 photos provide equivalent results. On the front point on the bar, there is a significant drop from ±37 μm by using 3 cameras, to ±29 μm by using 4 cameras, while the 5 and 6 cameras provide equivalent precision with the 4 cameras. Finally, on the back point on the bar, all the camera configurations provide equivalent results with precisions about ±22 μm. The distances from the camera to the points were between 1 to 2 m, thus the GSD is 200-400 μm/pixel

The above results indicate that the configuration of 4 cameras on the frame provides adequate outcome for the demands that are required. The results are in general better than the results that come from the 3 camera configuration, and equivalent to the ones of 5 and 6 cameras configuration.

The geometric configuration of 4 cameras provides enough rays for the intersections of the targets and good configuration for the wire measurement. The precisions on the offsets for the fiducials are about ±15 μm to ±20 μm which verifies that offset determination with photogrammetry can be performed precisely and is able to provide reliable results, directly comparable with the measurements that can be carried out through ecartometry.

The precision achieved using photogrammetry can be directly compared to the average precision that can be achieved by the repeatability of the offset measurement by ecartometry. From tests performed, the average precision results from repeatability by ecartometry is around ±16 μm for the radial offset (Valentin P. 2018).

This precision is at the same level as the precision achieved by the photogrammetric determination of the 3D distance. In the future if precise bi-directional inclinometers will be installed on the mounted frame on the train, then the radial and the vertical offsets can be measured with higher precision, than they are determined right now, due to the elimination of errors introduced from the connection to gravity.

The results using photogrammetry are very promising and the offset measurements through that are likely to substitute the radial offset measurements carried out by ecartometry due to their precision.

It should be mentioned that, the frame with mounted inclinometers and the cameras will be able to provide results which will be free of human errors. This on the other hand, is not possible through ecartometry which is a manual procedure, highly dependent on the user.

Reproducibility tests by ecartometry have shown that the precision achieved is at the level of ±110 μm, due to the fact that when the user tries to install again the configurations for the measurement, it is more prone an error. This will directly affect arbitrarily the result of the measurement and its precision (Valentin P. 2018). This is not the case in photogrammetry. Such errors might occur due to the user's lack of experience or due to some mechanical problems of the instrument that is used.

Chapter 8

CONLUSIONS

8.1. Conclusions

The aim of this thesis was the development of an algorithm for the encoded and uncoded targets position determination in 2D and 3D. The final goal is the calculation of the offset distances of the fiducials with respect to a stretched wire.

This work was separated into several parts to finally achieve the offset calculation. The very first one, is the target detection. All the targets should be automatically detected in order to proceed to the target position determination in 2D. Then, a number should be assigned to the targets in order to find their homologous points. If the targets are encoded their code will be extracted from the decoding algorithm that runs on their code segments. If they are uncoded targets, the correspondence will be achieved by 3D intersections. In this way, all the information about the targets will be gathered. After that, the stretched wire should also be determined. By using the developed algorithm, a list of 2D image coordinates is extracted which for each photo includes two points on the wire which are on the edges of each image. Since, the data for the targets and the wire are acquired, further processing on them can be carried out in order to transform them to a format that can be used as input for the CERN's adjustment program LGC2. Once the fiducials are projected on the wire, they can also be input using specific format on the LGC2 file, in order to run the adjustment. After the adjustment, the final 3D coordinates for both the fiducials and their projections are acquired and the offset measurement can be accomplished.

As it is mentioned, the detection of the targets is very crucial. It is the initial step of the developed algorithm. It is important that all targets should be detected correctly. It is crucial to have a great number of targets in order to increase the number of observations to determine the orientations more precisely and reliably.

If some points are missing, the determination of the orientations will be poorer and more importantly if some targets as the fiducials miss from the list of detected points then, the calculation of offsets will not be possible.

For the detection, depending on the minimum size of the target the sensibility parameter changes. The larger the targets, the less noise will

be included as possible targets, due to the decrease of the sensibility. In general, larger targets can be detected much more easily than the smaller targets. The size limit for the target detection is about 4-5 pixels in diameter. Below this value, the algorithm is unable to reliably detect targets. On all the projects the number of targets that has been identified by AICON software and the developed algorithm is on the same level, a fact that confirms its reliability.

After the automatic detection, a number of tests were performed in order to find the best way to carry out the target measurement. The most precise and simultaneously reliable is the ellipse fitting. So, a sub-pixel edge detector runs on each target image in order to find edges. Once these edges are found, then an ellipse adjustment is performed by using least squares. In this way, the best possible ellipse will be fitted to the edges that were found and also an indication of precision will be available due to the variance-covariance matrix that comes out of the adjustment.

If a target is damaged or for an unknown reason several edge points are not correct, they will be excluded from the list of edge points because their residuals may exceed the $3\sigma_0$. Hence, it is avoided that some wrong observations will be included for the estimation of the center of the ellipse. If the precision of a target that is calculated from least squares is bigger than $\pm0.5\mu m$ then this point is considered as a blunder and is not included for further processing. The typical precision of the 2D measurement of the targets using the ellipse fitting is about ±0.04 pixel on both x and y which is equivalent to the one that AICON software provides.

The decoding of the encoded targets is an important tool in order to find the correspondence of them among several images. Depending on whether a target is 12, 14 or 20 bits, the amount of points that are going to be spread on the code segments will be respectively 12, 14 or 20.

Afterwards, a binary number is going to be generated which indicates a specific code. The code that is going to be chosen as the representative for this specific spread will be the minimum number in the decimal system which is generated from repeated transfers of the first digit of the binary code sequence to the end of the binary code.

When the minimum number from the decimal system is chosen, there should be a search for its correspondence to the AICON code in a look-up table. The dissemination of the points on the code segments is going to be carried out 4 more times, by using each time a different rotation of the ellipse and each time a code will be generated. If the same code is generated at least two times, then this code is selected as the code that the

target is going to have. The decoding algorithm is able to provide very reliable results and on a total project almost all the coded targets have been assigned the same code both by AICON and the developed decoding algorithm. On all the test projects, more than 95% of the encoded targets detected both by AICON and the algorithm, had the same code assigned.

Finally, the data gathered from the encoded targets, the uncoded targets and the points of the wire should be treated to be compatible with the observations that the LGC2 requires. Most of the LGC2 files that were used during the elaboration of the thesis used as type of observations the UVEC (unity vectors). The fiducials also should be projected on the wire after the coordinate system is transformed in order to have the Z axis parallel to the vertical. Once this is done, the projected points should be included to the LGC2 file and the adjustment should be performed. The output of the adjustment provides the 3D coordinates for the fiducials and their projections. Thus, the 3D distance between them could be calculated.

Depending on the number of cameras that are used, the precision that is achieved varies. However, a frame with 4 cameras on its edges, creates a good geometric configuration for the target position determination both in 2D and 3D and the wire measurement which provides satisfying results and precisions. The precision on the offsets for the fiducials is from ± 15 μm to ± 20 μm which indicates that offset determination with this procedure is precise enough and is able to provide reliable results.

The developed algorithm is able to provide reliable results both in 2D and 3D. The 3D offset distance can be determined precisely with a standard deviation which fluctuates about ± 15 μm to ± 20 μm, depending on the position of the fiducial.

For the precise calculation of the 3D distance to the radial and vertical offset, two precise bi-directional inclinometers should be installed on future frames, which will provide the inclinations to transform with precision the coordinate system with respect to the vertical, thus to connect the frame to the gravity. Hence, the offset measurement precision will not be influenced by external factor but mainly from the measurement precision of the points and the wire.

The precision of ± 15 μm to ± 20 μm which is achieved by this procedure is very promising and is equivalent to the precision that is achieved by ecartometry. In addition the proposed procedure has the advantages of the automation of the measurement and the elimination of the human interference. So, some errors depending on the user are eliminated.

141
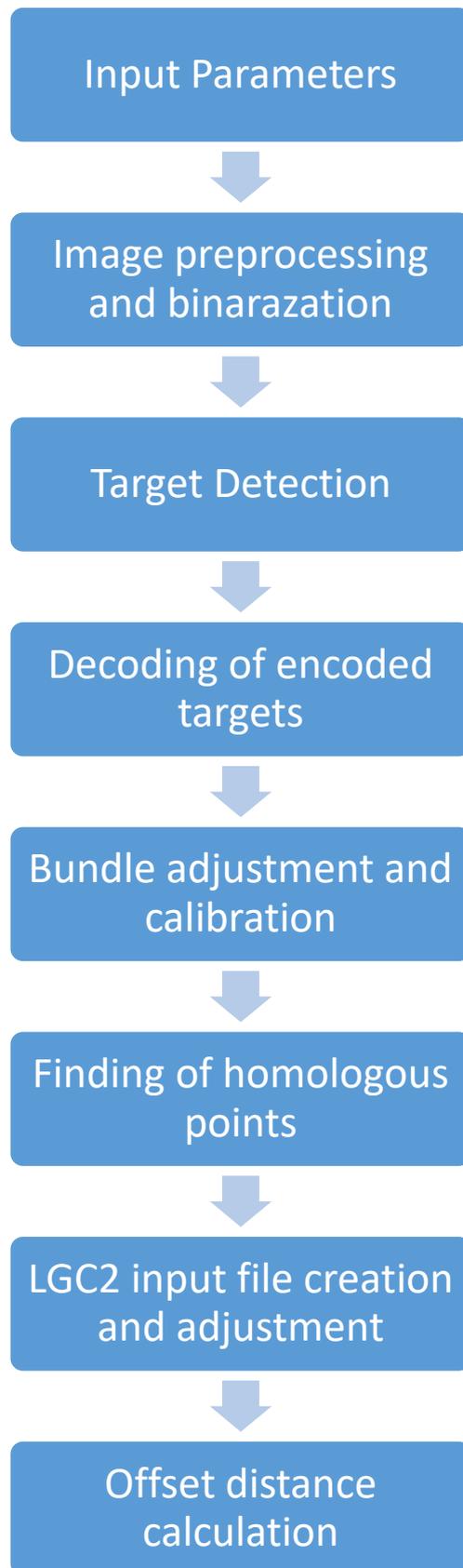
Figure 8.1 Algorithm procedure diagram

Bibliography

1. Adamopoulos L., Viskadourakis V., Gavalas D., Polizos G., Sverkos A., *Mathematics for Science and Technology Direction,* Athens, Greece: Diofantos Computer Technology and Publications Institute, 2018.

2. Agatza-Balodimou A.M., *Least squares adjustment I,* Athens, Greece: NTUA, 2009.

3. Barbier M., Dorleat Q., Jones M., LGC *a new revised version,* Geneva, Switzerland, 2016.

4. Behrens A., Bestmann P., Charrondiere C., Feniet T., Grenard JL., Mergelkuhl D., *The LHC Collimator Survey Train*, *11th International Workshop on Accelerator Alignment (IWAA2010),* Hamburg, Germany, 2010.

5. Behrens A., Mergelkuhl D., Vendeuvre C., *Evaluation of stretched wire measurement based on photogrammetry in the contect of CERN*, *14th International Conference on Accelerator Alignment,* Grenoble, France, 2016.

6. Chandrakala M., Durga Devi P., *Qualitative Comparison of Threshold based, International Journal of Advanced Research in Electronics and Communication Engineering (IJARECE),* Bhopal, India, 2016.

7. Dawkins P., *Calculus III Online Notes.*

8. Fatoumata D., *Object Detection using Circular Hough Transform,* Quebec City, Canada, 2015.

9. Fisher R., Perkins S., Walker A.,Wolfart E,. *Gaussian Smoothing,* Edinburgh, Scotland, 2003.

10. Greensted A., *Otsu Thresholding.*

11. Houcque D., *Introduction to MATLAB for engineering students.* Evanston, USA: Northwestern University, 2005.

12. Ioannidis H., *Photogrammetry Courses Notes NTUA.*

13. Komal Vij, Yaduvir Singh., *Enhancement of Images Using Histogram Processing*, *International Journal of Computer Applications in Technology,* Patiala, India, 2011.

14. LaValle S., *Planning Algorithms.*, Cambridge, United Kingdom: Cambridge University Press, 2006

15. Luhmann T., Robson S, Kyle S, Harley I. *Close Range Photogrammetry.* Dunbeath, Scotland, UK: Whittles Publishing, 2006.

16. Manolopoulos K., *Development of code for automatic recognition of targets and use in the VISUALSFM software., Diploma thesis,* Athens, Greece: NTUA, 2017.

17. Mergelkuhl D., *Measurement of stretched wires using photogrammetry 2011+2015.* Geneva, Switzerland, 2015.

18. Pedersen S., *Circular Hough Transform*, 2007.

19. Quesnel J., Durand H., Touzé T., *Stretched Wire Offset Measurements : 40 years of practice of this technique at CERN, 10th International Conference on Accelerator Alignment,* Tsukuba, Japan 2008.

20. Rossi L., The LHC superdonducting Magnets, *Particle Accelerator Conference 12-16 May 2003,* Portland, USA, 2003.

21. Scandella L. *Développement d'un algorithme de détection et de mesure d'un fil tendu sur des photos de l'accélérateur LHC au CERN.* Strasbourg, France: INSA, 2017.

22. Schenk T., *Introduction to Photogrammetry,* Columbus, USA: Department of Civil and Environmental Engineering and Geodetic Science, 2005.

23. Touzé T., *Effects of the Earth inertial forces on the Wire Positioning System,* Geneva, Switzerland: CERN, 2007.

24. Trujillo-Pino A., Krissian K., Aleman-Flores M., Santana-Cedres D., *Accurate Subpixel Edge Location based on Partial Area.,* In *Image and Vision Computing*, 72-90, Amsterdam, Netherlands: Elsevier, 2013.

25. Valentin P., "Private communication." 2018.

26. Vendeuvre C., *Évaluation des mesures de fils tendus par photogrammétrie en vue de l'automatisation des mesures d'écartométrie pour l'accélérateur de particules LHC au CERN,* Strasbourg, France: INSA, 2016.

27. Zhan Y., *Least Squares Fitting of Ellipses,* Princeton, USA: Princeton University, 2014.

28. Zhu Y., Huang C., *An Adaptive Histogram Equalization Algorithm on the Image., 2012 International Conference on Solid State Devices and Materials Science,* Kyoto, Japan, 2012.

Websites

1.   Böhm J. Last access August 15, 2018.
      http://www.janboehm.de/Projects/Target/target.html.

2.   *CERN About.* Last access April 23, 2018.
       https://home.cern/about.

3.   *CERN Accelerators.* Last access April 23, 2018.
      https://home.cern/about/accelerators.

4.   *CERN Accelerators.* Last access April 23, 2018.
      https://home.cern/about/how-accelerator-works.

5.   *CERN EN-SMM Group.* Last access April 26, 2018.
      http://en.web.cern.ch/en-smm-group.

6.   *CERN History.* Last access August 16, 2018.
      https://timeline.web.cern.ch/timelines/The-history-of-CERN.

7.   *CERN Large Hadron Collider.* Last access April 26, 2018.
      https://home.cern/topics/large-hadron-collider.

8.   *CERN LGC.* Last access June 14, 2018.
      https://readthedocs.web.cern.ch/display/SUS/LGC+v1.

9.   *CERN LHC.* Last access April 23, 2018.
      https://lhc-machine-outreach.web.cern.ch/lhc-machine-
      outreach/lhc-components.htm.

10.   *Geodetic Systems.* Last access May 02, 2018.
      https://www.geodetic.com/basics-of-photogrammetry-
      v2/#_Toc496190829

11.   *LGC2 User Guide.* 2018 Last access September 05, 2018.
      https://readthedocs.web.cern.ch/display/SUS/LGC2+User+Guide.

12.   *LHC Machine Outreach Components.* Last access April 26, 2018.
      https://lhc-machine-outreach.web.cern.ch/lhc-machine-
      outreach/lhc-components.htm.

13.   *Mathworks Coordinate Systems.* Last access May 05, 2018.
      https://ch.mathworks.com/help/vision/gs/coordinate-systems.html.

14.   *Mathworks Feature Matching.* Last access May 02, 2018.
      https://ch.mathworks.com/help/vision/examples/object-detection-
      in-a-cluttered-scene-using-point-feature-matching.html.

15. *Mathworks Sharpening.* Last access August 02, 2018. https://ch.mathworks.com/help/images/ref/imsharpen.html.

16. *Regionprops Matlab.* Last access August 27, 2018. https://ch.mathworks.com/help/images/ref/regionprops.html.

17. *Rotation Matrix Wolfram.* Last access August 15, 2018. http://mathworld.wolfram.com/RotationMatrix.html.

18. Salmon J. *XYHT.* Last access April 26, 2018. https://www.xyht.com/lidarimaging/state-of-close-range-photogrammetry/.

19. *Spherical Coordinates Wolfram.* Last access August 15, 2018. http://mathworld.wolfram.com/SphericalCoordinates.html.

20. *Stackexchange Mathematics.* Last access August 20, 2018. https://math.stackexchange.com/questions/2645689/what-is-the-parametric-equation-of-a-rotated-ellipse-given-the-angle-of-rotatio.